

Doctoral Dissertation

Design and fabrication of a multi-spectral near-infrared fundus camera
with a patterned interference filter for light scattering detection

Ze Wang

March 2022

Division of Material Science

Graduate School of Science and Technology

Nara Institute of Science and Technology

Abstract

Over the one century, with the development of optics and electronics, a variety of fundus cameras have been developed. Recent fundus camera development trends are miniaturization and cost reduction while improving image quality. However, high-resolution fundus images alone are not sufficient for health checks and disease prevention, and more detailed fundus information needs to be gathered from fundus images.

This research proposed a multi-spectral near-infrared fundus camera with a patterned interference filter for light scattering detection. Besides the fundus image, the proposed fundus camera can obtain the scattering information from the fundus compared with the previous fundus camera. This scattering information reflected the components inside the fundus tissues and vasculature, which can be used for lifestyle diseases diagnosis and disease prevention. To verify this proposal, the fabrication of this fundus camera and scattering experiments were introduced.

The fundus camera for light scattering detection was a combination of a projection mask and a fundus camera. For easier eyeball fixation and pattern projection on the fundus, the layout of the projection mask with three areas was designed, an eyeball fixation target, lines for linear patterned illumination, and fundus illumination area. In the scattering detection with the patterned metal mask fabricated following the layout, the human blood was replaced by artificial blood to simulate the reduced scattering coefficient of lipid. The positive relationship between the scattering information and the reduced scattering coefficient proved the feasibility of the lipid concentration measurement by scattering detection.

The layout of the projection mask was optimized to avoid the potential interaction of the adjacent pattern and easier eyeball fixation. The patterned metal mask in the scattering detection

was replaced by a patterned interference filter fabricated following the optimized layout. The results theoretically revealed that blood lipid concentration could be measured using the fundus camera with a patterned interference filter.

Acknowledgments

First of all, I would like to express my heartfelt gratitude and sincere esteem to Professor Jun Ohta for providing me a precious chance to start my Ph.D. course at the Photonic Device Science laboratory at Nara Institute of Science and Technology (NAIST). During our first meeting at an interview online, his enthusiasm and personality meant his laboratory is an excellent place for research, and it proved to be so. Prof. Jun Ohta guided me in the way to fulfill my research and provided me so many opportunities to practice my logical thinking and expression skills, I have benefited a lot from his advice during my Ph.D. course.

I would like to thank my supervisors, Professor Yukiharu Uraoka and Associate Professor Yaxiaer Yalikun, for always providing me comfortable discussion atmosphere and precious comments on my research over three years.

I would like to thank my supervisor, Associate Professor Kiyotaka Sasagawa, for his always patience guiding, and fruitful advice during the discussion in overcoming the barriers in my Ph.D. course. I would like to thank Associate Professor Hiroyuki Tashiro and Assistant Professor Makito Haruta for their helpful guidance and wisdom during my Ph.D. course.

I would like to thank Assistant Professor Hironari Takehara for his guidance, help, and encouragement. His guidance has been with me throughout my Ph.D. course. He was always willing to discuss and guide me through any research challenges I encountered, even during holidays or the New Coronavirus pandemic. Besides the guidance and helps in research, I benefited greatly from his personality, wisdom, and encouragement. Do not give up is what I learned from him, and keep going was what he said after every discussion we had. These have lifted me up during my Ph.D. course. I couldn't imagine what my study would be like without his guidance.

I would like to thank Mrs. Ryoko Fukuzawa, the secretary of our laboratory, who helped me a lot with the daily document work and allowed me to pay more attention to my research. I would like to thank Dr. Yasumi Ohta, the postdoctoral fellow in our laboratory, who always encouraged me in research and shared delicious desserts with us.

My sincere thanks also go to Professor Koichi Shimizu of Waseda University for giving me the opportunity to do a lab stay at his laboratory and for supporting my research.

I would like to thank Mr. Motoshi Sobue, CEO of Nanolux Co. Ltd., and Mr. Akihiko Futada, the collaborative researcher in our laboratory, for their technical support in the NIR colorization technology.

This research was supported by JST ACCEL(JPMJAC1601). This research was also supported by VLSI Design and Education Center (VDEC), the University of Tokyo, in collaboration with Cadence Design System, Inc. and Mentor Graphics, Inc.

I would also like to extend my acknowledgment to all members of Photonic Device Science Laboratory in NAIST for the daily discussions and cooperation. I enjoyed both the research and life in this big family and the memories here will always be in my heart. I wish you all have a bright future. I also want to thank all the friends who shared me with support and advice during my Ph.D. course, no matter in research or life. These help to me are like a fire in the winter, giving me the strength to move forward.

Last but not least, I would like to say a big thank you to my parents. Thank you so much for your concern and understanding. The presence of the new coronavirus makes it especially difficult to get together from thousands of miles away, but I can never forget how much I miss you! Words cannot express my feelings right now, but I still want to express them with a thank you!

Contents

Abstract	iii
Acknowledgments	v
List of Figures.....	x
List of Tables	xvi
1. Introduction	1
1.1 Development of Fundus Camera.....	1
1.2 Scattering in Fundus Tissues for Disease Diagnosis.....	1
1.3 The Principle of Interference Filter	4
1.4 The Purpose of This Research	7
1.5 Thesis Outline	8
2. The Multi-spectral NIR Fundus Camera for Fundus Observation	10
2.1 Prototype NIR Colorized Fundus Camera.....	10
2.2 Optical Simulation of the Fundus Camera	11
2.2.1 Components Selection by Optical Simulation	11
2.2.2 Evaluation of Simulation Results	13
2.3 Configuration of the Fundus Camera	14
2.4 Fundus Imaging by the Fundus Camera	16
2.5 Summary and Discussion	18

3.	Pattern Projection on the Fundus.....	20
3.1	Overview	20
3.2	Optical Design Modification for Fundus Pattern Projection	22
3.2.1	Components Selection	22
3.2.2	Evaluation of Simulation Results	26
3.3	Design of the Projection Mask.....	27
3.3.1	Fundus Based Layout Design.....	27
3.3.2	Parameters Selection.....	28
3.3.3	A Fabricated Patterned Metal Mask	29
3.4	Configuration of the Fundus Camera for Pattern Projection	30
3.5	Pattern Projection on the Retina with a Patterned Metal Mask	33
3.6	Scattering Experiments with a Patterned Metal Mask	34
3.6.1	Preparation of the Artificial Blood	35
3.6.2	Scattering Experiment System	40
3.6.3	Scattering Results Analysis.....	44
3.7	Summary and Discussion	47
4.	A Multi-Functional Interference Filter for Patterned Fundus Illumination	49
4.1	Overview	49
4.2	Design of a Multi-Functional Interference Filter.....	51
4.2.1	Layout Optimization of Each Functionality in the Projection Mask.....	51

4.2.2	Transmittance Simulation of Multi-Functional Interference Filter	55
4.3	Fabrication of the Multi-Functional Interference Filter	60
4.3.1	The Fabrication Flow Chart of the Multi-Functional Interference Filter	60
4.3.2	The Process Conditions during the Fabrication	64
4.4	Evaluation of the Multi-Functional Interference Filter	72
4.5	Summary and Discussion	74
5.	Scattering Detection by Pattern Projection	76
5.1	Overview	76
5.2	Pattern Projection on the Retina with a Multi-Functional Interference Filter	76
5.3	Scattering Experiments with a Multi-Functional Interference Filter	82
5.4	Summary and Discussion	85
6.	Conclusion	86
6.1	Summary.....	86
6.2	Future Plan.....	88
	References	90
	Appendix.....	97
	List of publications	102

List of Figures

Fig. 1.1 Photograph of the retina of the human eye, with overlay diagrams showing the positions and sizes of the macula, fovea, and optic disc [20]......2

Fig. 1.2 Photograph of the device for lipid concentration detection by detecting the blood scattering properties [28]......3

Fig. 1.3 (a) Schematic diagram of the near-infrared hyperspectral imaging system. (b) Visualization of the lipid content in mouse liver. The quantitative mapping of the lipid content in the liver samples is shown in the left, the visible images of the liver samples are shown in the right [37]......4

Fig. 1.4 Transmission spectrum of blue absorption filter and yellow-green absorption filter [39]......5

Fig. 1.5 Schematic diagram of the reflection and transmission in the interference filter. ..6

Fig. 1.6 Photograph of the commercial portable fundus camera with visible light illumination [43].7

Fig. 2.1 Schematic diagram of the prototype NIR color fundus camera developed by our lab.....10

Fig. 2.2 The color fundus image taken by the prototype NIR color fundus camera without visible illumination light. 11

Fig. 2.3 Schematic diagram of the fundus camera system in the numerical optical simulation. 12

Fig. 2.4 The incoherent irradiance distribution of (a) the illumination light on the detector and (b) cross-section row on the detector in numerical optical simulation. 13

Fig. 2.5 Photograph of the four bands LED in the fundus camera for illumination.	15
Fig. 2.6 Photograph of the assembled fundus camera following the optical simulation. .	16
Fig. 2.7 Clear fundus image of the eye model taken by the assembled fundus camera after calibration.	17
Fig. 2.8 Photograph of the eye model in this research from the front and back sides.	17
Fig. 2.9 Fundus image of a human eyeball taken by the assembled fundus camera.	18
Fig. 3.1 Outline diagram of the contents in Chapter three.	21
Fig. 3.2 The pattern of the projection mask projected on the detector in the fundus camera numerical optical simulation.....	23
Fig. 3.3 Schematic diagram of the fundus camera with a projection mask in numerical optical simulation.....	24
Fig. 3.4 Linear stripe pattern on the detector in the numerical optical simulation. The widths of the lines of the projection and the spaces between them are 1.25 mm.	24
Fig. 3.5 Linear stripe pattern with distortion on the detector in the simulation by the fundus camera without meniscus lens.	25
Fig. 3.6 The cross-section column incoherent irradiance distribution of the linear stripe patterned illumination beam on the detector in numerical optical simulation.	26
Fig. 3.7 (a) Photograph of the human eyeball retina captured by a conventional fundus camera and (b) schematic of the fundus patterned illumination.	28
Fig. 3.8 The layouts of the designed patterned mask with three parts.....	29
Fig. 3.9 Photograph of the fabricated patterned metal mask.....	30

Fig. 3.10 Measured spectrum of the 800 nm LED.	31
Fig. 3.11 The absorption spectrum of the oxygenated and deoxygenated hemoglobin from 300 nm to 1000 nm [51], [52].....	32
Fig. 3.12 Photograph of the fundus camera with a patterned metal mask for pattern projection.	32
Fig. 3.13 Photographs of the linear stripe pattern projected on fundus in (a) the glass eye model and (b) human eyeball.	34
Fig. 3.14 Schematic diagram of the measurement system of optical parameters.....	38
Fig. 3.15 The fitting curve of the relationship between ink concentration and absorption coefficient.	39
Fig. 3.16 The fitting curve of the relationship between the Intralipos concentration and reduced scattering coefficient.	39
Fig. 3.17 Schematic diagram of the scattering detection system. Part A is the fundus camera with a patterned metal mask, part B is the eye model with artificial blood, and part C is the monitor.	41
Fig. 3.18 Photograph of the assembled fundus camera with a patterned metal mask and an eye model for scattering detection.	41
Fig. 3.19 Photograph of the glass tube (capillary) in the scattering experiment.	42
Fig. 3.20 Photograph of the linear stripe patterned light on a glass tube filled by artificial blood for scattering measurement.	43
Fig. 3.21 Schematic diagram of scattering measurement by a glass tube with artificial blood.....	43

Fig. 3.22 The propagation diagram of scattered photons in well blended artificial blood.	45
Fig. 3.23 Schematic diagram of the single Mie scattering.	46
Fig. 3.24 Normalized pixel values for different scattering lengths of the artificial blood with different reduced scattering coefficients.	47
Fig. 4.1 Outline diagram of the contents in Chapter four.	50
Fig. 4.2 Normalized pixel value dependence on the distance from start point measured for the sample with 7.68 mm^{-1} reduced scattering coefficient.	52
Fig. 4.3 The layouts of (a) the multi-linear stripe pattern with a 3.1 mm line pitch and (b) the single linear stripe pattern.	53
Fig. 4.4 Layout of the new eyeball fixation target.	54
Fig. 4.5 Layout of the new eyeball fixation target and multi-linear stripe pattern.	55
Fig. 4.6 Schematic structure of the multi-functional interference filter for pattern projection on the fundus.	57
Fig. 4.7 Simulated transmission spectrum of the multi-functional interference filter with 18-layer film stack. The blue curve shows the transmission spectrum of the linear stripe pattern, with a narrow transmittance peak at 800 nm; the green curve shows the transmission spectrum of the eyeball fixation target, with a narrow transmittance peak around 680 nm; the red curve shows the transmission spectrum of the fundus illumination area. All these spectrum curves have high transmittance at the NIR band.	58
Fig. 4.8 The fitting curve of the relationship between the deposition time and deposition	

thickness.	65
Fig. 4.9 Schematic structure of the bottom 9-layer film stack of the multi-functional interference filter. The first layer from the bottom of this 9-layer film stack is marked with B1.	65
Fig. 4.10 The fitting curve of the relationship between the etching time and thickness of the intermediate layer (TiO ₂).	68
Fig. 4.11 Microphotographs of the eyeball fixation target in the bottom 9-layer film stack after the first cycle of the photolithography and etching.	69
Fig. 4.12 Microphotographs of the partial areas in the fabricated 9-layer film stack.	70
Fig. 4.13 The transmission spectrum of the fabricated multi-functional interference filter measured by the MSRFTM system.	72
Fig. 4.14 Photograph of the fabricated multi-functional interference filter.	73
Fig. 5.1 Schematic diagram of the NIR fundus camera with a patterned interference filter for pattern projection on the fundus.	77
Fig. 5.2 Photograph of the NIR fundus camera with a patterned interference filter for projection on the fundus.	78
Fig. 5.3 Fundus image of the eye model with a linear stripe illuminate by 800 nm light.	79
Fig. 5.4 The observed image through the ophthalmic lens in the NIR fundus camera with a patterned interference filter with 800 nm wavelength light illumination.	80
Fig. 5.5 The observed image through the ophthalmic lens in the NIR fundus camera with a patterned interference filter with 660 nm wavelength light illumination.	79

Fig. 5.6 Fundus images of the human eyeball taken by the NIR fundus image with the patterned interference filter by the linear stripe patterned illumination light with (a) 660 nm and 800 nm, (b) 660 nm, 800 nm, and NIR band.....	81
Fig. 5.7 Schematic diagram of the scattering detection system.	82
Fig. 5.8 Normalized pixel values for different scattering lengths of the artificial blood with different reduced scattering coefficients.	83
Fig. 5.9 Photograph of the linear stripe patterned light on a glass tube filled by artificial blood.....	83
Fig. 5.10 Normalized pixel values for different reduced scattering coefficient when scattering distance equal to 0.345 mm.	84

List of Tables

Table 2.1 The part number of optical components in the fundus camera.	15
Table 3.1 The components concentration and reduced scattering coefficient of the artificial blood.....	40
Table 4.1 The film thickness of the multi-functional interference filter in the simulation.	59
Table 4.2 The flow chart of the fabrication of the 18-layer multi-functional interference filter.	60
Table 4.3 The constant parameters during the sputtering deposition.	66
Table 4.4 Deposition time for different target materials.	66
Table 4.5 The constant parameters during the etching process.	67
Table 4.6 The etching times for different areas in the bottom 9-layer film stack.....	68

1. Introduction

1.1 Development of Fundus Camera

The first fundus camera was developed in the 1900s [1], [2]. The principle of the fundus camera requires that the illumination and imaging pathways pass through different portions of the eye's optics to avoid back reflection [3]. The complex optical system of the fundus camera enables the observations of the interior of an eye. It can be used to diagnose several eye diseases by allowing fundus observations. With the development of the fundus camera, the field of view enlarged [4], [5], the traditional camera was replaced by a digital camera [6], aberrations decreased [7], and image resolution increased [8][9]. Since the fundus is the only site in the human body to observe vasculature noninvasively directly, the fundus can be observed directly for disease diagnoses, such as diabetic retinopathy [10], [11], hypertension [12], heart diseases and stroke [13], and dementia [14], [15].

1.2 Scattering in Fundus Tissues for Disease Diagnosis

Although recent trends in fundus camera development are miniaturization, pupil tracking, sharper images, and cost reduction using smartphones [16]–[19], few studies about the blood lipid concentration detection by the fundus camera were reported. As shown in Fig. 1.1 [20], the fundus of the human eye includes the retina, optic disc, macula, fovea, posterior pole, and so on [21], in which the retina is the inner layer of tissue in the human eyeball with high sensitivity to light. The choroid, a middle layer of tissue behind the retina, also has a scattering coefficient close to the retina, which can vary from 8 mm^{-1} to 14 mm^{-1} for different wavelength light illumination [22]–[26].

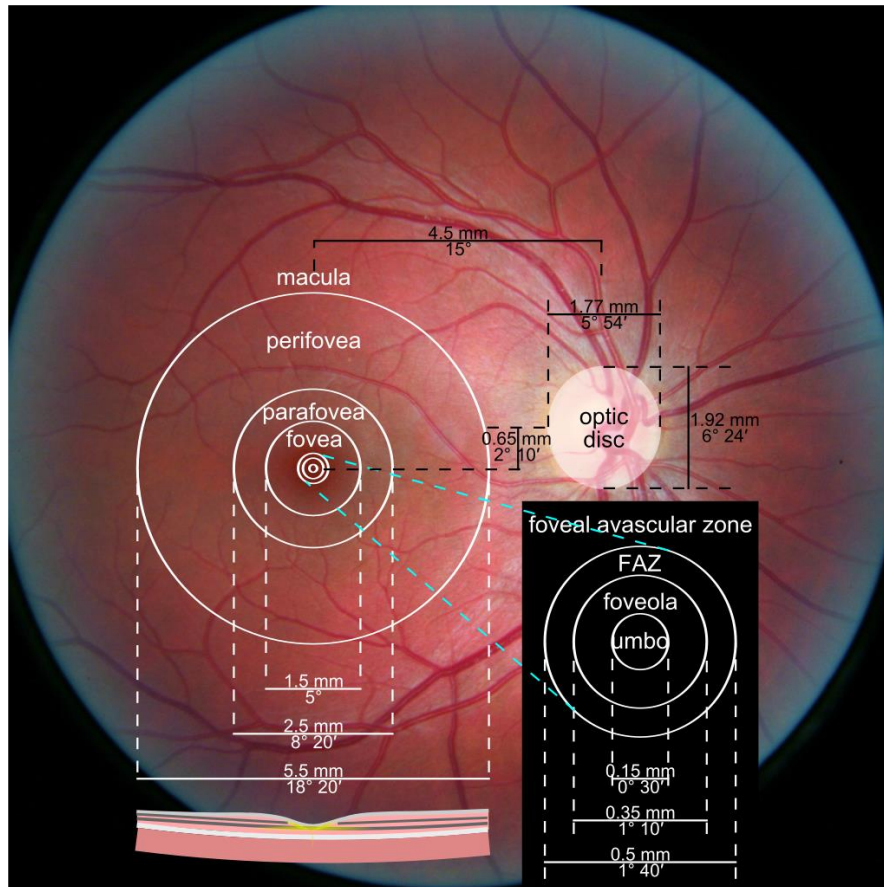


Fig. 1.1 Photograph of the retina of the human eye, with overlay diagrams showing the positions and sizes of the macula, fovea, and optic disc [20].

The fundamental optical properties of fundus tissues can be applied to disease diagnoses [26]. The absorption and scattering properties in the fundus are related to histopathologic observation [27]. Furthermore, a device application for lipid concentration detection by detecting the scattering properties has been reported [28], as shown in Fig. 1.2. To simulate the scattering properties of the fundus tissues and blood, Intralipos was applied for the scattering experiment [29]. The reduced scattering coefficient is a parameter of scattering properties to describe the diffusion of photons in a random walk of step size [30]. The human blood with different reduced scattering coefficients can reveal how the photons transport in the human blood, which can reflect the information of the components in the human blood. For example, dementia is a disease associated with systemic vascular factors and cerebrovascular disease [31],

[32].



Fig. 1.2 Photograph of the device for lipid concentration detection by detecting the blood scattering properties [28].

Since the retina is considered as an extension of the central nervous system due to the homology between the fundus and cerebrovascular system [33], [34], the fundus vasculature factors can be a window to reflect the condition of the cerebral vasculature [16], [35], [36]. Several articles also demonstrated the blood lipid concentration estimation by image processing, this also provides a good way for fundus blood lipid concentration detection, but the complex system operability and low experimental repeatability are still difficult for repetitive experiment data collection [37], [38], as shown in Fig. 1.3. Fig. 1.3(a) shows the schematic diagram of the near-infrared (NIR) hyperspectral imaging system. The structure of this system is similar to the fundus camera, which is illumination and imaging simultaneously. With the captured image and developed model, the lipid content in mouse liver can be estimated, as shown in Fig. 1.3(b). These papers prove that the lipid concentration can be measured by imaging methods. Thus, we seek to design and fabricate a near-infrared fundus camera that can satisfy the basic requirements for fundus observation while also being compact and easy to operate for scattering

detection.

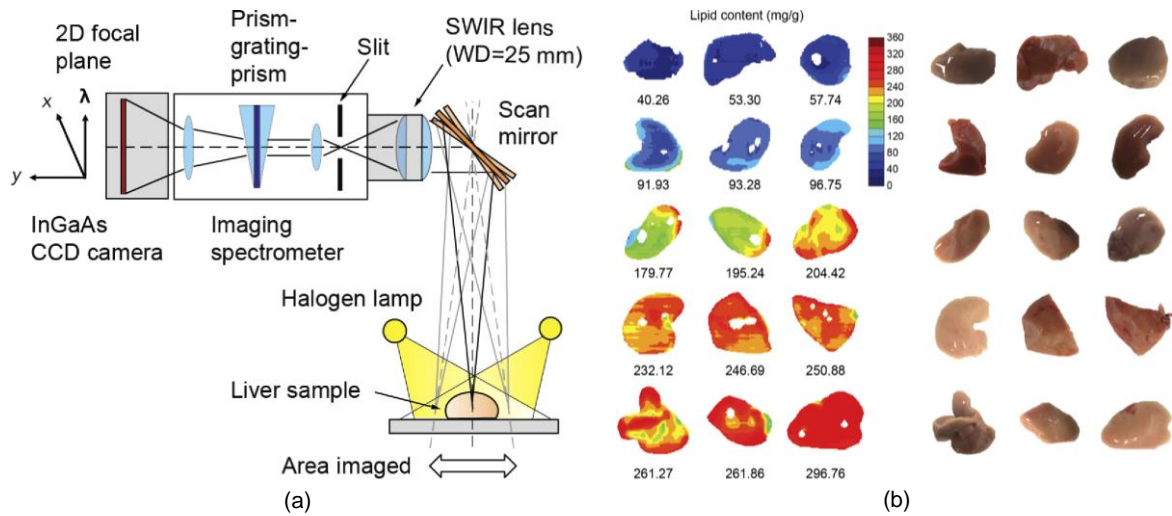


Fig. 1.3 (a) Schematic diagram of the near-infrared hyperspectral imaging system. (b) Visualization of the lipid content in mouse liver. The quantitative mapping of the lipid content in the liver samples is shown in the left, the visible images of the liver samples are shown in the right [37].

1.3 The Principle of Interference Filter

In this research, we selected the interference filter as the projection mask to achieve the pattern projection on the fundus. Though both the absorption filter and interference filter can satisfy the selection requirements of wavelength transmission, we selected the interference filter because it has narrower bandwidth, especially in the NIR band [39], [40], high transmittance, and easy specific pattern formation. Like shown in Fig. 1.4, the wide half bandwidth of the absorption filter is easier to lead to interaction between the neighboring wavelengths during the patterned fundus illumination. Compared to interference filter, due to most of the absorption materials, like dyes and pigments, are liquid state, the specific pattern formation during the fabrication of absorption filter is harder to control. Thus, we finally selected the interference

filter for patterned fundus illumination.

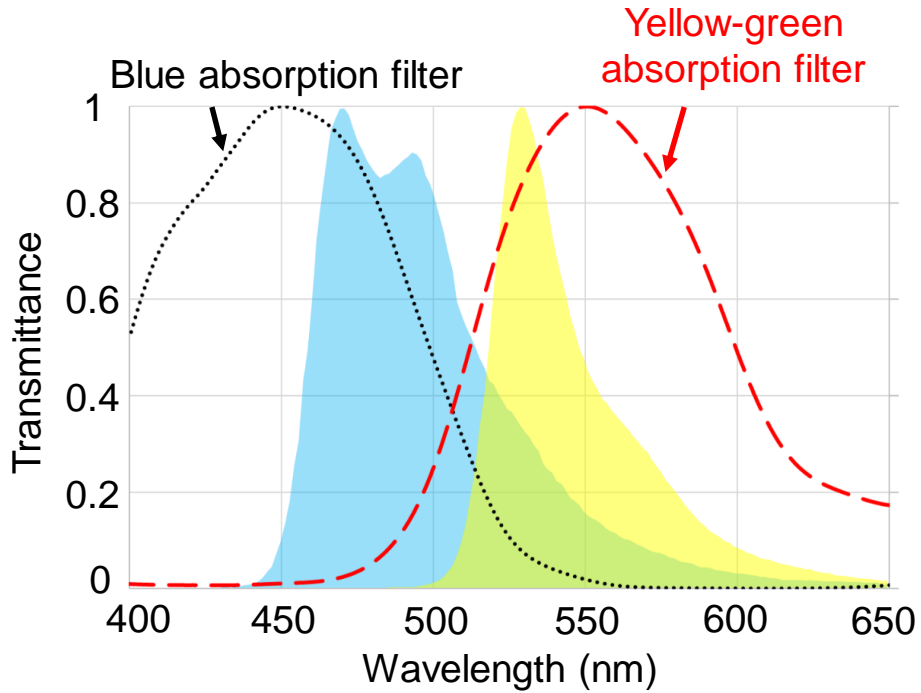


Fig. 1.4 Transmission spectrum of blue absorption filter and yellow-green absorption filter [39].

The interference filter is a filter consisting of multilayers with different refractive indices to transmit specific spectral bands while maintaining a low absorption. The multi-reflection in the interface of different refractive index films causes the various transmittance at wavelengths. As shown in Fig. 1.5, the optical path difference of the adjacent reflection light R_1 and R_2 in the high refractive index film is shown in Equation 1.

$$\Delta L = 2n_H l_H \cos \theta \quad (1)$$

where the n_H is the high refractive indices, l_H is the thickness of the high refractive index film, and θ is the refractive angle when the incident light from low refractive index film to high refractive index film. The phase difference of the adjacent reflection light can be described as Equation 2 without phase shift [41].

$$\delta = \left(\frac{2\pi}{\lambda}\right) \Delta L \quad (2)$$

where the λ is the wavelength of the incident light. Thus, the transmittance of the light can be described as Equation 3 [39].

$$T = \frac{1}{1 + F \sin^2\left(\frac{\delta}{2}\right)} \quad (3)$$

where $F = \frac{4R}{(1-R)^2}$, R is the reflection. According to these equations, only the phase difference, and more specifically is the optical path difference, can affect the wavelength transmittance. The transmittance is highest when the optical path difference is an integer multiple of the incident light wavelength. Conversely, the transmittance is zero when the optical path difference is half-odd multiples of the incident light wavelength. Thus, the selection of the wavelength transmittance is achieved by the interference filter.

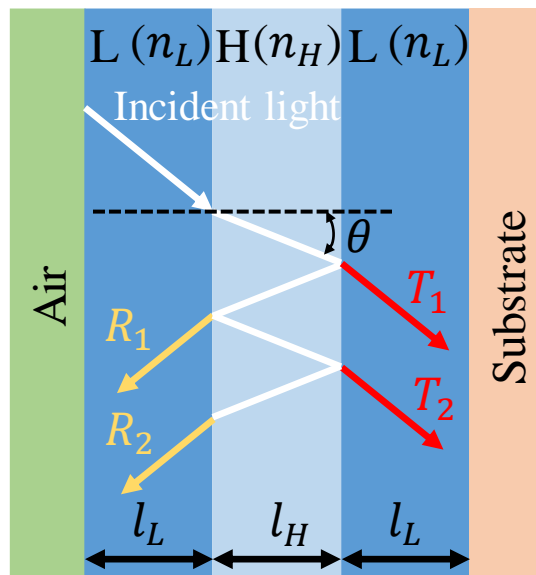


Fig. 1.5 Schematic diagram of the reflection and transmission in the interference filter.

1.4 The Purpose of This Research

A NIR fundus camera has been developed to acquire colorized images of the interior of the human eye using only NIR illumination in our laboratory [18], [43]. Compared with the commercial portable fundus camera shown in Fig. 1.6 [44], the proposed NIR fundus camera can avoid irritation of the eyes, as the human eyeball is insensitive to NIR light, thereby making it easier to perform observations of the fundus. Since the fundus to be observed is composed of the vasculature, optic disc, and other tissues with different refractive indices, there is a possibility to check the health condition by analyzing the state of the scattered light from the fundus. Thus we proposed a noninvasive method for fundus scattering detection using the NIR fundus camera with a patterned interference filter. Compared with conventional methods for lipid concentration measurement in human blood, the proposed method can detect the scattering information noninvasively directly for lipid concentration measurement. The complex operation and physical pain of patients in blood collection can be avoided. Furthermore, with the help of a selfie fundus camera, self-detection of lipid concentration is possible.

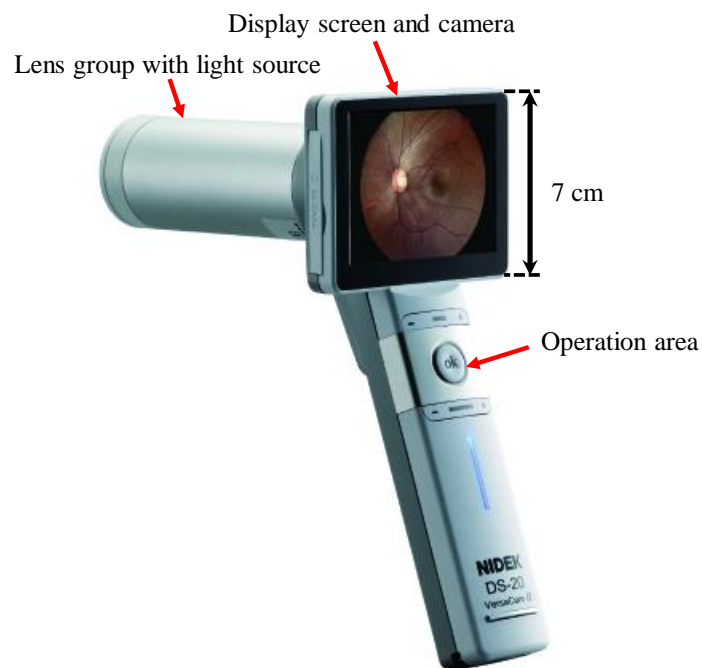


Fig. 1.6 Photograph of the commercial portable fundus camera with visible light illumination [43].

1.5 Thesis Outline

There are six chapters in this thesis, the brief outline of these six chapters is shown as follows.

Chapter 1: Introduction

This chapter introduced the development of the fundus camera in more than one century. Besides that, studies about the scattering information of fundus tissues for diseases diagnosis were provided, these studies prove the feasibility of lipid concentration measurement by imaging methods. Then, the reason for selecting the interference filter for pattern projection and its principle for wavelength selection were introduced. The purpose of this research is presented in the last.

Chapter 2: The multi-spectral NIR fundus camera system for fundus observation

The design and fabrication of the NIR fundus camera for fundus observation are introduced in this chapter. The fundus camera is evaluated both in the numerical optical simulation and fundus observation. The details of the numerical optical simulation and fundus camera assemble are presented in this chapter.

Chapter 3: Pattern projection on the fundus

This chapter presents a NIR fundus camera with a patterned metal mask for pattern projection on the fundus. Following the numerical optical simulation results and human fundus structure, the layout of the projection mask is designed. The patterned metal mask fabricated following the layout is added to the NIR fundus camera for pattern projection on the fundus and scattering detection. Furthermore, the preparation of artificial blood for scattering detection is presented. The details and results of the pattern projection on the fundus and scattering detection are introduced in this chapter.

Chapter 4: A multi-functional filter for patterned fundus illumination

This chapter presents the design, fabrication, and evaluation of the multi-functional interference filter. In the design part, the mask layout is optimized following the results in Chapter 3, and the transmittance spectrum of every area in the multi-functional interference filter is simulated. In the fabrication part, the main fabrication procedures are introduced. The fabrication process is evaluated by comparing the semi-finished interference filter transmission spectrum of the measurement and simulation, which is shown in the appendix. Finally, in the evaluation part, the fabricated multi-functional interference filter is evaluated by comparing the transmission spectrum in measurement and simulation. The constant parameters during the fabrication process are presented in this chapter.

Chapter 5: Scattering detection by pattern projection

This chapter presents the pattern projection on the fundus and scattering detection by the NIR fundus camera with the fabricated patterned interference filter. The scattering results prove the feasibility of the lipid concentration measurement by the multi-spectral NIR fundus camera with a patterned interference filter. The details of the pattern projection and scattering results are presented in this chapter.

Chapter 6: Conclusion

This chapter summarizes all the research results in this thesis and presents the future plan of this research.

2. The Multi-spectral NIR Fundus Camera for Fundus Observation

2.1 Prototype NIR Colorized Fundus Camera

The prototype NIR color fundus camera developed by our laboratory is an adaptation of a reflex-free indirect ophthalmoscope and based on multi-spectral color imaging (combined with NIR colorization technology), which can be separated into a fundus illumination system and a fundus imaging system [17][18]. The schematic diagram of the prototype NIR color fundus camera is shown in Fig. 2.1. The overlapped optical path in these two systems is from beam splitter to eyeball fundus.

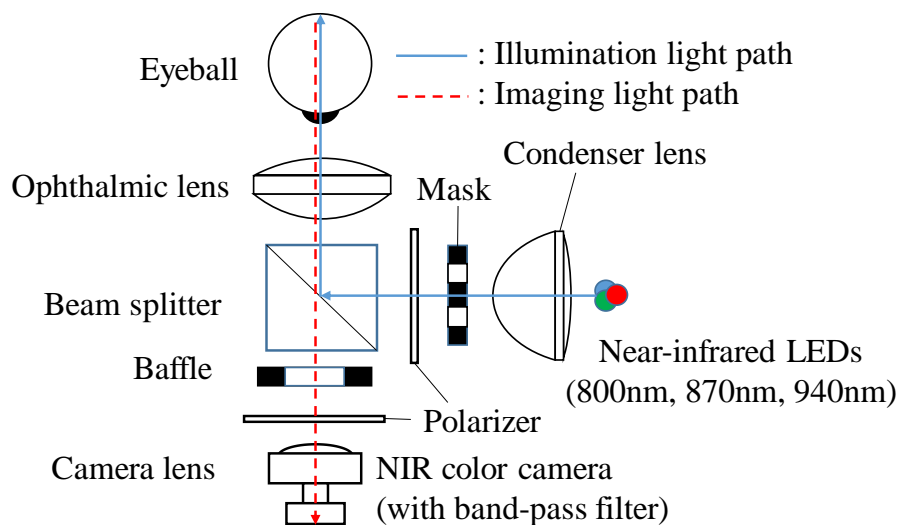


Fig. 2.1 Schematic diagram of the prototype NIR color fundus camera developed by our lab.

The NIR colorization technology, which includes NIR LEDs (800 nm, 870 nm, and 940 nm) and a NIR color camera with a band-pass filter, can get color fundus images with only NIR illumination light. The camera mentioned above has a prism in front of the three image sensors to divide NIR light into three NIR bands, which are NIR1 (800 nm), NIR2 (870 nm), and NIR3

(940 nm), and deliver them to the corresponding image sensors. The NIR1, NIR2, and NIR3 image sensors can acquire signals correlated to red, blue, and green, respectively [45]. To get color fundus images, the reflected light wavelengths from the retina should be the same as NIR1, NIR2, and NIR3. The NIR band illumination light can avoid irritation to the human eyeball and make the fundus observation easier. The color fundus image, taken by the fundus camera mentioned above is shown in Fig. 2.2, shows a clear optic disc and vasculatures, proving the feasibility of fundus observation by the prototype NIR color fundus camera [17].

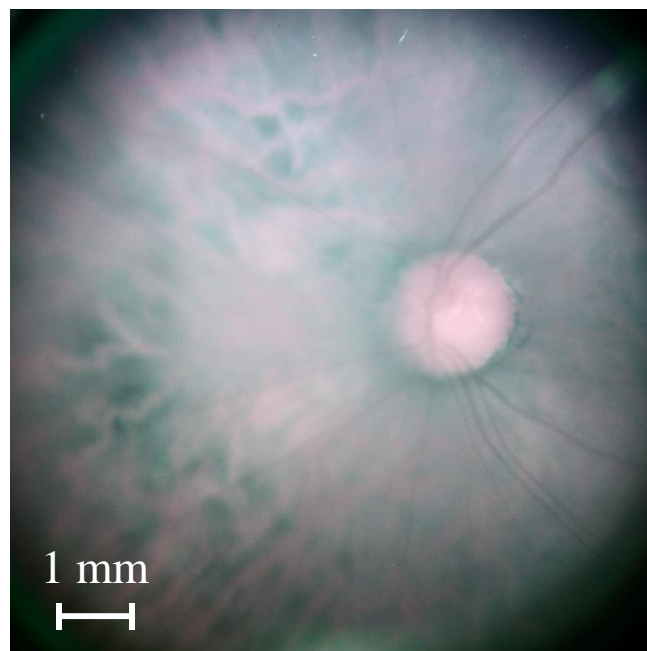


Fig. 2.2 The color fundus image taken by the prototype NIR color fundus camera without visible illumination light.

2.2 Optical Simulation of the Fundus Camera

2.2.1 Components Selection by Optical Simulation

The numerical optical simulation of the fundus camera in this thesis was simulated by an optical design software ZEMAX. The Arizona eye model was applied in the numerical optical

simulation [46], [47]. Figure 2.3 shows the schematic diagram of the fundus camera in the numerical optical simulation, composed of a fundus illumination system and a fundus imaging system. The fundus illumination system includes a uniform illumination system composed of a diffuser and two condenser lenses to uniform the fundus illumination light. The two condenser lenses are to convert the diverging beam from the light source into a roughly parallel beam for fundus illumination. The diffuser is to decrease the effect of ghost images caused by the light source and increase the uniformity of the illumination light. The polarizer prevents stray light into the camera. The ophthalmic lens is used for the Maxwellian view illumination which achieves convergent illumination light in front of the cornea [48]. Thus, the annular illumination beam from the mask can illuminate the retina without the back reflection from the cornea. The beam splitter is a vital sharing standard optic in the fundus camera for illumination and imaging simultaneously. In Fig. 2.3, the light path through the beam splitter is omitted and only the reflected light path is considered to avoid confusion. The split ratio of the beam splitter in numerical simulation is set as 50:50 to increase the energy utilization rate of the illumination light. The aperture is to control the field of view of the camera and decrease the stray light from

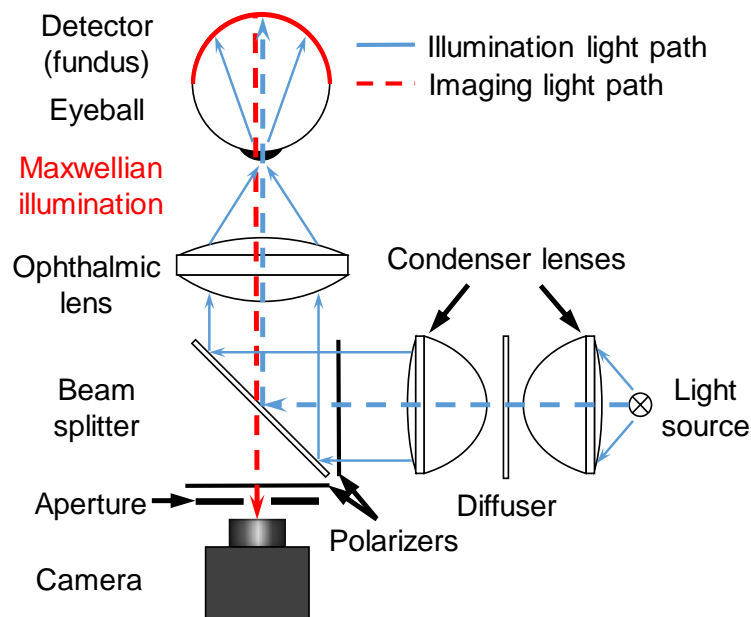


Fig. 2.3 Schematic diagram of the fundus camera system in the numerical optical simulation.

the external environment.

2.2.2 Evaluation of Simulation Results

The wavelength in the simulation for fundus illumination was set as 800 nm; the reason for selecting the wavelength will be explained in section 3.4. The eyeball radius in the simulation is 13.4 mm, and the back half of the eyeball is set as a detector. The irradiance distribution of the illumination light on the detector is shown in Fig. 2.4(a). In this research, the uniformity of the irradiance beam was selected as the parameter to evaluate the fundus illumination. The distribution map shows a round shape irradiance distribution, in which the radius less than 8 mm has a uniform distribution compared with other areas, this area is selected as the illumination area, like shown in the blue circle in Fig. 2.4(a). The imaging area radius is about 6 mm, like shown in the green circle in Fig. 2.4(a). As shown in Fig. 2.4(a), the cross-section row data at the position where the Y coordinate value is zero was collected. Then the collected data was applied to evaluate the uniformity of the incoherent irradiance distribution on the detector, as shown in Fig. 2.4(b). The uniformity of the irradiance distribution of the

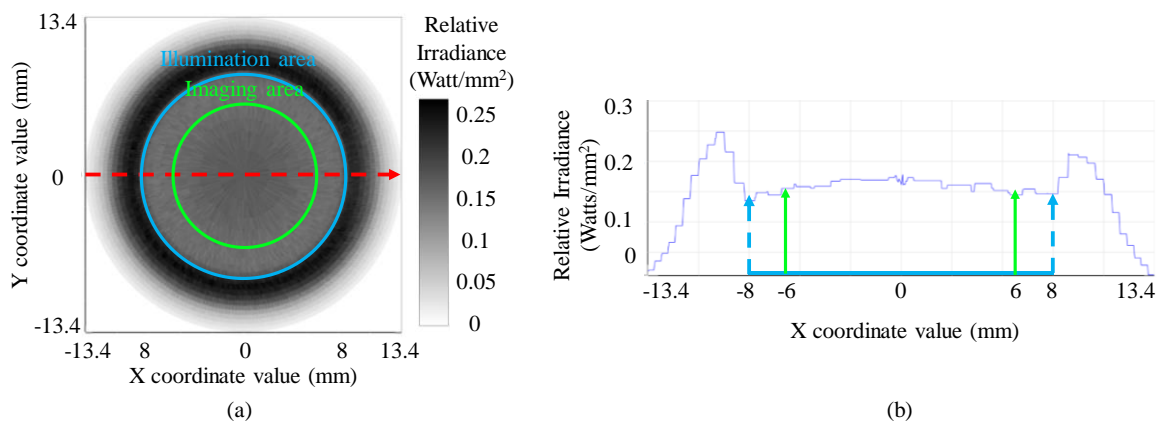


Fig. 2.4 The incoherent irradiance distribution of (a) the illumination light on the detector and (b) cross-section row on the detector in numerical optical simulation.

illumination area in the numerical optical simulation is calculated according to the formula shown below [1][49]:

$$U = 1 - \frac{|\phi_{Center} - \phi_{85\%}|}{\phi_{Max}} \quad (4)$$

where U is the uniformity of the illumination beam, ϕ_{Center} is the irradiance at the center of the selected illumination area, $\phi_{85\%}$ is the irradiance at 85% of the selected illumination area radius, and ϕ_{Max} is the maximum irradiance in the selected illumination area. The uniformity of the irradiance distribution on the illumination area in simulation is 90.1%, which is high enough for uniform fundus imaging [50]. Thus, the calculated uniformity proves the feasibility of the uniform fundus illumination in the numerical optical simulation by this fundus camera.

2.3 Configuration of the Fundus Camera

The assembly of the fundus camera system is presented in this section. The system assembly was carried out following the numerical optical simulation mentioned above. The light source in the fundus camera is a four-band LED with 780 nm, 800 nm, 850 nm, and 940 nm wavelength for NIR color fundus imaging, which is shown in Fig. 2.5. The part number of the optical components in the fundus camera is shown in Table 2.1. A photograph of the assembled fundus camera is shown in Fig. 2.6. The system imaging test will be presented in section 2.4.

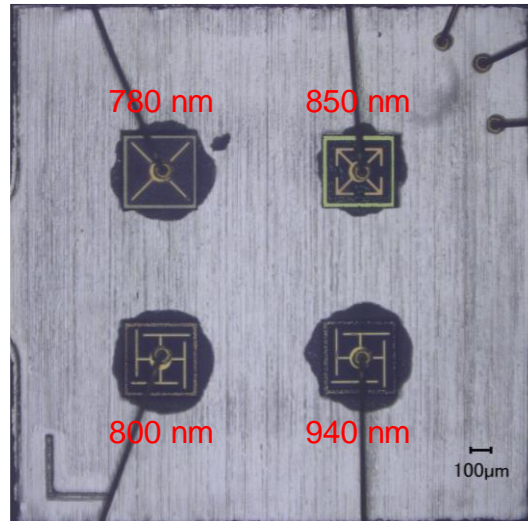


Fig. 2.5 Photograph of the four bands LED in the fundus camera for illumination.

Table 2.1 The part number of optical components in the fundus camera.

Optical component	Part number	Company
Light source	Custom-made product	Yellow Stone Corp.
Condenser lens	ACL25416-B	THORLABS
Diffuser	DG10-120-B	THORLABS
Beam splitter	BSW26R	THORLABS
Ophthalmic lens	V40LC	VOLK
Camera	Color Night Vision	Nanolux
Camera lens	LMVZ990-IR	KOWA

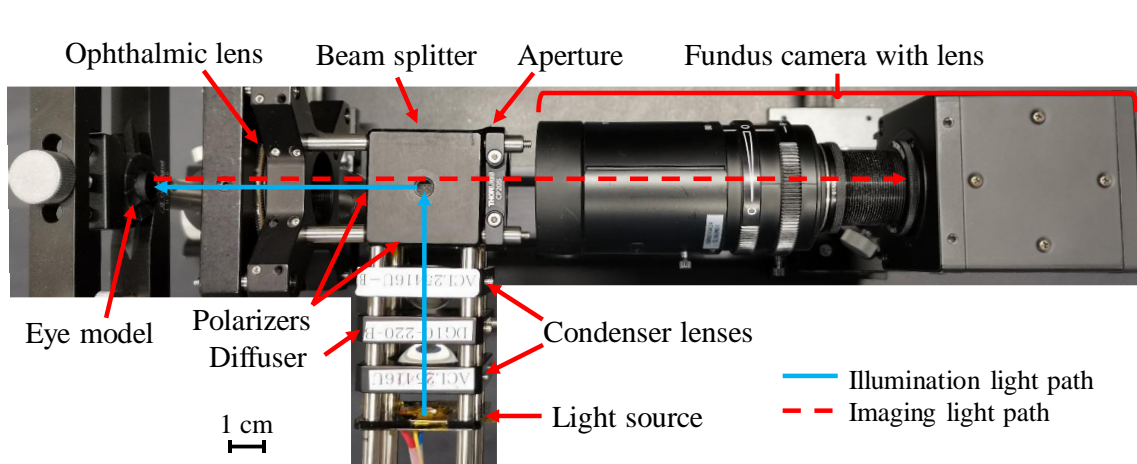


Fig. 2.6 Photograph of the assembled fundus camera following the optical simulation.

2.4 Fundus Imaging by the Fundus Camera

The fundus imaging by the assembled fundus camera is presented in this section. Since the optics in the assembled fundus camera always have some distance deviations compared with the simulation results, an eye model was applied to the fundus camera to calibrate the potential distance error. According to the sharpness of the eye model fundus image captured by the camera, the distance between the optics was fine-tuned for a clear fundus image. The eye model in this research is shown in Fig. 2.7. The fundus image of the eye model after distance adjustment is shown in Fig. 2.8. The clear optic disc and fundus vasculature prove that the assembled fundus camera performs well for eye model fundus observation.

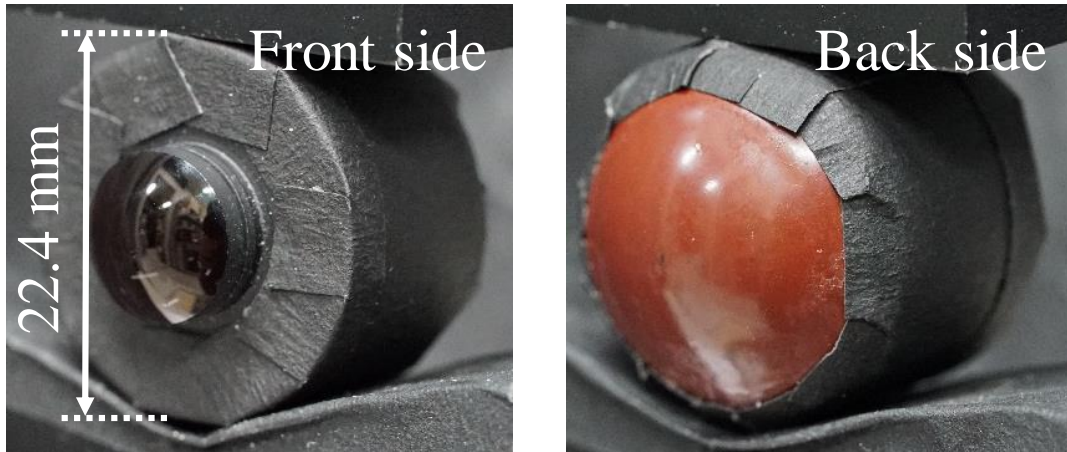


Fig. 2.7 Photograph of the eye model in this research from the front and back sides.

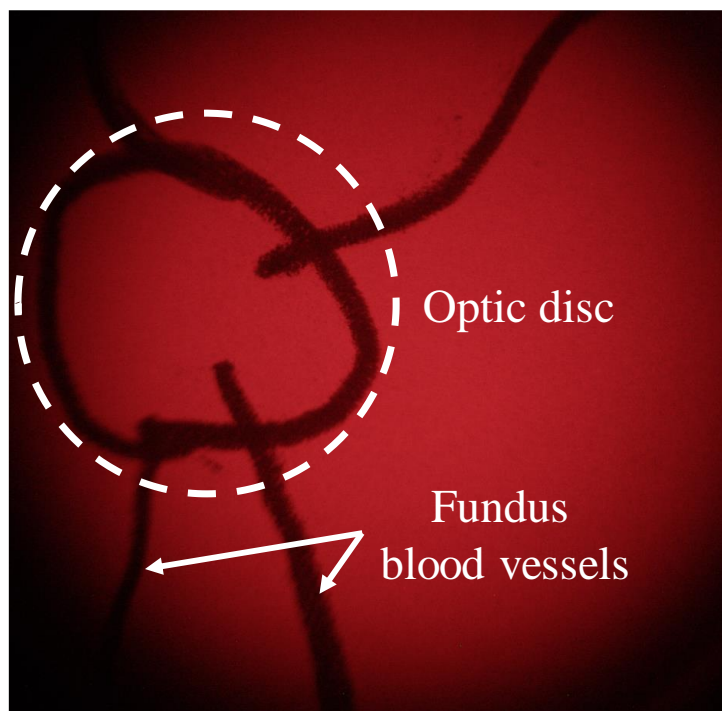


Fig. 2.8 Clear fundus image of the eye model taken by the assembled fundus camera after calibration.

After the fundus camera calibration and eye model fundus imaging, the fundus camera was applied to the human eyeball for fundus observation. The fundus image of the human eyeball is shown in Fig. 2.9. The clear optic disc and fundus blood vessels prove that the

assembled fundus camera has high performance for fundus observation. Besides the optic disc and fundus blood vessels, the observed retina and choroid can also be applied to disease diagnosis.

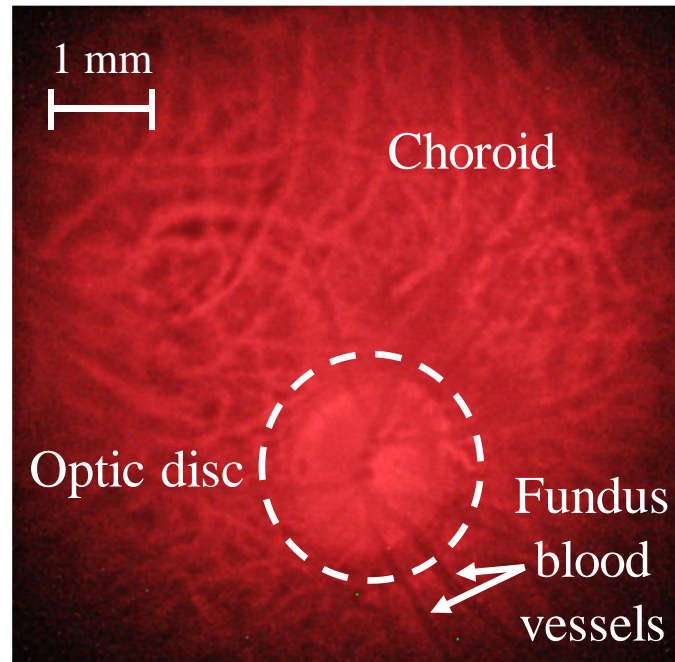


Fig. 2.9 Fundus image of a human eyeball taken by the assembled fundus camera.

2.5 Summary and Discussion

The design and fabrication of the fundus camera for fundus observation were presented in this chapter. The optical structure of the fundus camera for fundus observation was simulated by ZEMAX. The calculated uniformity of the irradiance distribution on the detector is higher than 90%, which means the uniform fundus illumination is available by this fundus camera in the numerical optical simulation. Furthermore, the fundus camera assembled following the simulation results was applied to the fundus observation of the eye model and human eyeball. The clear optic disc and fundus blood vessels demonstrate the high performance of the fundus camera in fundus observation. Besides the optic disc and fundus blood vessels, the observed

retina and choroid in the fundus image prove the feasibility of the fundus camera in disease diagnosis.

This research followed the Ethical Guidelines for Medical and Health Research involving Human Subjects at the Nara Institute of Science and Technology.

3. Pattern Projection on the Fundus

3.1 Overview

The fundus is the only site in the human body to observe arteries and capillaries noninvasively directly. The observation of the fundus is an essential way for disease diagnosis. Though fundus images can reveal the type of disease according to the strange characteristics of the fundus, which is also related to the doctor's experience, the health condition check and disease prevention are still hard to achieve only through fundus observation. Thus, we proposed a fundus camera with a projection mask for fundus patterned illumination to analyze the scattering from the retina. The structure of the fundus camera was modified for linear stripe patterned illumination in the numerical optical simulation. A projection mask was designed and added for linear stripe patterned illumination and to decrease the unconscious movement of the human eyeball. Furthermore, this chapter also demonstrated the feasibility of linear stripe patterned illumination by the assembled system for scattering detection. Figure 3.1 shows the outline diagram of this chapter.

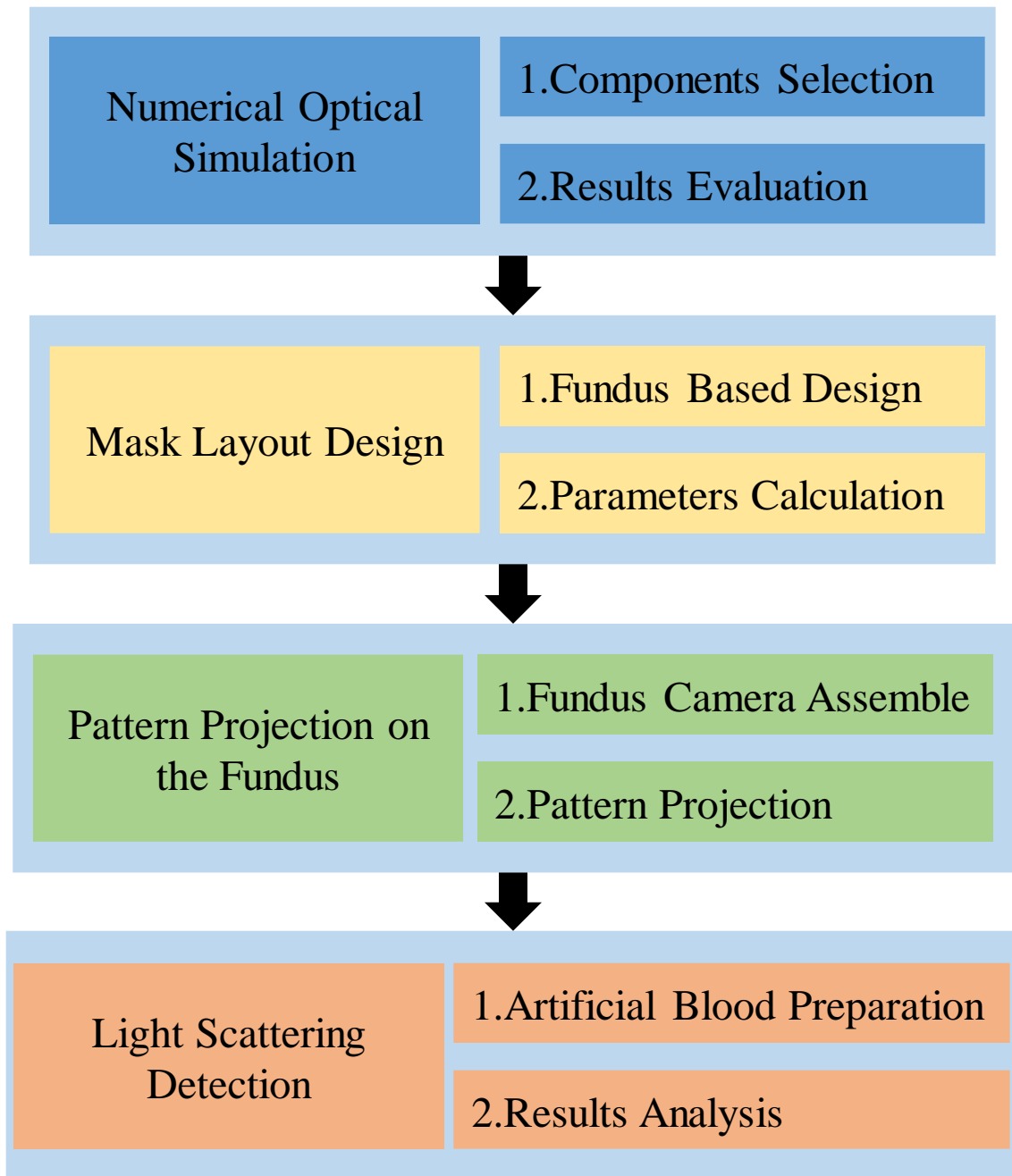


Fig. 3.1 Outline diagram of the contents in Chapter three.

3.2 Optical Design Modification for Fundus Pattern Projection

3.2.1 Components Selection

The numerical optical simulation of the fundus camera with a projection mask was simulated by ZEMAX. The Arizona eye model was applied in the numerical optical simulation. To achieve the fundus patterned illumination, a patterned illumination system, which includes a projection mask and a lens group, was added to the fundus camera. The patterned illumination system was used for generating a linear stripe patterned illumination beam to check and eliminate the distortion of the projected pattern on the detector. The linear stripe pattern in the projection mask consists of the repetition of a 1.25 mm line and 1.25 mm space pattern. In the simulation to check the shape of the pattern on the projection mask, the parallel light generated by a rectangle light source passes through the projection mask vertically and collected by a rectangle detector. In the numerical optical simulation, the parameters of the projection mask were set as follows: X full width is 16, and aspect ratio is 1. The image of the projection mask on the detector is shown in Fig. 3.2.

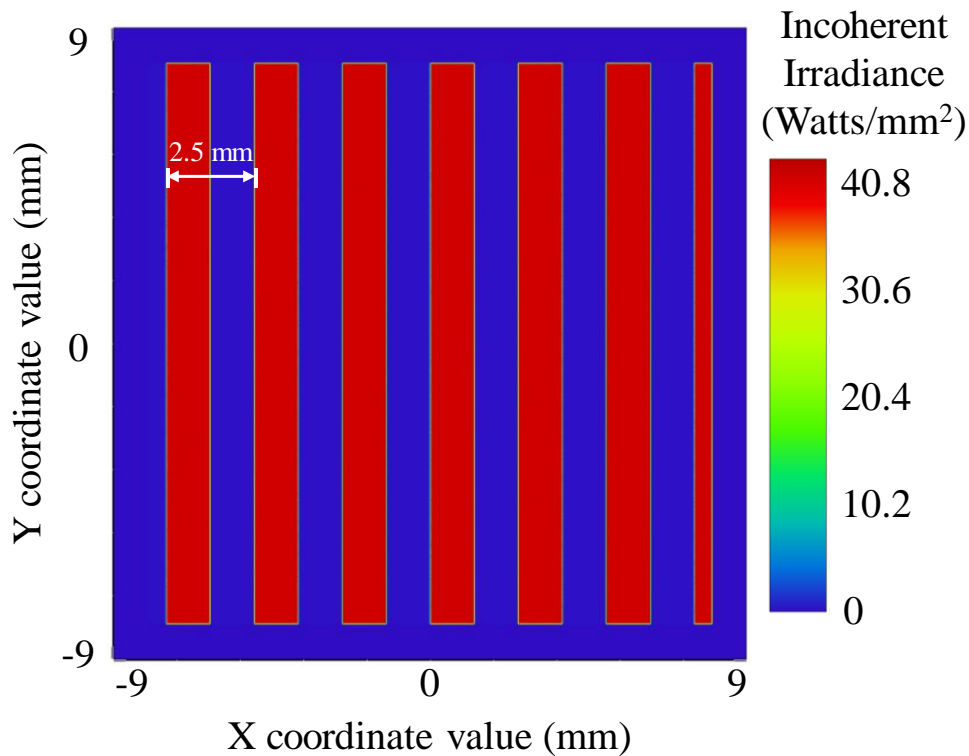


Fig. 3.2 The pattern of the projection mask projected on the detector in the fundus camera numerical optical simulation.

As for the lens group, we selected a bi-convex lens (LB1761-B, THORLABS) and a positive meniscus lens (LE1234-B, THORLABS) for patterned projection on the detector and the calibration of aberration. All the optical path in the simulation was calculated according to the lens parameters. The part numbers of condenser lens, diffuser, beam splitter, and ophthalmic lens are shown in Table 2.1. Regarding the position, the projection mask was set right behind the second condenser lens, and the lens group was placed between the projection mask and the beam splitter. Figures 3.3 and 3.4 show the schematic diagram of the fundus camera with a projection mask and the pattern projected on the detector in the numerical optical simulation, respectively. The apparent boundaries between the adjacent linear stripes on the detector verified the feasibility of the linear stripe patterned illumination by the fundus camera with a projection mask in the numerical optical simulation. Figure 3.5 is the pattern projected on the detector by the fundus camera without the meniscus lens. Compared with the straight stripes in

Fig. 3.4, the distortion in the projected pattern proves the significance of the meniscus lens in pattern projection on the fundus.

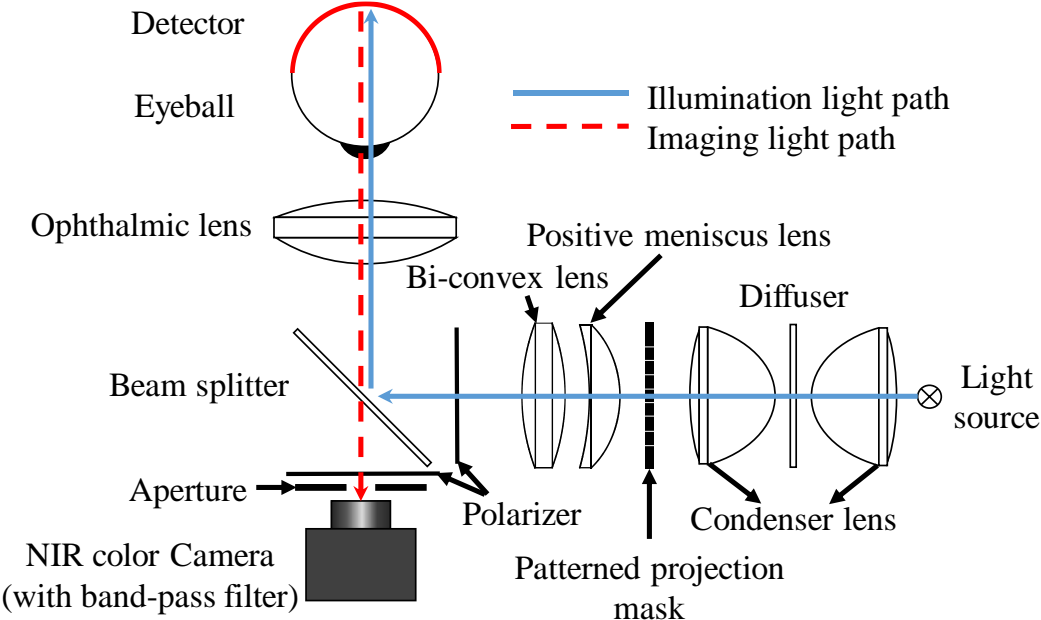


Fig. 3.3 Schematic diagram of the fundus camera with a projection mask in numerical optical simulation.

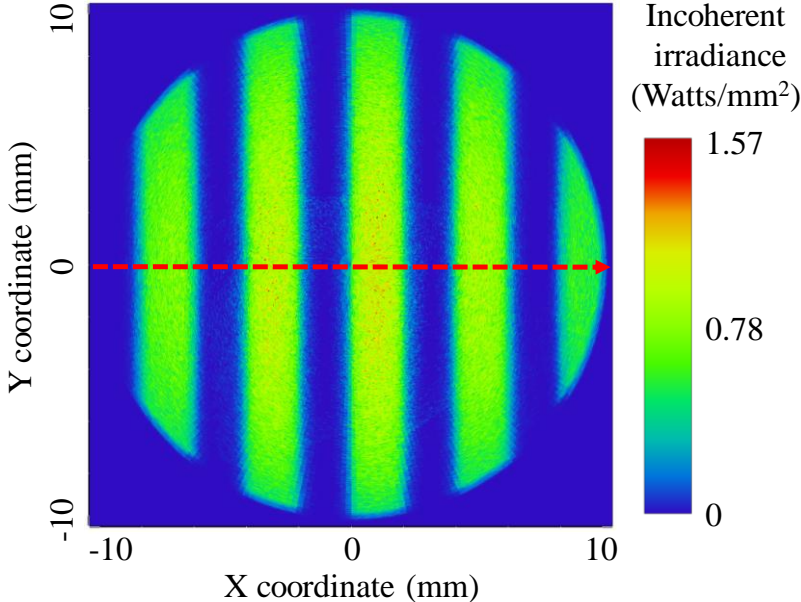


Fig. 3.4 Linear stripe pattern on the detector in the numerical optical simulation. The widths of the lines of the projection and the spaces between them are 1.25 mm.

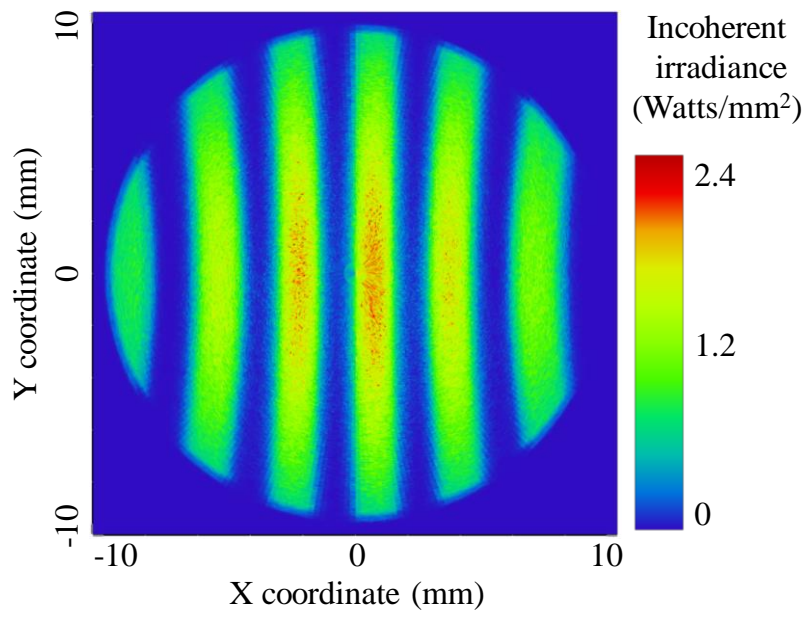


Fig. 3.5 Linear stripe pattern with distortion on the detector in the simulation by the fundus camera without meniscus lens.

3.2.2 Evaluation of Simulation Results

As mentioned previously, the uniformity of irradiance distribution was selected as the parameter to evaluate the pattern projected on the detector in numerical optical simulation. Since the vacant illumination light intensity exists between the adjacent linear stripe pattern, the uniformity of the linear stripe patterned illumination light is no longer essential to evaluate the fundus illumination. As shown in Fig. 3.4, the cross-section row data at the position where the Y coordinate value is zero was collected. Then the collected data was applied to evaluate the fundus illumination, as shown in Fig. 3.6. Figure 3.6 shows that the radius of the valued linear stripe patterned illumination area is larger than 9 mm, which is satisfy the requirements of fundus illumination. Furthermore, the obvious boundary between the peak and valley of the irradiance in Fig. 3.6 demonstrates the feasibility of the pattern projection on the fundus in the optical numerical simulation.

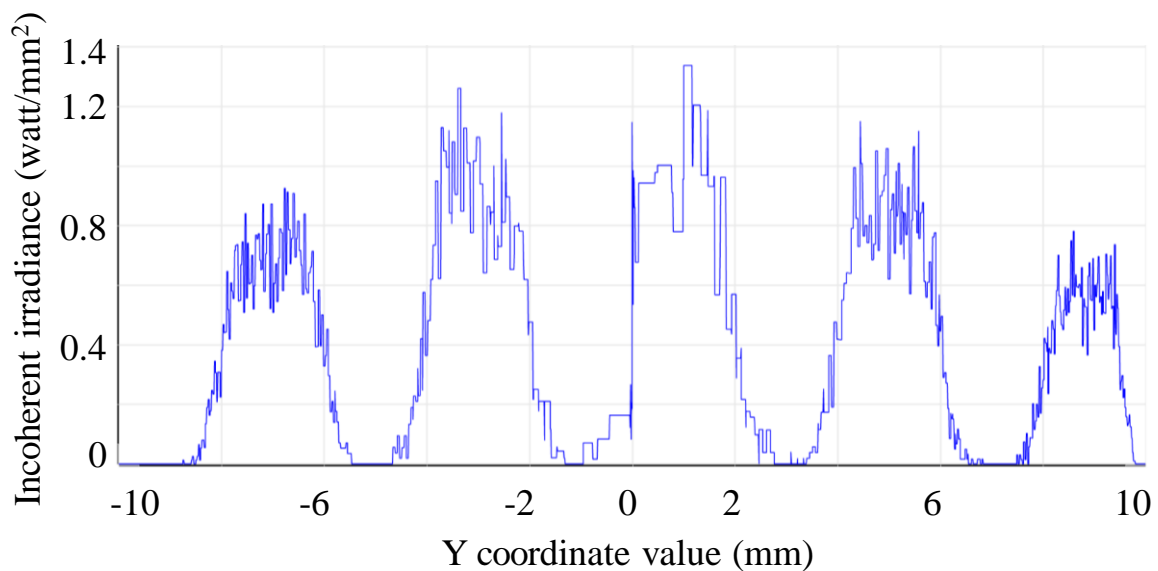


Fig. 3.6 The cross-section column incoherent irradiance distribution of the linear stripe patterned illumination beam on the detector in numerical optical simulation.

3.3 Design of the Projection Mask

Following the simulation results, the layout of the projection mask was designed, and a layout-based patterned metal mask was fabricated to test the feasibility of linear stripe patterned fundus illumination.

3.3.1 Fundus Based Layout Design

The layout of the projection mask includes three areas, which are designed according to human eyeball structure. Figure 3.7(a) shows the image of the human eyeball retina, which was captured by a commercial portable fundus camera (DS-20 VersaCam, NIDEK) with a visible light source. The optic disc, fovea, and other tissues can be observed clearly from the fundus image. According to previous research, the mean distance between the fovea and the optic disc center (DFD) is 4.76 ± 0.34 mm [51].

There are variations in the retinas, and it is essential to ensure the linear stripe illumination light can illuminate the fundus blood vessels. The linear stripe pattern was designed to improve the possibility of illuminating the fundus vasculature perpendicularly. We were mainly concerned with two areas in fundus for the patterned mask layout design: optic disc area and fovea area. The optic disc area in the fundus contains the optic disc, fundus tissues, and fundus blood vessels. The fundus blood vessels are converged in the optic disc such that when the linear stripe patterned illumination light illuminates the optic disc area, there is a higher possibility to illuminate the blood vessels perpendicularly than the other patterns. To place the linear stripe pattern on the optic disc area, an eyeball fixation target was designed in the layout of the projection mask. The eyeball fixation target will appear on the fovea (i.e., the center of sight) when a patient's eye gazing on the eyeball fixation target. This allows the linear stripe patterned illumination light to illuminate the optic disc area simultaneously, as shown in Fig.

3.7(b). Different layouts with different relative distances between the eyeball fixation target and the linear stripe patterns were designed to ensure that at least one of the linear stripe patterns can suit a specific patient. Furthermore, because the unconscious movement of the eyeball has a significant influence on the captured fundus image [52], the eyeball fixation target helps fix the eyeball's gazing position to decrease this effect.

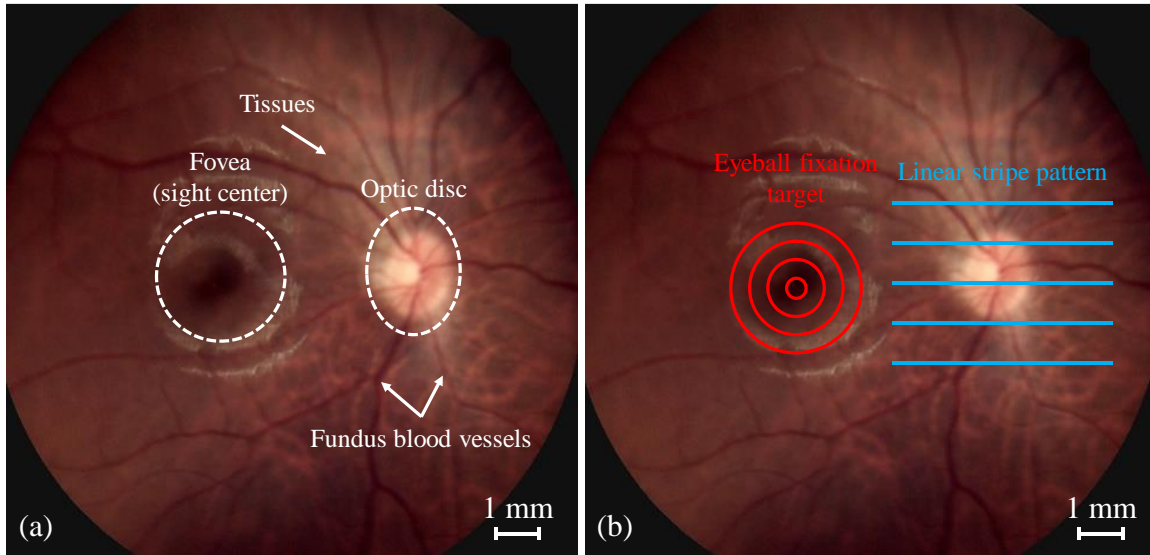


Fig. 3.7 (a) Photograph of the human eyeball retina captured by a conventional fundus camera and (b) schematic of the fundus patterned illumination.

3.3.2 Parameters Selection

The projection mask in numerical optical simulation consists of a repetition of a 1.25 mm line and a 1.25 mm space pattern; following the clear pattern projected on the detector, the layouts of the projection mask were designed. The layouts were designed by an EDA software Virtuoso System Design Platform (Cadence Design System, Inc.). Figure 3.8 shows the three areas in the layouts of the patterned mask: 1) the linear stripe pattern, 2) the eyeball fixation target (donut shape), and 3) the fundus illumination area, comprising the full area illumination. The pitch of the linear stripe pattern in the patterned mask is 1.1 mm (0.1 mm line and 1 mm space), larger than in simulation to prevent the scattering interaction from the adjacent linear

pattern. However, these areas in the patterned metal mask fabricated according to these layouts are not active, which means the linear stripe pattern and eyeball fixation target can transmit all the wavelength light, and the fundus illumination area cannot transmit any wavelength light.

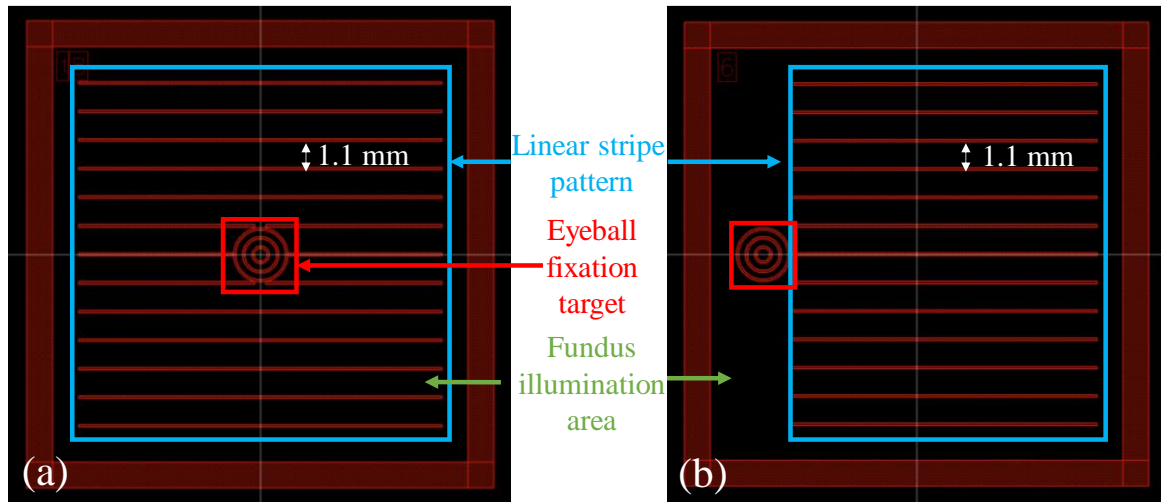


Fig. 3.8 The layouts of the designed patterned mask with three parts.

3.3.3 A Fabricated Patterned Metal Mask

The metal mask for pattern projection on the fundus is fabricated following the designed layout. Figure 3.9 shows the photograph of the fabricated patterned metal mask. The fabricated patterned metal mask includes the linear stripe pattern with a 1.1 mm pitch, and the eyeball fixation target, as shown in Fig. 3.8(b). The fundus illumination area is omitted in the metal mask due to the fundus illumination area is covered by absorption materials, which can absorb all the wavelength bands of light instead of the transmission of the NIR band of light. The fabricated patterned metal mask simplified the function of the projection mask in the design. Compared with the projection mask in the design, the linear stripe pattern and eyeball fixation target can pass through all the wavelengths of light instead of the specific bands of light.

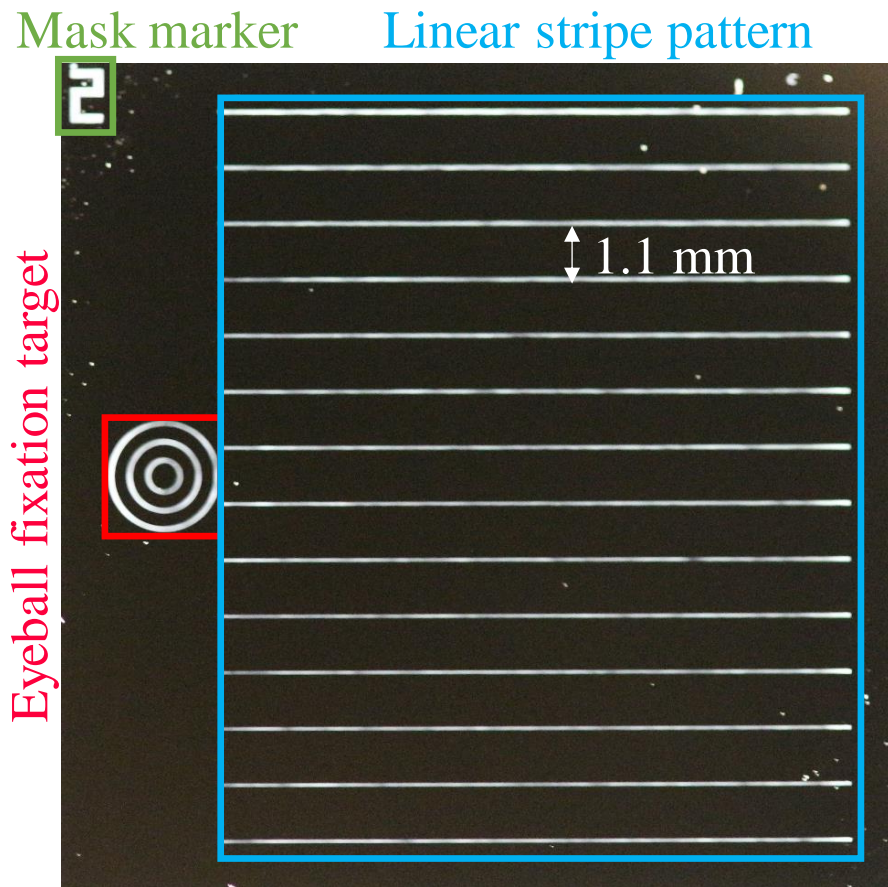


Fig. 3.9 Photograph of the fabricated patterned metal mask.

3.4 Configuration of the Fundus Camera for Pattern Projection

To test the feasibility of the patterned fundus illumination, we conducted a linear stripe patterned fundus illumination experiment using the fabricated patterned metal mask instead of the projection mask in the numerical optical simulation. In this experiment, an 800 nm LED was selected as a light source; the measured emission spectrum is shown in Fig. 3.10. Although the visibility of the emission band owing to its wide half bandwidth is convenient for this experiment, a narrower emission band is preferred for scattering detection. An interference filter was presented in the following chapter to overcome this problem.

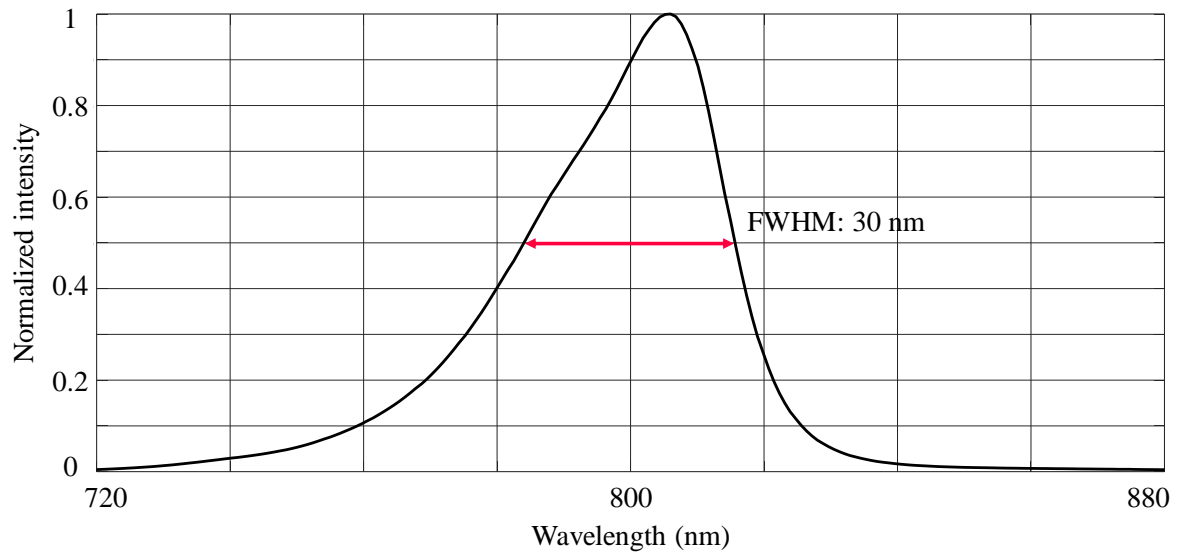


Fig. 3.10 Measured spectrum of the 800 nm LED.

The scattering from the fundus vasculature has an essential role in the fundus scattering. While red blood cells (RBCs) contribute to vasculature scattering, the absorption coefficient of hemoglobin depends upon the incident wavelengths and upon whether it is oxygenated (in the artery) or deoxygenated (in the vein). As shown in Fig. 3.11 [53], [54], when the incident wavelength is around 800 nm, the absorption coefficient is relatively low, and the values for oxygenated and deoxygenated hemoglobin are almost the same, making different absorption coefficients of arteries and veins avoidable [55], [56]. This is one of the reasons for setting the 800 nm LED as a light source. Another reason is that the human eyeball is insensitive to light with a wavelength near 800 nm, which prevents the constriction of the eye's iris. Eye constriction caused by the stimulus from the light source can be eliminated. The fundus camera with a patterned metal mask designed by optical simulation was assembled. Figure 3.12 shows the photograph of the fundus camera with a patterned metal mask.

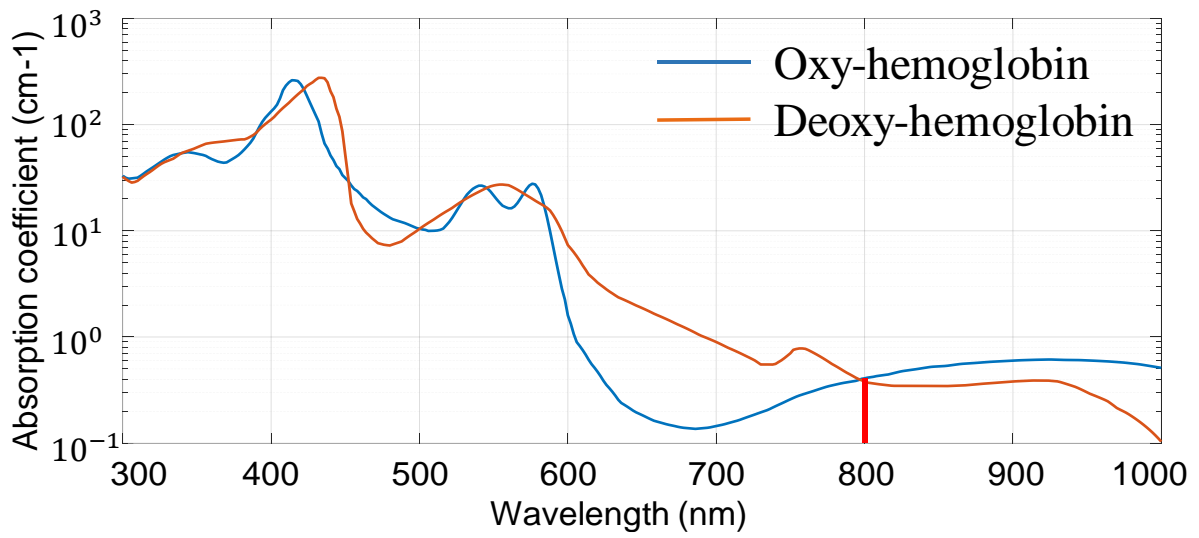


Fig. 3.11 The absorption spectrum of the oxygenated and deoxygenated hemoglobin from 300 nm to 1000 nm [51], [52].

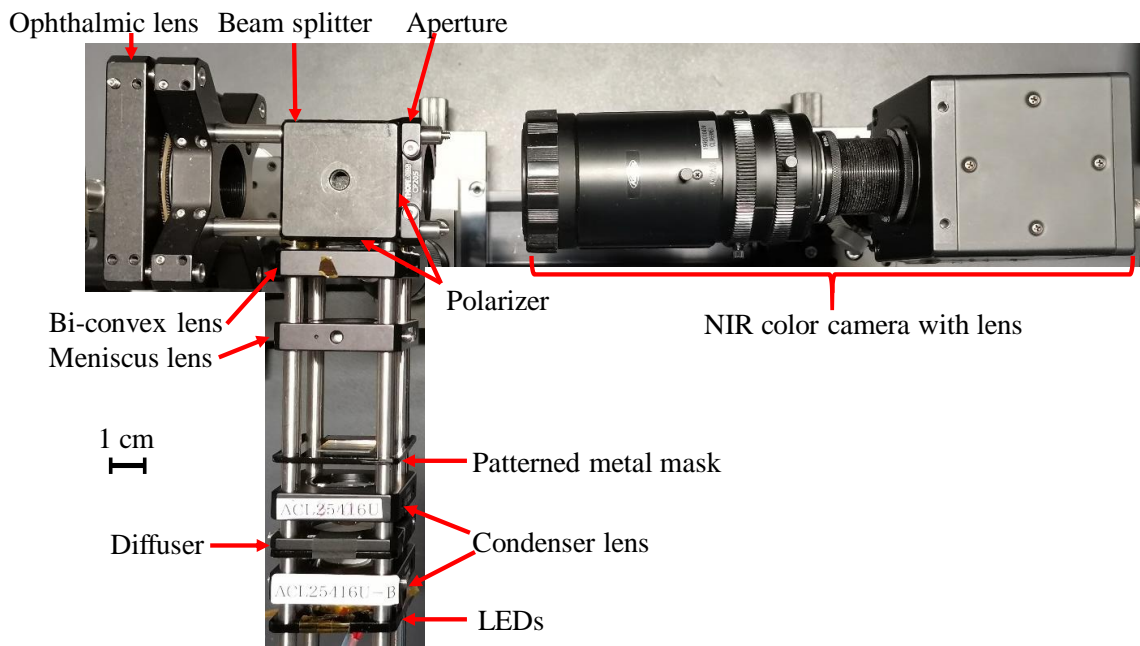


Fig. 3.12 Photograph of the fundus camera with a patterned metal mask for pattern projection.

3.5 Pattern Projection on the Retina with a Patterned Metal

Mask

The NIR fundus camera with a patterned metal mask was applied to both a glass eye model and a human eyeball, as they both have a similar optical length and pattern on the fundus. The first step in fundus patterned imaging acquisition of the human requires the patient eyeball should look toward the pattern formed by the eyeball fixation target so that the linear stripe patterned beam will illuminate around the optic disc area. The pattern illuminated fundus images are then captured by the camera and accumulated to decrease the random noise, creating the pattern as shown in Fig. 3.13(b). Figure 3.13(a) shows the linear stripe pattern in the glass eye model captured by the NIR fundus camera with a patterned metal mask. Subsequently, the NIR fundus camera with a patterned metal mask was applied to the human eyeball creating the fundus image shown in Fig. 3.13(b). The linear stripe pattern and optic disc can be clearly observed. These two images only show the linear stripe pattern, while the eyeball fixation target is out of the field of view. As there is fewer fundus vasculature near the fovea, we want to enlarge the optic disc area to image every detail of the fundus vasculature. However, the fovea area is unnecessary in the pattern illuminated fundus image; hence, Fig. 3.13(b) only shows the optic disc area with man vasculature. The eyeball fixation target will appear in Fig. 3.13(b) if the field of view is more comprehensive. The precise linear stripe pattern, optic disc, and fundus vasculature prove the feasibility of our proposed NIR fundus camera for observing the interior of an eye and the patterned fundus illumination for fundus scattering detection. However, the scattering information from an image like Fig. 3.13(b) is difficult to analyze because the scattered light may affect each other, resulting from the narrow pitch of the linear stripe pattern and low image resolution. Hence, the layout of the patterned mask needs optimization.

From the results, it was found that the linear stripe pattern should be changed to be sparse. In this case, if a metal mask is used, it won't be easy to see the underlying fundus pattern. However, if the interference filter mask proposed in this study is used, the entire area of the interference filter can transmit infrared light of 900 nm or more, so a NIR 3-channel sensor, which includes NIR1 (800 nm), NIR2 (870 nm), NIR3 (940 nm), can take a whole fundus image. Simultaneously, the pattern illumination for scattering measurement at 800 nm can be acquired on the NIR1 channel.

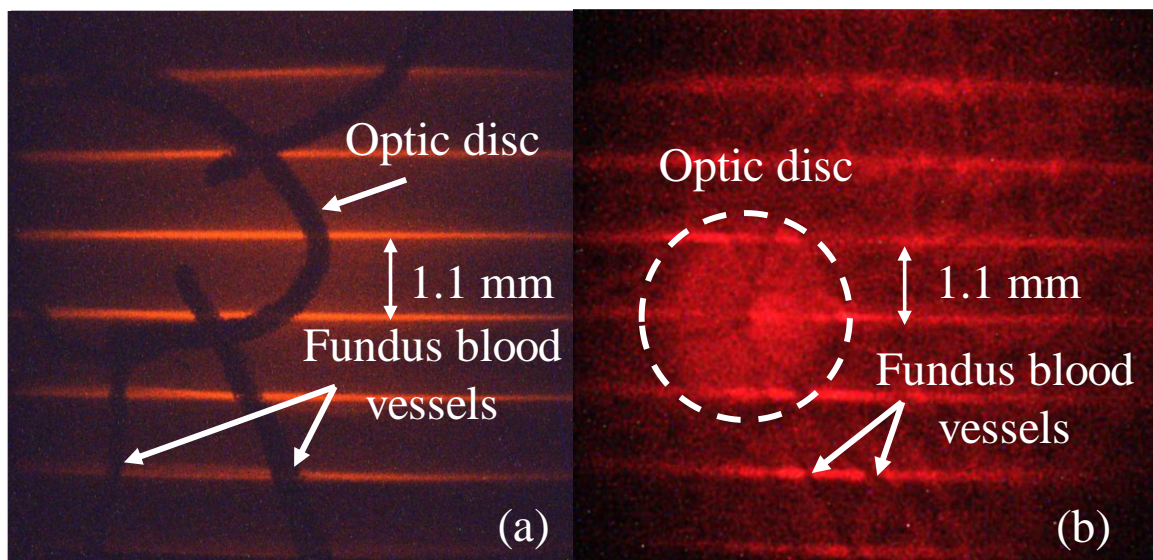


Fig. 3.13 Photographs of the linear stripe pattern projected on fundus in (a) the glass eye model and (b) human eyeball.

3.6 Scattering Experiments with a Patterned Metal Mask

Since the linear stripe patterned fundus images prove the feasibility of the fundus patterned illumination in the last section, the scattering experiments with linear stripe patterned illumination are presented in this section. The pitch of the linear stripe pattern in the metal mask is 1.1 mm; in case of the potential interaction between the scattered light generated by the

adjacent linear pattern, the patterned metal mask in this scattering experiment was covered by a 100% absorption mask. This combined mask absorbs all the illumination light except for the light illuminate on a specific linear stripe pattern in the metal mask. In this section, the patterned metal mask means the combined mask.

3.6.1 Preparation of the Artificial Blood

Human blood is a body fluid that delivers nutrients and oxygen to cells and transports metabolic waste products away from those same cells. The human blood is mainly composed of red blood cells, white blood cells, platelets, and plasma, in which plasma constitutes 55% of blood fluid and contains proteins, lipids, glucose, mineral ions, hormones, carbon dioxide, and so on. Blood lipid is mainly transported with protein, which is called lipoprotein, in blood plasma. The lipoprotein is a biochemical assembly whose primary function is to transport hydrophobic lipid molecules in blood plasma or other extracellular fluids. The lifestyle diseases, such as dyslipidemia, stroke, etc., are highly related to the lipoprotein concentration in human blood. Thus its measurement is crucial for disease prevention and diagnosis. In this research, we are mainly concerned with the optical parameters of the lipoprotein in human blood.

According to the light transport theory, the optical parameters are defined by the absorption coefficient (μ_a) in mm^{-1} and the reduced scattering coefficient (μ'_s) in mm^{-1} [57]. In which the μ_a describes the probability of a photon to be absorbed per unit length, The μ'_s is to describe the diffusion of particles in random space. The reduced scattering coefficient can be described as the following equation:

$$\mu'_s = \mu_s \times (1 - g) \quad (5)$$

where the μ_s is the scattering coefficient and g is the anisotropy parameter. The scattering

coefficient is a measure of the ability of particles to scatter photons out of a beam of light [58]. Furthermore, the scattering coefficient can also be defined as a description of a medium containing many scattering particles at a concentration [30]. The anisotropy parameter is the cosine function of the partial deflection angle.

The μ'_s of blood depends on a mismatch of averaged refractive indices of blood plasma and RBC cytoplasm [59]. It has been reported that mixtures of black ink and Intralipos (soybean oil emulsion) can be used as artificial blood to experiment with the optical property [60]–[65]. Since the lipoprotein is the main blood component of interest in this research, we applied black ink and Intralipos to emulate the optical parameters of human blood. Artificial blood is composed of black ink (PILOT INK-350-B) and Intralipos (OTSUKA Intralipos injection 20%) used to emulate human blood's absorption coefficient and scattering coefficient, respectively, to test the relationship between scattering propagation distance and the reduced scattering coefficient. It is to be noted that the results from the solution cannot directly be compared with those from human blood because of the presence of particles of various sizes and refractivity.

Though the black ink still has an albedo value, which means the low reduced scattering coefficient, when mixed the black ink with diluted diffusive medium, by measuring the extinction coefficient of the mixture, the calculated absorption coefficient of the black ink is approximately zero, which is negligible [66]–[70]. Similarly, the absorption coefficient of Intralipos also can be ignored compared to its scattering coefficient according to the previous study of the Intralipos optical properties [71], [72]. Thus, in this research, the black ink and Intralipos were applied to emulate the optical parameters of human blood without considering the reduced scattering coefficient and absorption coefficient from the black ink and Intralipos, respectively.

The concentration of black ink and Intralipos is related to the artificial blood's effective

scattering coefficient and absorption coefficient. The formula of Beer-Lambert law is shown as follows, which was applied to the measurement of the optical parameters of the black ink and Intralipos.

$$A = \log_{10} \frac{I_t}{I_0} = \log_{10} \frac{1}{T} = K \times l \times c \quad (6)$$

in which, A is the absorbance, I_0 and I_t are the intensity of incident light and transmitted light, respectively, T is transmission ratio, K is Molar attenuation coefficient, l is the thickness of absorption media, and c is the concentration of the absorption media. Thus, the relationship between the optical parameters and the concentration of black ink and Intralipos can be obtained according to the Beer-Lambert law [73]. Figure 3.14 shows the schematic diagram of the optical parameter measurement system of ink and Intralipos. The parallel incident light transmits the test solution and is detected by the detector, with the intensity of the incident light and transmitted light, and the thickness of the solution, the optical parameters of the solution can be calculated. The calculation of the optical properties as following equation (7).

$$\ln \frac{I_0}{I} = (\mu_a + \mu_s) \times L \quad (7)$$

where the I_0 is the intensity of the incident light, I is the intensity of the transmitted light, and L is the thickness of the test solution. Due to the scattering coefficient of ink and absorption coefficient of Intralipos are not in consideration, the optical parameters of the test solution are detectable. Following Equation (5), the reduced scattering coefficient can be calculated. The fitting curves of the reduced scattering coefficient and absorption coefficient according to Waseda university's experimental data are shown in Fig. 3.15 and 3.16. Though the fitted curve equation parameters are different from the previous research, the positive linear correlation between the coefficients and solution concentration satisfies the requirements of scattering experiments. The fitted curve equations are shown as follows:

$$\mu_a = 0.31 \times C_{ink} + 0.02 \quad (8)$$

$$\mu'_s = 0.19 \times C_{Int} + 0.08 \quad (9)$$

where the μ_a is the absorption coefficient, μ'_s is the reduced scattering coefficient, C_{ink} is the concentration of ink, and C_{Int} is the concentration of Intralipos. Their coefficients of determination are 0.995 and 0.997, respectively.

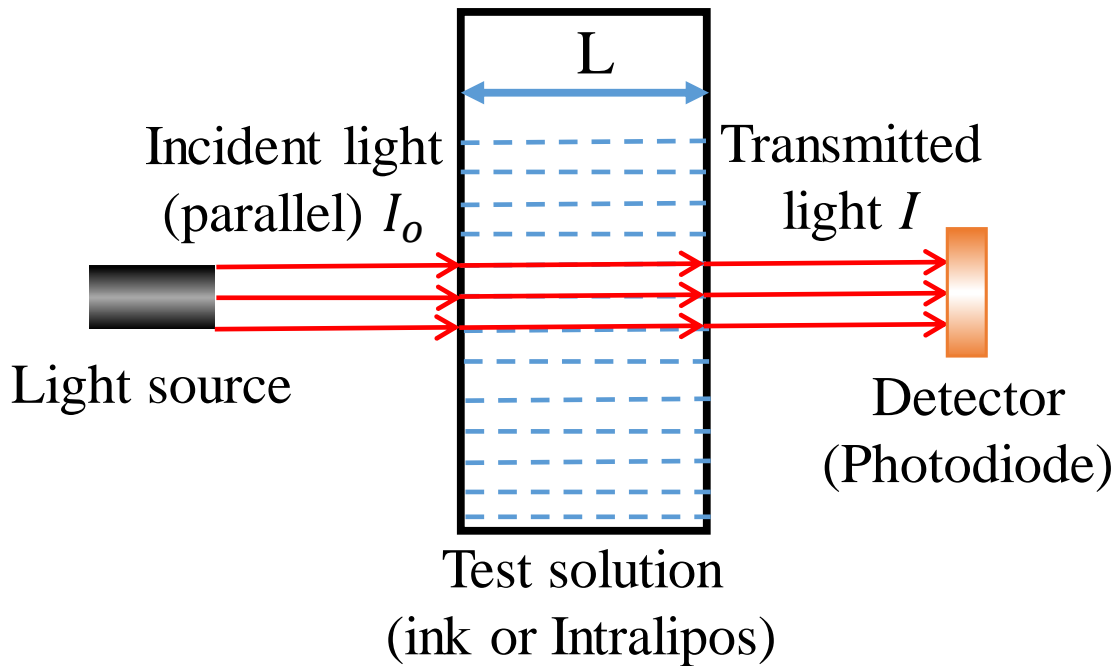


Fig. 3.14 Schematic diagram of the measurement system of optical parameters.

The artificial blood was prepared with the reduced scattering coefficient from 1.03 to 7.68 mm^{-1} by changing only the proportion of Intralipos in the mixture to test the maximum scattering propagation distance. Table 3.1 shows the concentration details of the artificial blood in this experiment. Though the reduced scattering coefficient in this experiment is higher than in human blood, this scattering experiment is to verify the feasibility of the fundus camera with a projection mask in lipid concentration detection.

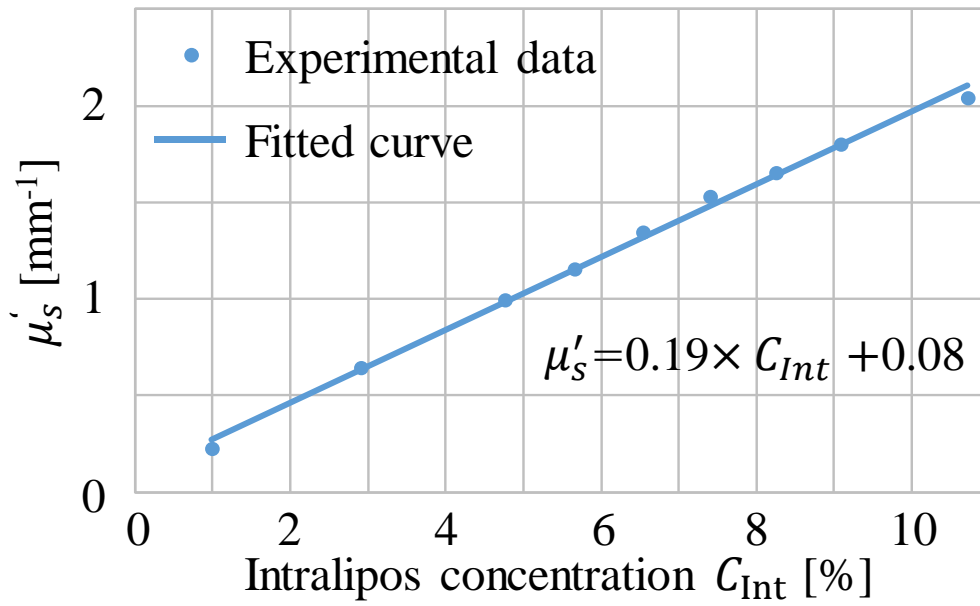


Fig. 3.15 The fitting curve of the relationship between the Intralipos concentration and reduced scattering coefficient.

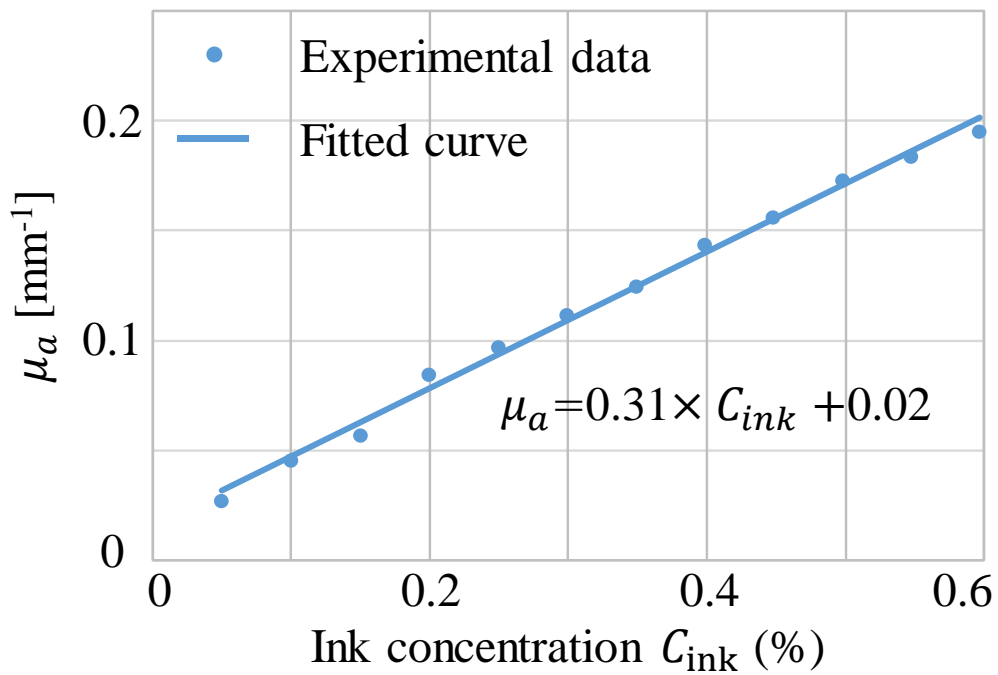


Fig. 3.16 The fitting curve of the relationship between ink concentration and absorption coefficient.

Table 3.1 The components concentration and reduced scattering coefficient of the artificial blood.

Intralipos concentration (vol%)	5%	10%	20%	30%	40%
Ink concentration (vol%)	1.6%	1.6%	1.6%	1.6%	1.6%
Reduced scattering coefficient (mm^{-1})	1.03	1.98	3.88	5.78	7.68

3.6.2 Scattering Experiment System

The fundus vasculature is the target of linear stripe patterned illumination. An experiment system for scattering detection was proposed to test the feasibility of the patterned metal mask in scattering detection. The system mainly includes three parts: a fundus camera with a patterned metal mask for linear stripe patterned illumination, an eye model with artificial blood for scattering generation, and a monitor (Blackmagic video assist 4K) for observation. Figure 3.17 shows the schematic of the scattering detection system, and Fig. 3.18 shows photograph of the assembled fundus camera with a patterned metal mask and an eye model for scattering detection.

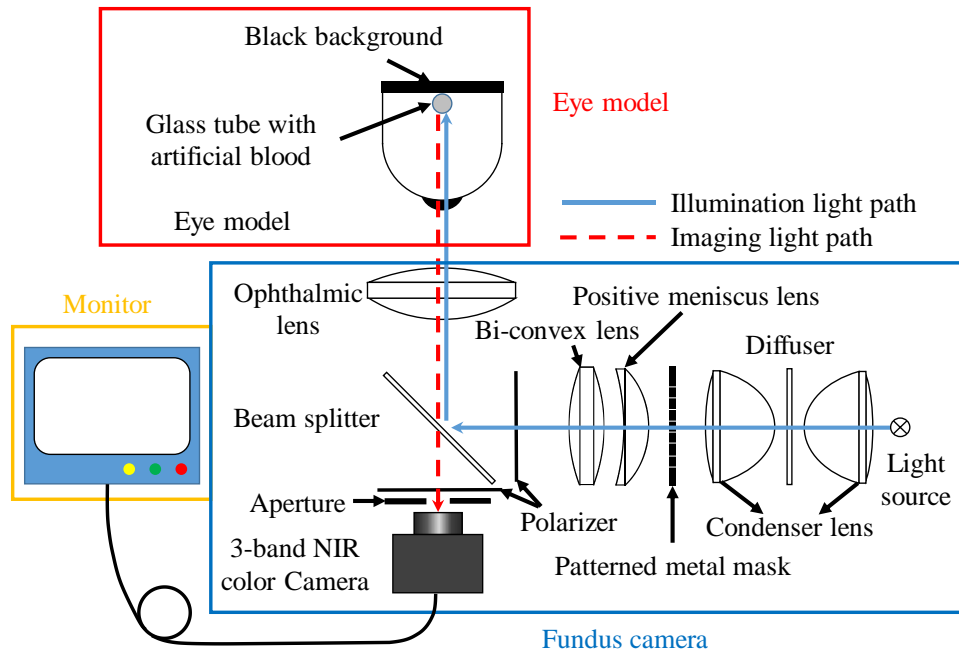


Fig. 3.17 Schematic diagram of the scattering detection system. Part A is the fundus camera with a patterned metal mask, part B is the eye model with artificial blood, and part C is the monitor.

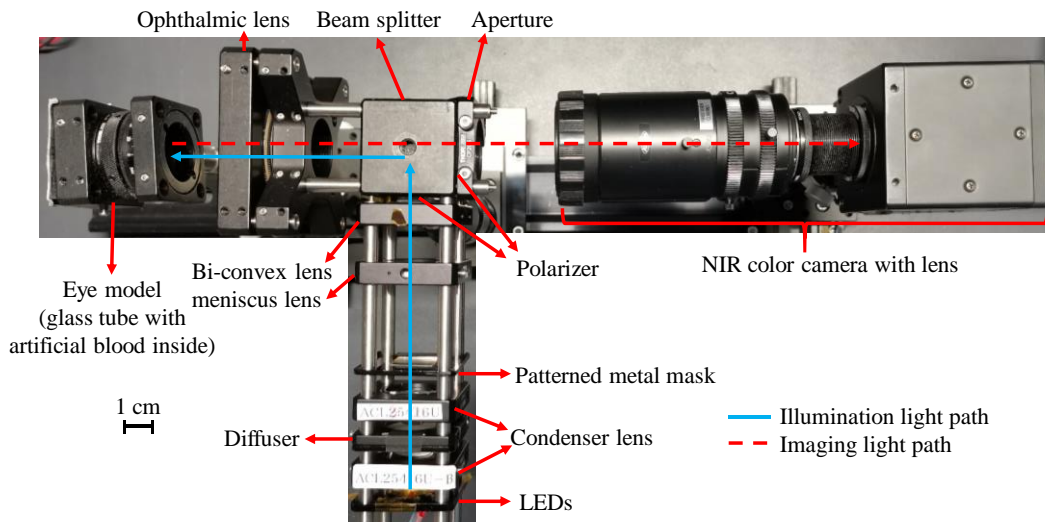


Fig. 3.18 Photograph of the assembled fundus camera with a patterned metal mask and an eye model for scattering detection.

According to the research of fundus vasculature, the mean diameter of fundus artery ranges from $135.73 \pm 15.64 \mu\text{m}$ to $123.01 \pm 13.43 \mu\text{m}$ and of vein ranges from $151.32 \pm 15.22 \mu\text{m}$ to $137.69 \pm 13.84 \mu\text{m}$ [74]. Thus, a glass tube with an inner diameter of $210 \mu\text{m}$ and an outer diameter of $700 \mu\text{m}$ was applied to emulate the fundus vasculature. The photograph of the glass tube is shown in Fig. 3.19. The background behind the glass tube is the black background. The eye model is rotatable to ensure the linear stripe patterned illumination light is perpendicular to the glass tube in the illumination plane.

Figure 3.20 demonstrates the schematic diagram of the scattering measurement. The linear stripe patterned illumination position will be set as the start point for scattering measurement. The direction of measurement was along with the glass tube, and the scattering intensity and the scattering position were calculated according to the pixel value and number. The photograph of the linear stripe patterned light on a glass tube filled with artificial blood is shown in Fig. 3.21. The measured data of different lipid concentrations will be applied to fit a relationship curve of scattering intensity and distance for the mixture with different reduced scattering coefficients.

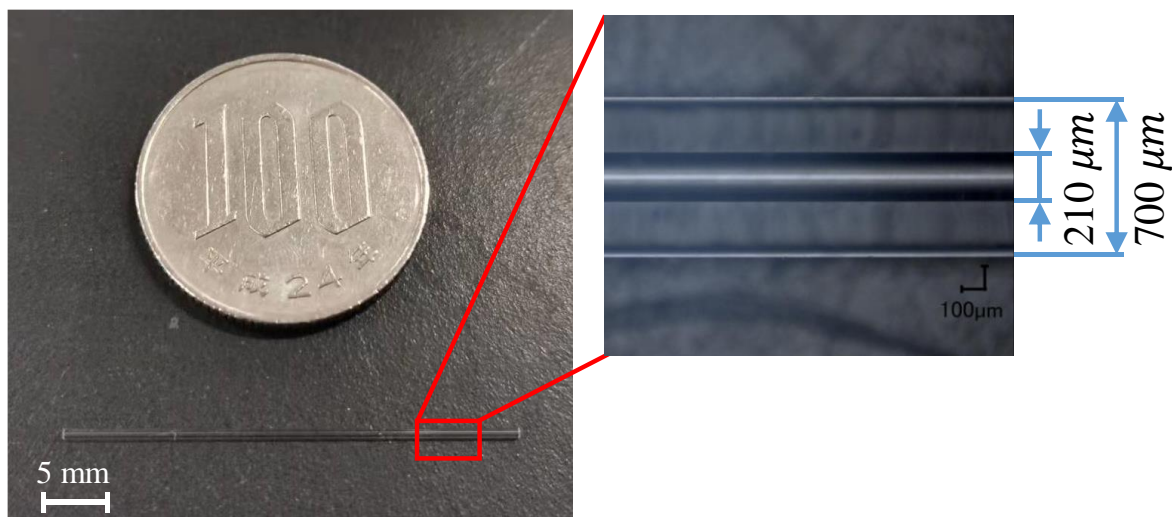


Fig. 3.19 Photograph of the glass tube (capillary) in the scattering experiment.

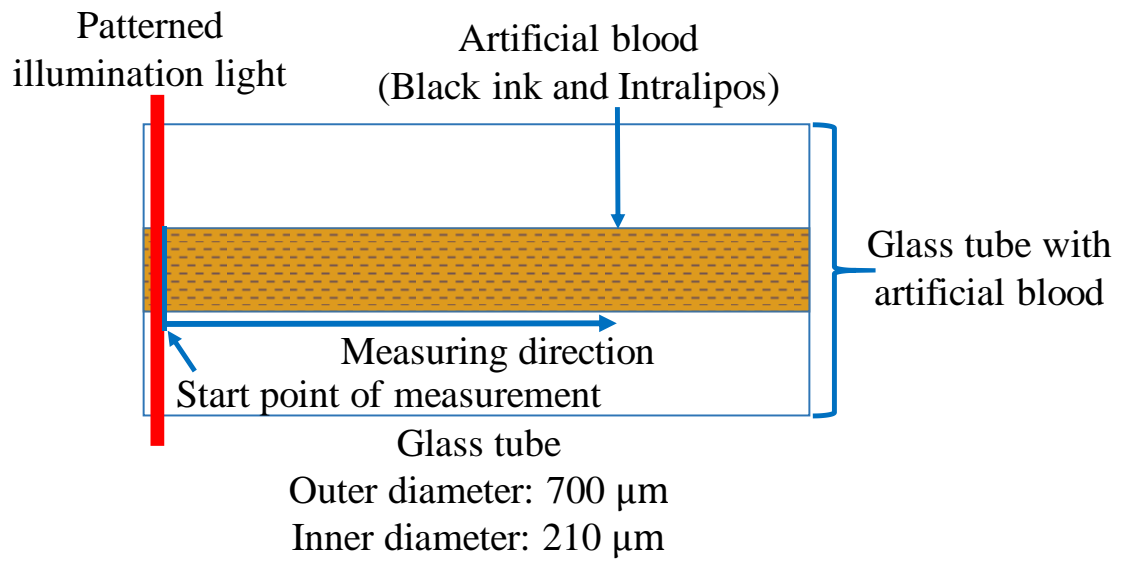


Fig. 3.20 Schematic diagram of scattering measurement by a glass tube with artificial blood.

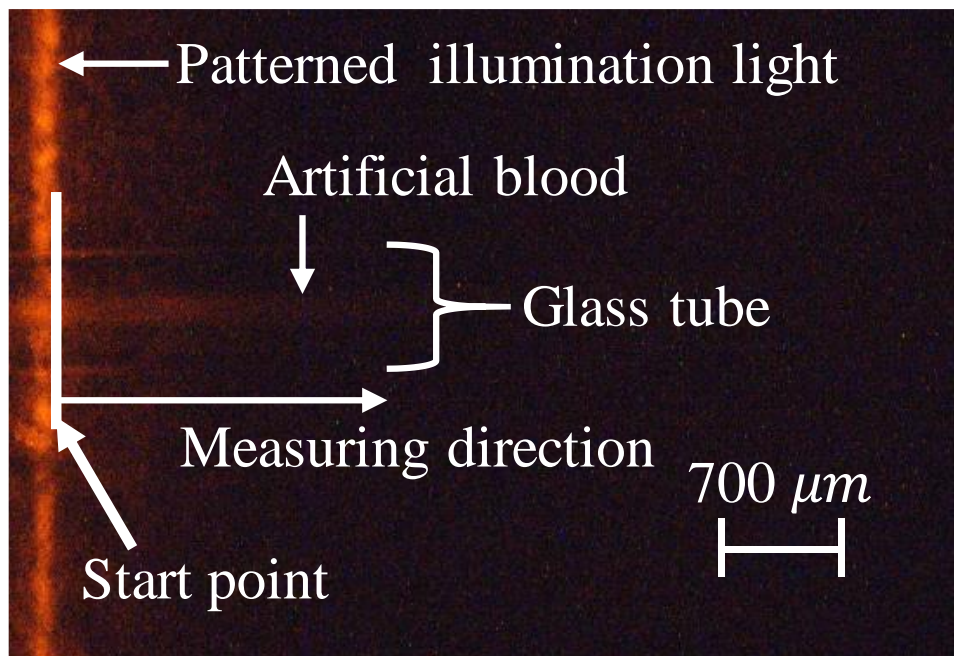


Fig. 3.21 Photograph of the linear stripe patterned light on a glass tube filled by artificial blood for scattering measurement.

3.6.3 Scattering Results Analysis

The artificial blood mainly includes particles of Intralipos and ink, in which ink and Intralipos are assumed to be without scattering coefficient and absorption coefficient, respectively. The artificial blood is well blended to eliminate the variable reduced scattering coefficient due to the Intralipos accumulation. The propagation diagram of scattered photons inside the artificial blood is shown in Fig. 3.22. The distance from light out to light in was called scattering distance here. The main component of Intralipos is soybean oil, whose particle size ranges from 4.8 microns to 1.7 microns [75]. The Lipoprotein inside the blood is classified into five types according to their sizes and compositions. They are chylomicron (diameter 75-1200 nm), very-low-density lipoprotein (30-80 nm), intermediate-density lipoprotein (25-30 nm), low density lipoprotein (18-25 nm), and high-density lipoprotein (50-120 nm) [76]. Thus, soybean oil can be used for emulating the chylomicron. The wavelength of illumination light for scattering detection was selected as 800 nm. The elastic scattering will be generated in the artificial blood with the linear stripe patterned illumination. The type of the elastic scattering can be separated according to the particle size and incident light wavelength, which is shown as follows:

$$a = \frac{2\pi r}{\lambda} \quad (10)$$

where a is the size parameter, r is the particle's radius, and λ is the wavelength of the incident light [77]. The calculated size parameter is used to distinguish the scattering type, in which Mie scattering has a size parameter ranging from 0.1 to 100. [78] Attributed to the similar illumination light wavelength and particle size, the size parameter will range from about 13 to 37. Thus the scattering-type in the artificial blood with 800 nm illumination should be Mie scattering. The schematic of the single Mie scattering is shown in Fig. 3.23 according to the Mie scattering theory [79], [80]. From the schematic diagram, the characteristic of Mie

scattering is the forward scattering intensity is stronger than other directions can be observed. However, multiple scattering happens in the artificial blood due to linear patterned illumination will change the scattering propagation distance and intensity (scattering relationship) according to the number of scattering events, that is, the lipid concentration in the artificial blood. Multiple scattering is more deterministic than single scattering; due to the multiple scattering combines average results from many single scattering events, the direction and intensity of the scattered light is predictable. Thus, multiple scattering can be measured for lipid concentration detection in artificial blood.

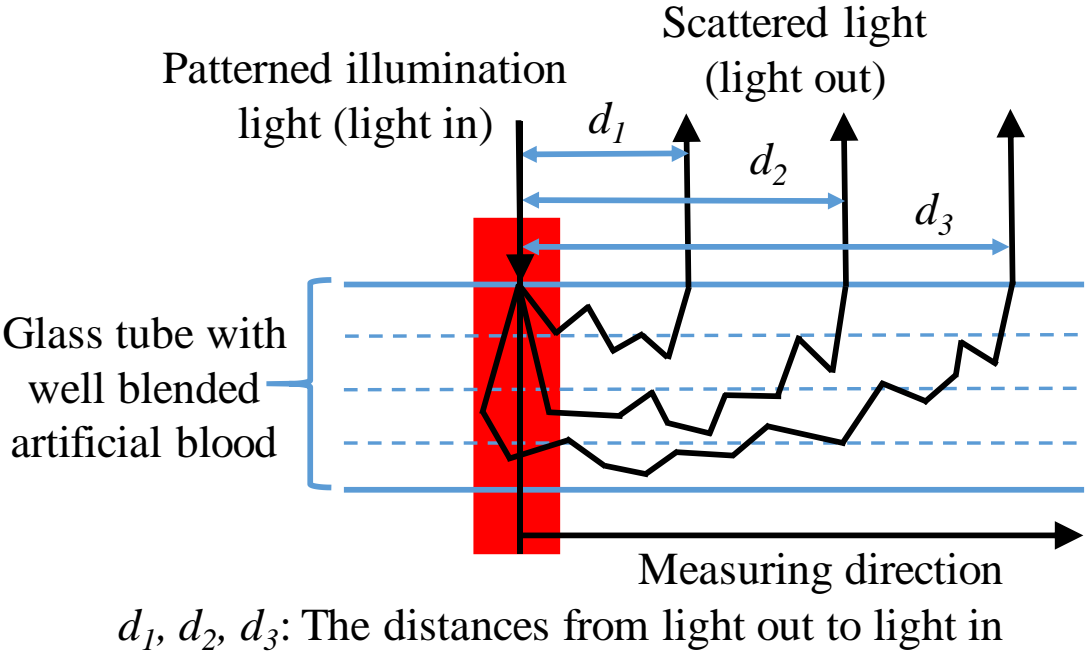


Fig. 3.22 The propagation diagram of scattered photons in well blended artificial blood.

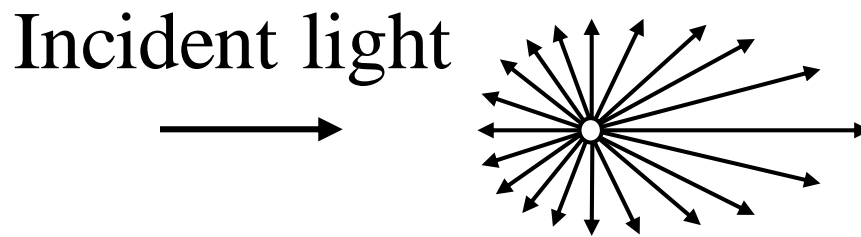


Fig. 3.23 Schematic diagram of the single Mie scattering.

The artificial blood with different lipid concentrations was applied to the lipid scattering experiment. Since the high intensity of the patterned illumination light may affect the measurement of the scattering intensity, the patterned illumination light area on an empty glass tube was set as the background for subtraction to remove the influence of the excessively high illumination light in the scattering experiment. Furthermore, images accumulation was applied to decrease the noise level. The accumulation number in this scattering experiment was set as 100. The measured normalized pixel values (scattering intensity) and the related distance from the start point (scattering distance) for the artificial blood with different reduced scattering coefficients are shown in Fig. 3.24. This figure shows that the scattering intensity is different under the same scattering distance for the artificial blood with different reduced scattering coefficients. The scattering intensity when the scattering distance is 0.345 mm (the distance of 100 pixels from the start point) was selected for scattering information analysis. The 100 pixels scattering distance is to reduce the influence of the illumination light on the scattering light while detecting the scattering information of the solutions with different lipid concentrations. Though the differences between the scattering relationship of different artificial blood can only be easily distinguished at a short scattering distance (D), the feasibility of reduced scattering coefficient (lipid concentration) measurement with the detected scattering information by the NIR fundus camera with a patterned metal mask was proved.

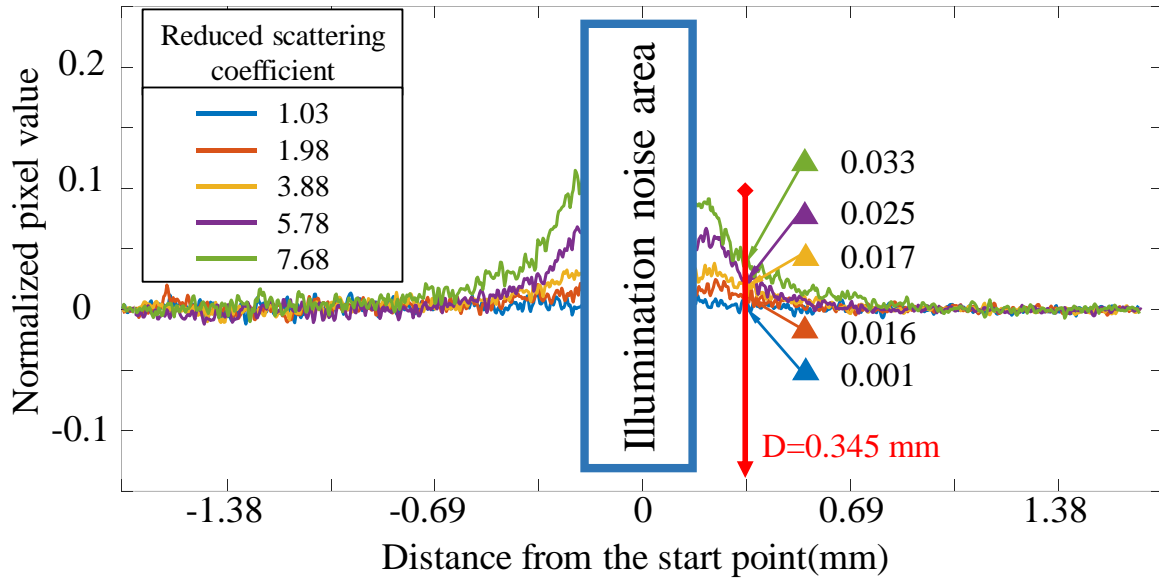


Fig. 3.24 Normalized pixel values for different scattering lengths of the artificial blood with different reduced scattering coefficients.

3.7 Summary and Discussion

In this chapter, a NIR fundus camera with a patterned metal mask for pattern projection on the fundus was presented. The numerical optical simulation of the NIR fundus camera with a patterned metal mask was presented firstly. Compared with the simulation results of the fundus camera, a linear stripe patterned illumination system, which includes a projection mask, a bi-convex lens, and a meniscus lens, was added. The image of the linear stripe pattern on the detector is precise with high uniformity. Furthermore, the layout of the projection mask was designed for a preliminary experiment. The projection mask layouts include the linear stripe pattern, eyeball fixation target, and fundus illumination area. These three areas are designed according to the human fundus structure to ensure the linear stripe patterned fundus illumination and eyeball fixation can be done simultaneously. Then the fundus camera was assembled for pattern projection and scattering detection. The fundus image taken by this fundus camera

shows a clear optic disc, fundus vasculature, and linear stripe pattern, which proves the feasibility of pattern projection on the fundus. Finally, the assembled fundus camera was applied to the scattering detection of artificial blood. A group of artificial blood with different reduced scattering coefficients was prepared to emulate the scattering properties of human blood. The scattering experiment results show a high correlation between the scattering information and the reduced scattering coefficient in artificial blood, which proves the feasibility of lipid concentration detection by the NIR fundus camera with a patterned metal mask.

4. A Multi-Functional Interference Filter for Patterned Fundus Illumination

4.1 Overview

The feasibility of the lipid concentration detection by measuring the scattering information has been proved by the fundus camera with a patterned metal mask, so a patterned interference filter (multi-functional interference filter) with three active areas will be designed for the scattering experiment. The problems found during the pattern projection on the fundus and scattering detection show that the layout of the projection mask needs to be optimized to avoid the interaction of the adjacent illumination light and fix the eyeball easier. Following the evaluated scattering distance, two optimized linear stripe patterns and a new eyeball fixation target comprised a matrix including number, alphabet, and circles are proposed. Furthermore, the transmission spectrum of each area in the multi-functional interference filter is simulated by adjusting the intermediate layer thickness of each area in the filter, the simulation result shows high transmittance at the wavelength band we are interested in. The fabrication of the multi-functional interference filter mainly includes sputtering deposition, photolithography, and etching process. The bottom nine layers of the multi-functional interference filter were deposited to form the intermediate layer (9th layer) with different thicknesses by photolithography and etching process. The details and parameters in the fabrication are presented. Finally, the transmission spectrum of the fabricated multi-functional interference filter was measured by reflection and transmission methods simultaneously. The transmission spectrum shows similar wavelengths of the transmittance peak as the simulation, which proves the fabricated multi-functional interference filter satisfies the requirements of the pattern projection. The outline diagram of this chapter is shown as Fig. 4.1.

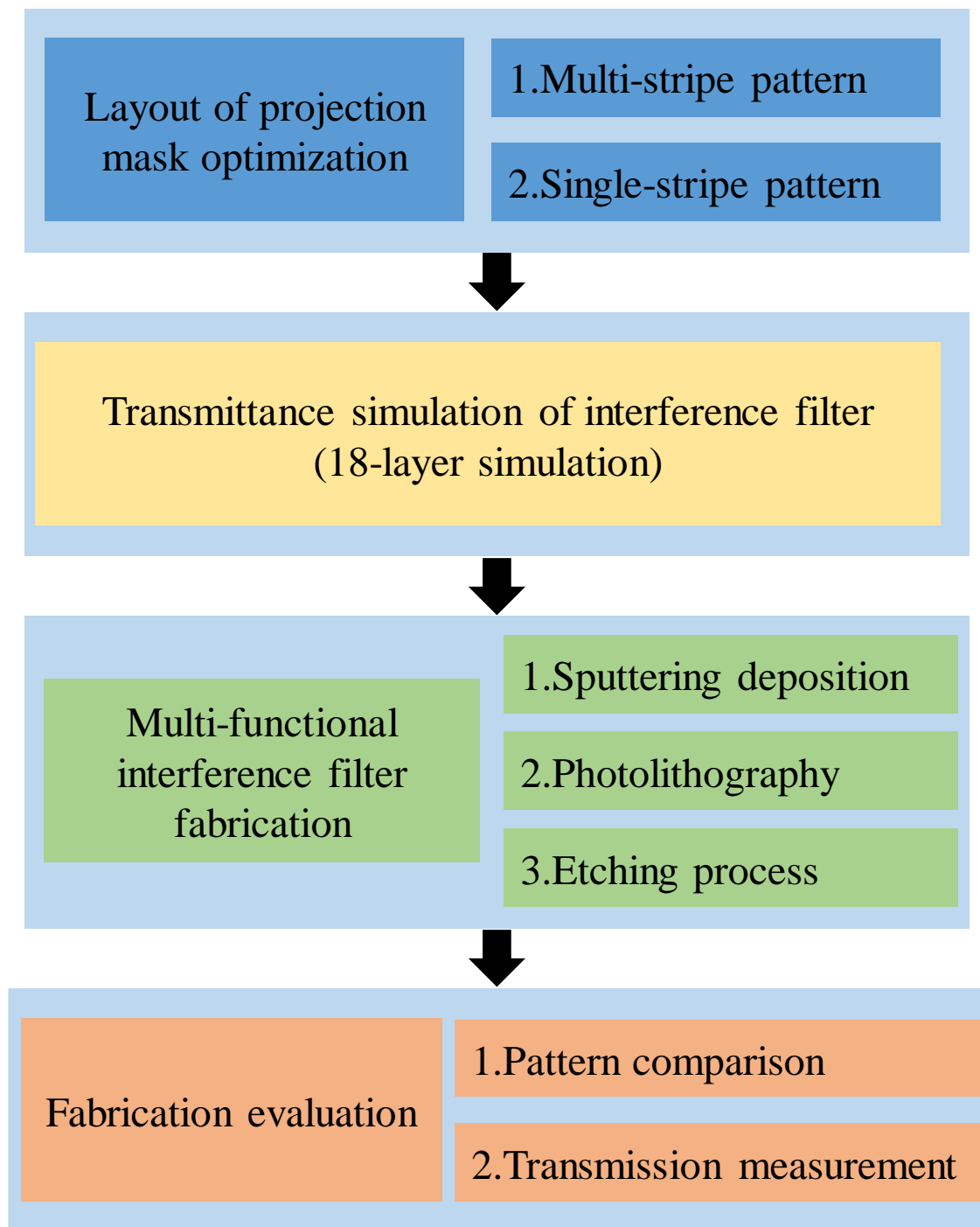


Fig. 4.1 Outline diagram of the contents in Chapter four.

4.2 Design of a Multi-Functional Interference Filter

4.2.1 Layout Optimization of Each Functionality in the Projection Mask

The projection mask has three areas: linear stripe pattern, eyeball fixation target, and fundus illumination area. Following the results from the fundus pattern projection and scattering detection by the metal mask, the layout needs to be optimized for higher performance. The optimization of the layout is only in linear stripe pattern and eyeball fixation target and will be presented individually. The optimization of the linear stripe pattern is to project the linear stripe pattern on the fundus and avoid the interaction of adjacent illumination simultaneously. The optimization of the eyeball fixation target is to fix the eyeball easier and fine-tune the gazing position of the patient eyeball for better pattern projection on the fundus. Due to the fabrication process of the multi-functional interference filter, the projection mask is composed of two layouts, the layout of the linear stripe pattern and the layout of the eyeball fixation target. The fabrication process of the multi-functional interference filter will be presented in the following sections.

The linear stripe pattern is to generate the linear stripe patterned illumination light for pattern projection on the fundus. The narrow pitch of linear stripe in the patterned fundus illumination may cause interaction between the scattering light from the adjacent linear pattern, so optimizing the pitch of linear stripe in the layout of the patterned projection mask is necessary. The relationship between the intensity and propagation distance of the fundus scattering is challenging to analyze with the interaction of adjacent linear patterns. To minimize the interaction between the scattered light generated by different linear illumination, we proposed two optimized linear stripe patterns.

One of our proposals is a multi-linear stripe pattern. To estimate the proper linear stripe pitch to avoid the interaction, the only parameter we are concerned with was the distance where the scattering disappeared, which was called scattering-disappear distance. Figure 4.2 shows the normalized pixel values (scattering intensity) for different scattering distances of the artificial blood with 7.68 mm^{-1} reduced scattering coefficient. In this figure, the scattering intensity drops rapidly from the start point to about 0.7 mm. In the middle part, from about 0.7 to about 1.5 mm, the descending speed becomes slower, but the descending trend is still easily observed. As for the remaining area, from about 1.5 mm to 2.1 mm, it is hard to observe any change in the scattering intensity, and all the scattering intensities are floating around 0. These statistics showed that the scattering-disappear distance of the artificial blood with 7.68 mm^{-1} reduced scattering coefficient is close to 1.5 mm. Figure 4.3(a) shows the layout of the multi-linear stripe pattern with 3.1 mm line pitch, which was estimated according to the data mentioned above. Furthermore, the distance from the third linear stripe to the up border was set as 9.5 mm, and the reason will be presented in our second proposal. Four parts were designed in the layout of the linear stripe pattern, the linear stripe pattern, a pattern marker, a filter marker,

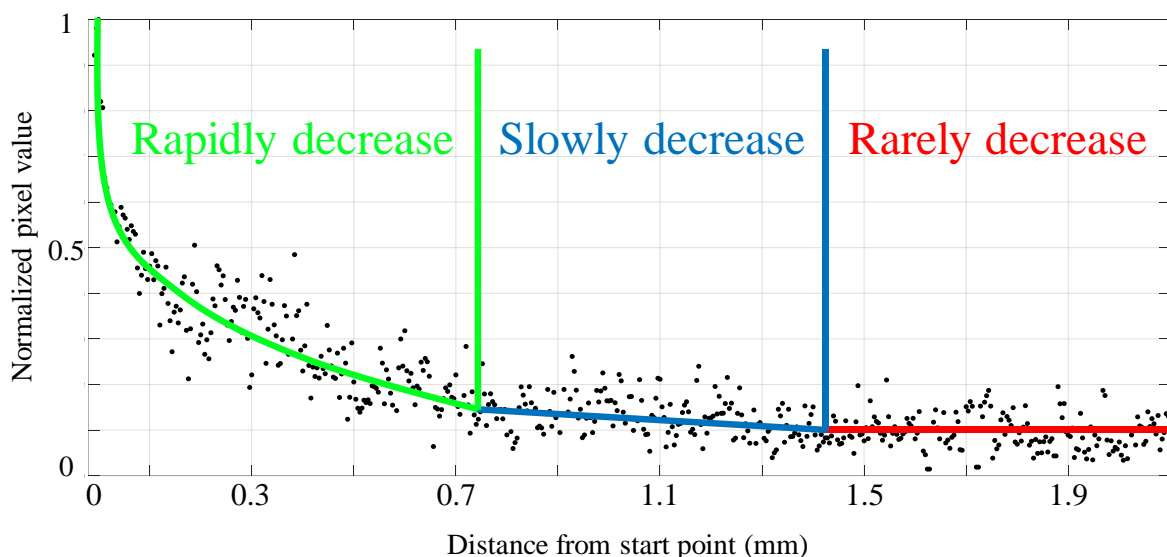


Fig. 4.2 Normalized pixel value dependence on the distance from start point measured for the sample with 7.68 mm^{-1} reduced scattering coefficient.

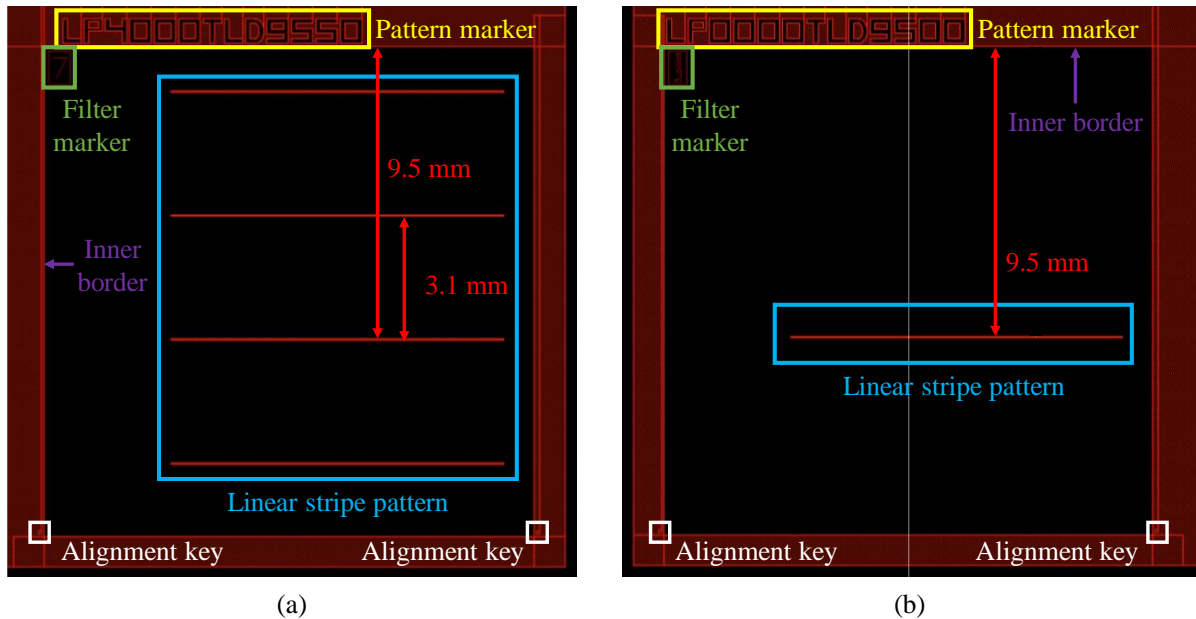


Fig. 4.3 The layouts of (a) the multi-linear stripe pattern with a 3.1 mm line pitch and (b) the single linear stripe pattern.

Another proposal is a single linear stripe pattern. To eliminate the interaction of adjacent linear patterns, we designed another layout of the projection mask with a single line. To transfer linear striped patterned light to illuminate the fundus vasculature and optic disc simultaneously when the human eye gazing on the eyeball fixation target, we estimated the position of the linear stripe by the fundus pattern projection. The linear stripe patterned light that can simultaneously illuminate the optic disc and fundus vasculature was recorded during the fundus observation by the patterned metal mask. The linear stripe that generates this light beam is what we need. This fundus observation was repeated five times to ensure the linear stripe position. The single linear stripe pattern layout is shown in Fig. 4.3(b). The distance between the linear stripe and mask upper inner border (border distance) was 9.5 mm. The mask inner border means the inner line of the red edge in Fig. 4.3. Chosen owing to its ability to cover the blood vessels, optic disc, and fundus tissue simultaneously, the single line in the layout was selected as the only linear stripe, the multi-linear stripe pattern also contains a line at the same position. In case of the

difference of patients, two more layouts of the single linear stripe with border distance 9.6 mm and 9.4 mm were designed. The single linear stripe pattern have the same usage as the multi-linear stripe pattern.

The eyeball fixation target is for easier eyeball fixation and optic disc area illumination. Though the eyeball fixation target already existed in the first version of the layout, we designed a new one to fine-tune the gazing position of the patient's eyeball easier. As shown in Fig. 4.4, the new eyeball fixation target comprises a matrix of circles, which also contains a crosshair consisting of alphabets and numbers. This design aims to enable the observer to accurately understand where the gazing position of the patient's eyeball is. With this design, the patient can be asked to change the gazing position on the eyeball fixation target for better optic disc illumination by the linear stripe light, for example, from position 2A to position 2B. With the adjustable gazing position, this eyeball fixation target can also decrease the affection from fundus differences from different patients. The final designed layout of the new eyeball fixation target and multi-linear stripe pattern is shown in Fig. 4.5.

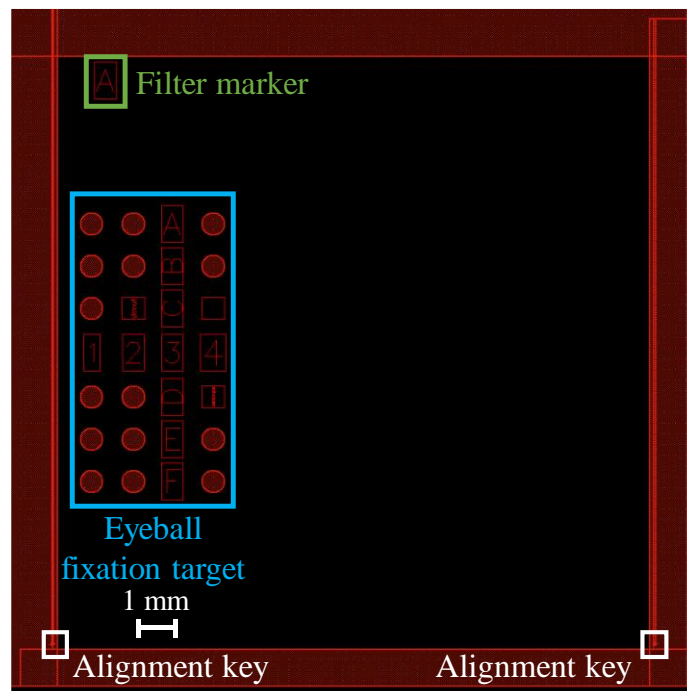


Fig. 4.4 Layout of the new eyeball fixation target.

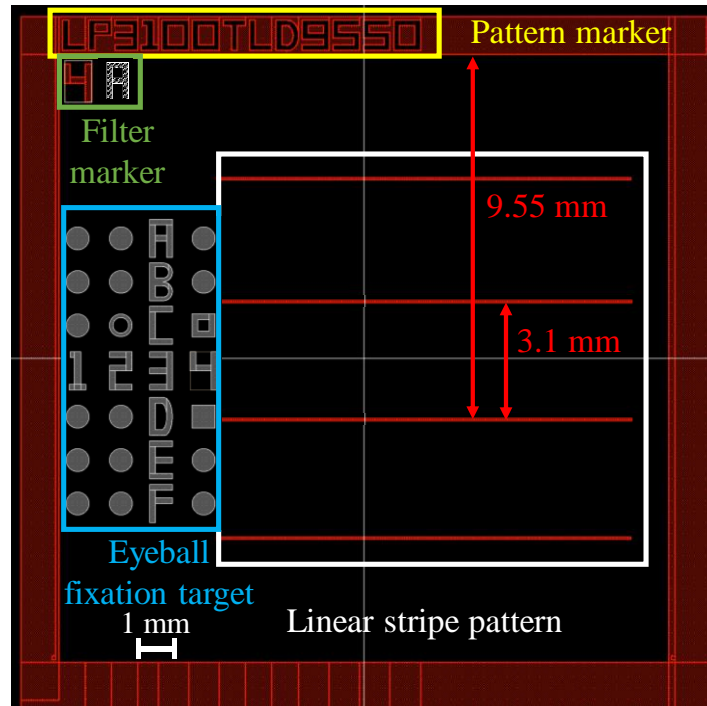


Fig. 4.5 Layout of the new eyeball fixation target and multi-linear stripe pattern.

4.2.2 Transmittance Simulation of Multi-Functional Interference Filter

The multi-functional interference filter included in the proposed fundus camera system was simulated to simultaneously transmit light of three wavelength bands in the different areas of the multi-functional interference filter. The linear stripe pattern with 800 nm wavelength was to transfer the illumination light from the light source to project the pattern on the fundus. The eyeball fixation target with 680 nm wavelength was to fix the gazing position of the eyeball for optic disc area illumination, and the fundus illumination area with NIR wavelength was to wide-area fundus illumination.

The transmission spectrum of the multi-functional interference filter simulated by our in-house thin-film simulator running on Mathematica. As shown in Fig. 4.6, there are 18 layers in the filter, and the 9th layer from the bottom is the intermediate layer. From the Fabry-Perot principle, we can control the transmittance of incident light at a specific wavelength, associated

with the refractive indices and the thicknesses of the materials used as thin films. Herein, we selected titanium dioxide (TiO₂) and silicon dioxide (SiO₂) as the high refractive index medium and the low refractive index medium, respectively. At the same time, the glass (BK7) is used as the substrate to simulate the multi-functional interference filter. The thickness of the high refractive index film (H) and the low refractive index film (L) can be represented as follows:

$$L = \frac{\lambda_0}{4n_L} \quad (11)$$

$$H = \frac{\lambda_0}{4n_H} \quad (12)$$

where λ_0 is the reference wavelength, L and H are the thickness of the film with different refractive index mediums, n_L and n_H are the low refractive index and the high refractive index, respectively. The thickness of the intermediate layer in the multi-functional interference filter determines the wavelength that can be transmitted. Thus, we can obtain an interference filter with high transmittance for a specific wavelength in the Mathematica simulation.

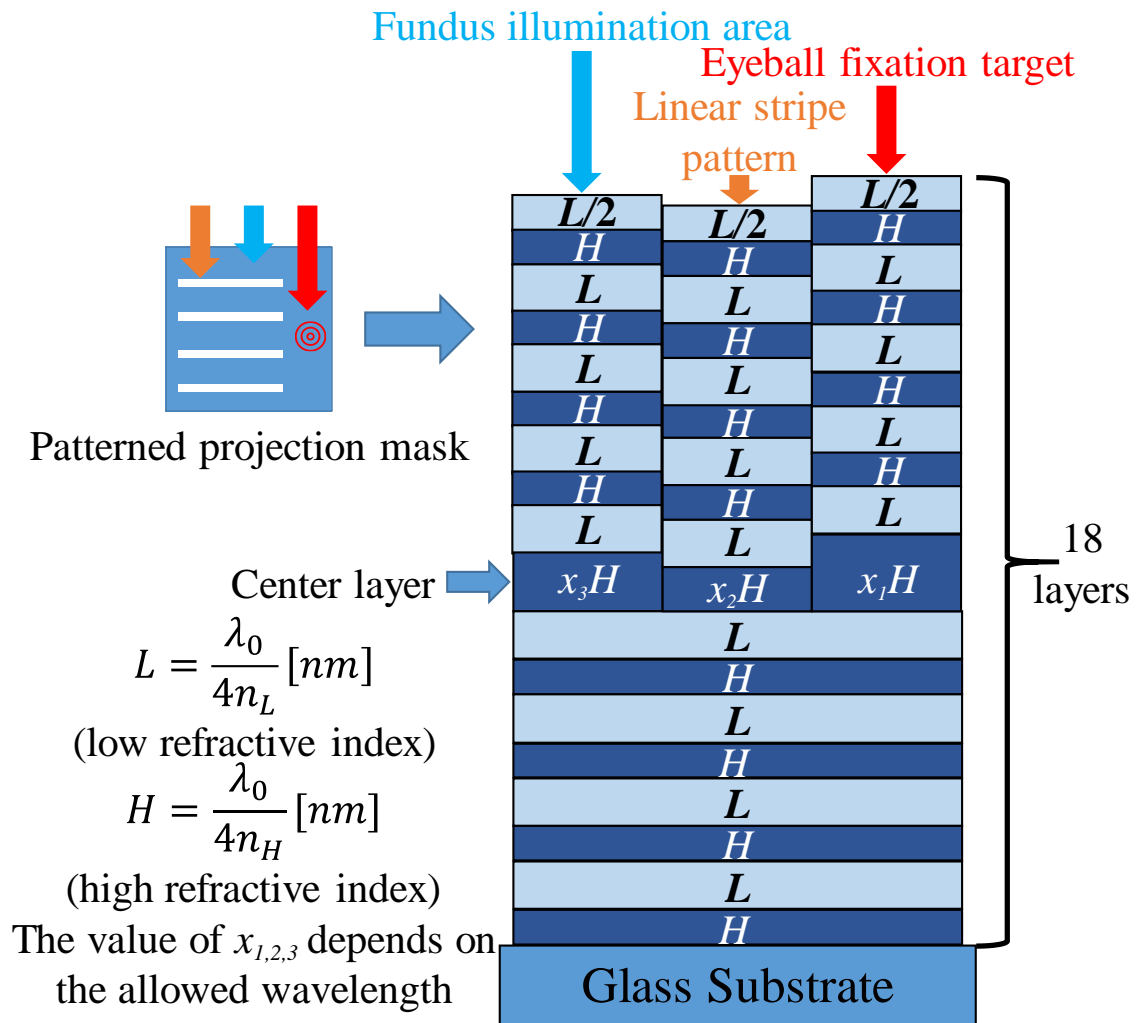


Fig. 4.6 Schematic structure of the multi-functional interference filter for pattern projection on the fundus.

As shown in Table 4.1, the default thicknesses of the high refractive film and the low refractive film are 76.4 nm and 126.4 nm, respectively. The thickness of the intermediate layer is different for the three areas in the multi-functional interference filter, 20.7 nm for the linear stripe pattern, 119.2 nm for the eyeball fixation target, and 76.4 nm for the fundus illumination area. Figure 4.7 shows the transmission spectrum of the multi-functional interference filter for different roles we got from the Mathematica simulation. The blue transmittance curve shows that the transmittance peak at 800 nm is more than 95%, and the half-bandwidth is less than 10 nm. The green transmittance curve shows that the transmittance peak around 680 nm is more

than 95%, and the half-bandwidth is less than 10 nm. The half-bandwidth of these two transmittance peaks is narrow enough to filter each other. All the transmittance curves show the high transmittance at the NIR band. Thus the transmission spectrum satisfies the requirements for pattern projection on the fundus.

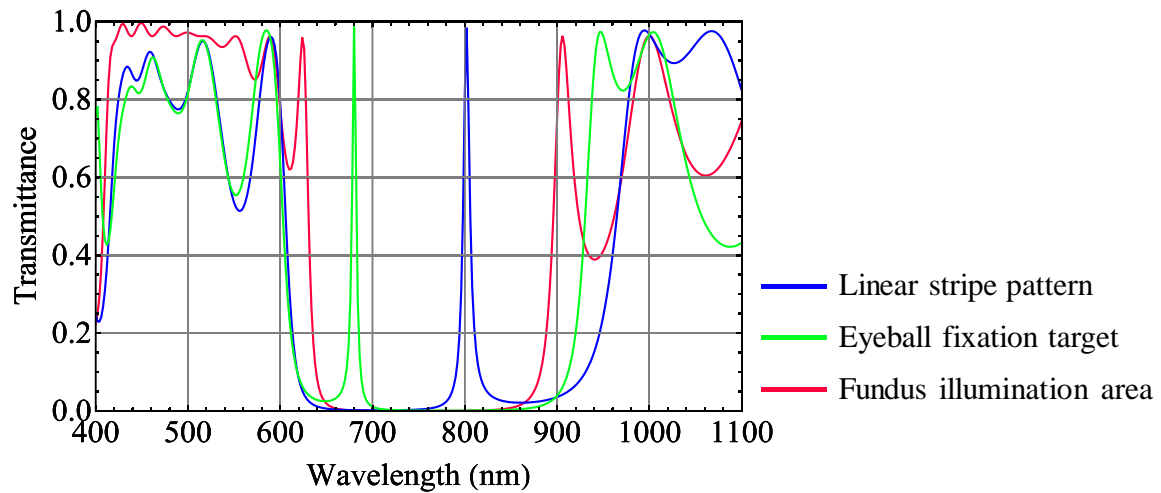


Fig. 4.7 Simulated transmission spectrum of the multi-functional interference filter with 18-layer film stack. The blue curve shows the transmission spectrum of the linear stripe pattern, with a narrow transmittance peak at 800 nm; the green curve shows the transmission spectrum of the eyeball fixation target, with a narrow transmittance peak around 680 nm; the red curve shows the transmission spectrum of the fundus illumination area. All these spectrum curves have high transmittance at the NIR band.

Table 4.1 The film thickness of the multi-functional interference filter in the simulation.


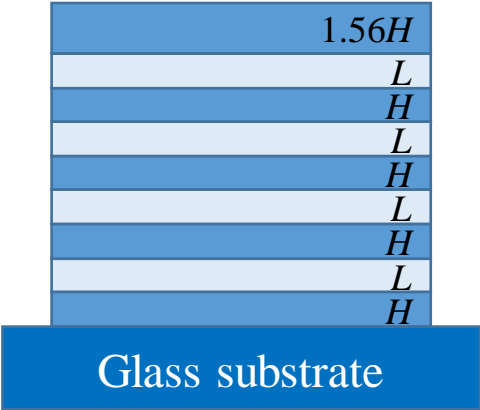
Media	Thickness
Silica (n_L)	126.4 nm
Titanium dioxide (n_H)	76.4 nm
Silica (first layer from the top)	63.2 nm
Titanium dioxide (the intermediate layer)	20.7 nm (for the linear stripe pattern) 119.2 nm (for the eyeball fixation target) 76.4 nm (for the fundus illumination area)

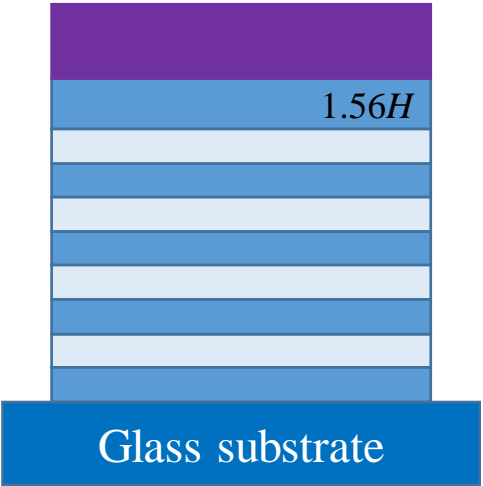
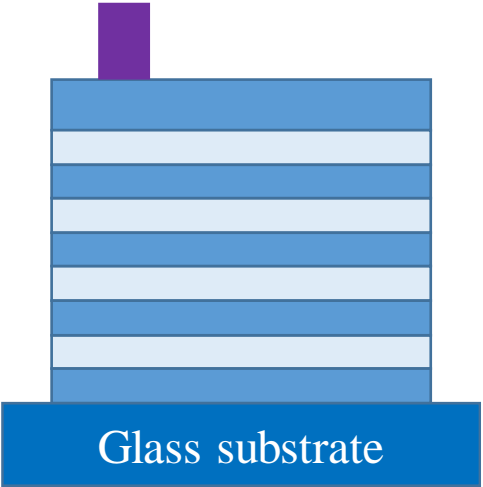
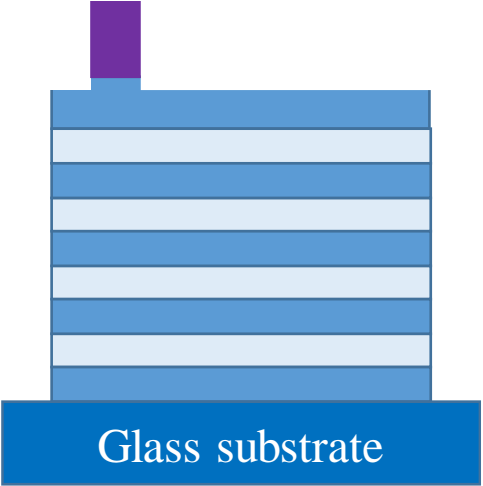
4.3 Fabrication of the Multi-Functional Interference Filter

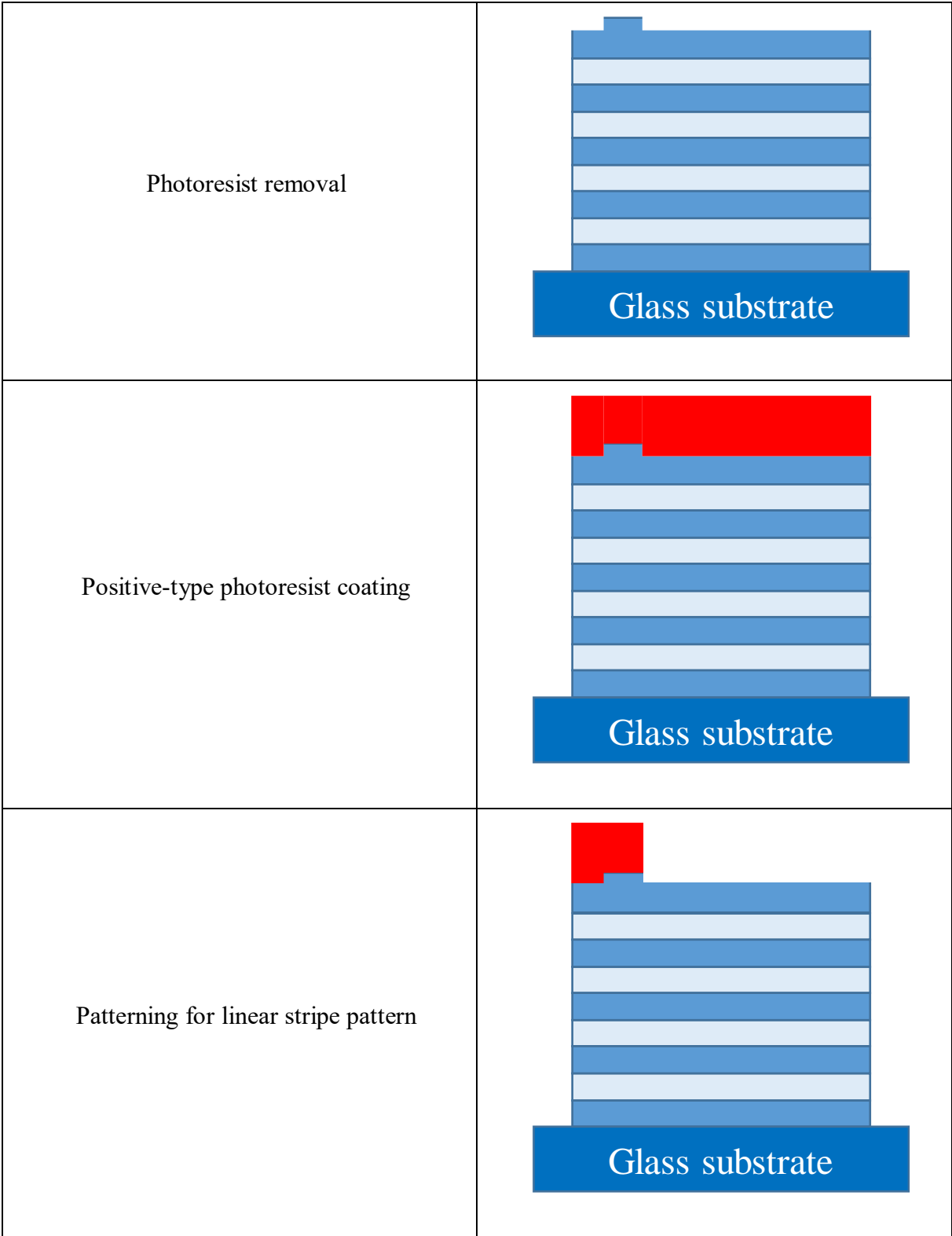
4.3.1 The Fabrication Flow Chart of the Multi-Functional Interference Filter

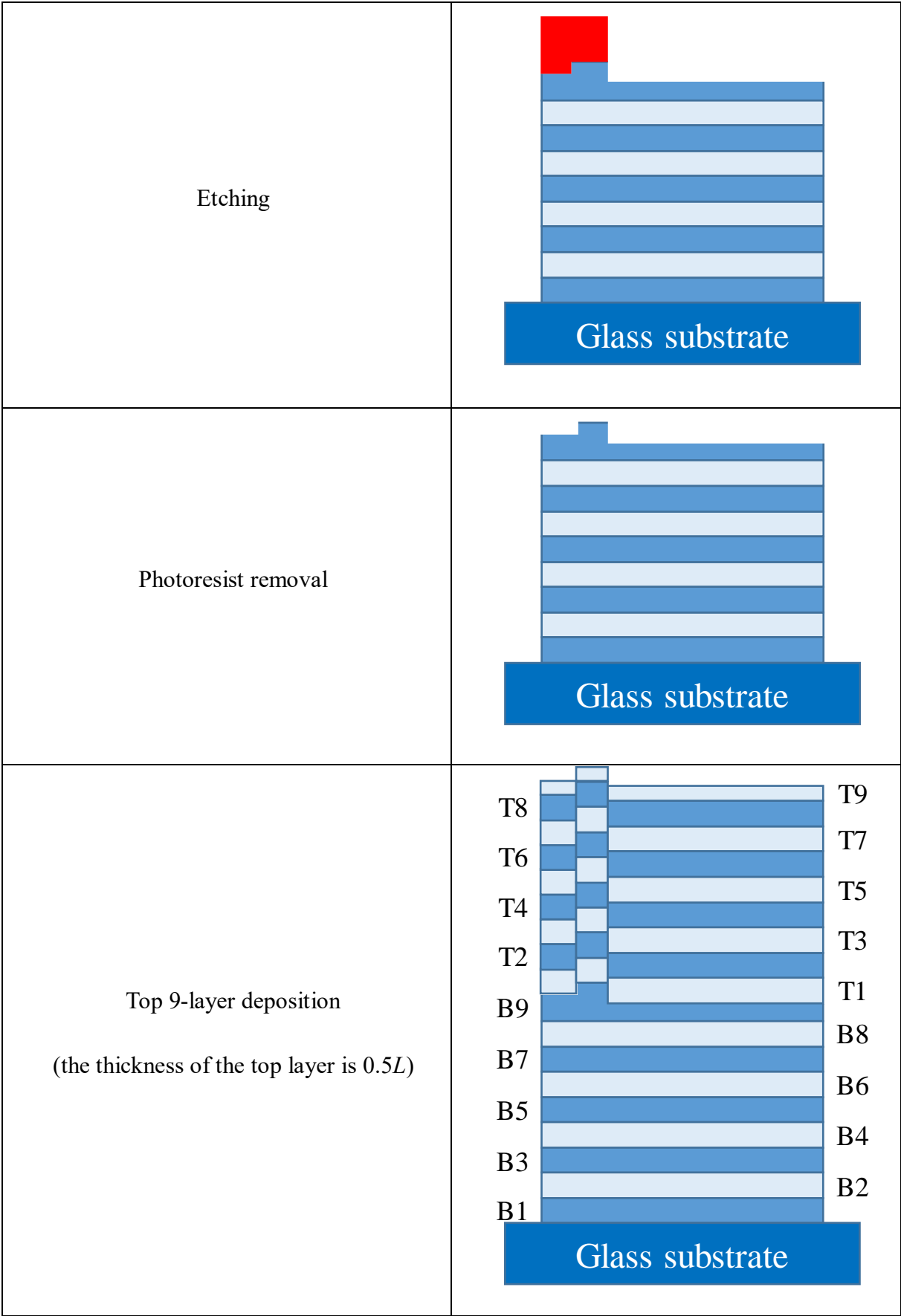
The fabrication procedure of the multi-functional interference filter mainly includes three steps, sputtering deposition, photolithography, and etching. Table 4.2 shows the schematic cross-section of the fabrication of the 18-layer multi-functional interference filter. In the schematic cross-section, the H means the thickness of the TiO_2 film, which is equal to 76.4 nm, the L means the thickness of the SiO_2 film, which is equal to 126.4 nm, all these thicknesses are calculated by the transmittance simulation. The layer number is demonstrated in the last.

Table 4.2 The schematic cross-section of the fabrication of the 18-layer multi-functional interference filter.

Process step	Schematic cross-section
Glass substrate preparation	
Bottom 9-layer deposition	

<p>Adhering film-type negative photoresist</p>	 <p>A cross-sectional diagram of a glass substrate. The substrate is a solid blue block at the bottom, labeled "Glass substrate". Above it is a stack of alternating horizontal layers: a dark blue layer, a light blue layer, a dark blue layer, a light blue layer, a dark blue layer, a light blue layer, a dark blue layer, a light blue layer, and a dark blue layer. On top of this stack is a thick purple layer labeled "1.56H".</p>
<p>Patterning for eyeball fixation target</p>	 <p>A cross-sectional diagram showing the patterning step. The purple photoresist layer from the previous step is now a thin, narrow vertical strip on top of the dark blue layer of the stack. The rest of the photoresist has been removed. The substrate is labeled "Glass substrate".</p>
<p>Etching</p>	 <p>A cross-sectional diagram showing the etching step. The thin purple strip remains on top of the dark blue layer. The light blue layers and the dark blue layers below them have been etched away, leaving a recessed area. The substrate is labeled "Glass substrate".</p>





4.3.2 The Process Conditions during the Fabrication

A sputtering deposition is a common process to fabricate titanium dioxide and silica films. TiO_2 and SiO_2 are alternately deposited by sputtering. Since the deposited film thickness is significantly related to the flow rate of argon and oxygen, chamber pressure, and deposition time, we have obtained an equation about the relationship between deposition time and film thickness while controlling the other parameters. The constant parameters during the sputtering deposition are shown in Table 4.3. Figure 4.8 shows the fitting curve of the relationship between the deposition time and deposition thickness of silica and titanium dioxide, respectively. The fitting curves about the deposition time and thickness of silica and titanium dioxide are shown in Equations 10 and 11, respectively.

$$T_{Si} = 12.96 \times t_{Si} \quad (13)$$

$$T_{Ti} = 1.99 \times t_{Ti} \quad (14)$$

where the t_{Si} is the deposition time of SiO_2 in a minute, t_{Ti} is the deposition time of TiO_2 in a minute, T_{Si} is the deposition thickness of SiO_2 in the nanometer, and T_{Ti} is the deposition thickness of TiO_2 in the nanometer. As shown in Table 4.2, the bottom 9-layer of the multi-functional interference filter will be deposited first, the first layer from the top of the 18-layer interference filter is defined as T1. Figure 4.9 shows the schematic structure of the bottom 9-layer film stack of the multi-functional interference filter. In this figure, the first layer from the bottom of this 9-layer film stack is defined as B1. Due to the eyeball fixation target has the highest film thickness of the intermediate layer (B9), this thickness is applied to deposit the intermediate layer (CFS-4ES-II, Shibaura, Japan). The deposition times shown in Table 4.4 are estimated following the fitting curve shown in Fig. 4.8. The film thickness fluctuation during the film deposition will affect the transmittance of the film stack, so the transmittance measurement of the deposited 9-layer film stack is important.

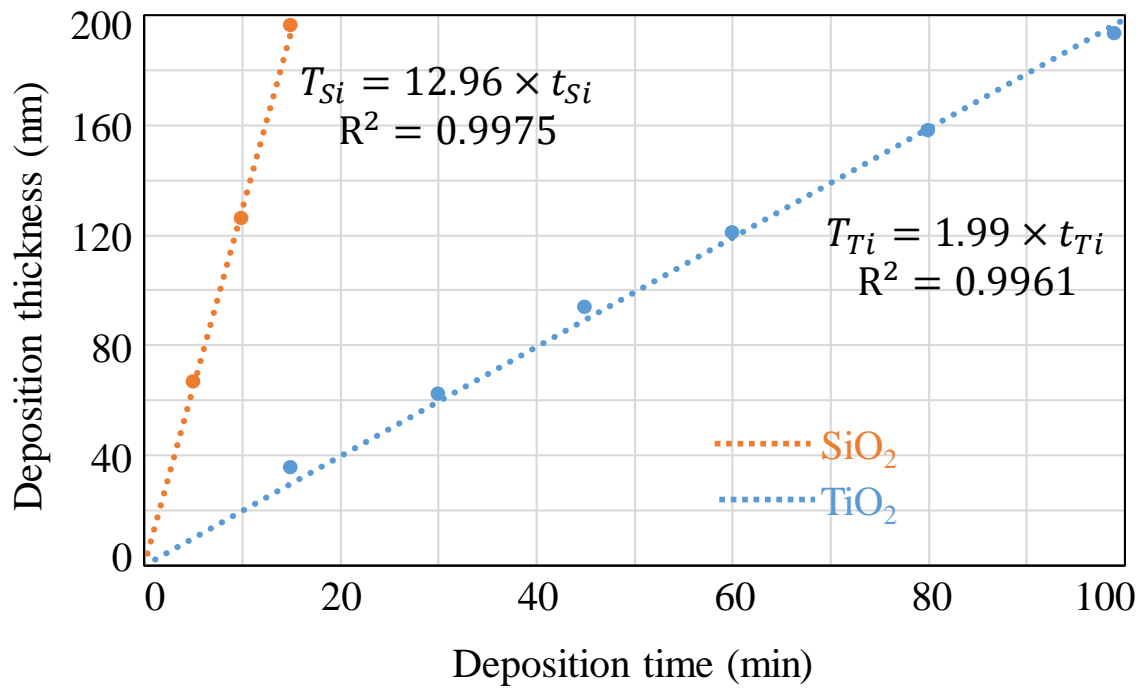


Fig. 4.8 The fitting curve of the relationship between the deposition time and deposition thickness.

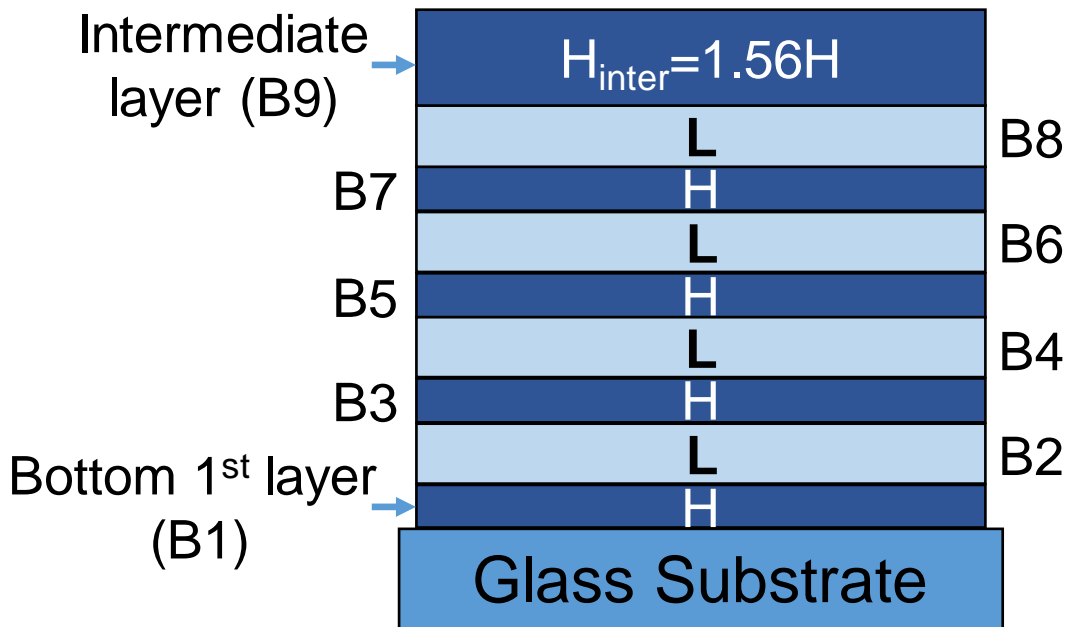


Fig. 4.9 Schematic structure of the bottom 9-layer film stack of the multi-functional interference filter. The first layer from the bottom of this 9-layer film stack is marked with B1.

Table 4.3 The constant parameters during the sputtering deposition.

The constant parameter		Value
Pressure inner chamber (Pa)		0.5
Gas flow rate (sccm)	Argon	19
	Oxygen	1
The rotational speed of the table (r/min)		24
RF powers (W)	SiO ₂	400
	TiO ₂	300

Table 4.4 Deposition time for different target materials.

Target material	Layer number	Film thickness in simulation	Deposition time
SiO ₂	B2, B4, B6, B8, T3, T5, T7, T9	126.4 nm (L)	9min45sec
TiO ₂	B1, B3, B5, B7, T2, T4, T6, T8	76.4 nm (H)	38min23sec
TiO ₂ (intermediate layer)	B9	119.2 nm	59min54sec
SiO ₂ (most top layer)	T1	63.2 nm	4min52sec

The photoresist coating follows the sputtering deposition process. Two cycles of photolithography and etching are required to obtain the thickness of the intermediate layer of the fundus illumination area and the linear stripe pattern. In the first cycle, a negative-type photoresist (n-PR; RY3315EE) was combined with the filter by a heat roller (L3570HI, Asmix) at 125°C. After the photoresist coating, the mask fabricated according to the layout of the eyeball fixation target (shown in Fig. 4.4) was applied to the exposure of the filter by a contact aligner (MA-10, Mikasa Co., Ltd., Japan) to remove the photoresist in all areas except the eyeball fixation target. Reactive ion etching (RIE) (RIE-10NIT, Samco Inc., Japan) was applied to etch the intermediate layer of the exposed filter. The etching thickness is significantly related to the gas flow rate and etching time. The constant parameters during the etching process are shown in Table 4.5. Figure 4.10 shows the fitting curve of the relationship between the etching time and thickness of the intermediate layer (TiO₂). The equation of the fitting curve is shown as Equation 12.

$$T_{etch} = 18.59 \times t_{etch} \quad (15)$$

where the t_{etch} is the etching time in a minute, and T_{etch} is the etching thickness in a nanometer.

Table 4.5 The constant parameters during the etching process.

The constant parameter		Value
Gas flow rate (sccm)	CHF3	20
	O ₂	5
Chamber pressure (Pa)		3
RF powers (W)		150

The etching times for different areas in the bottom 9-layer film stack is shown in Table 4.6. The microphotographs of the partial eyeball fixation target in the bottom 9-layer film stack after the first cycle of the photolithography and etching are shown in Fig. 4.11.

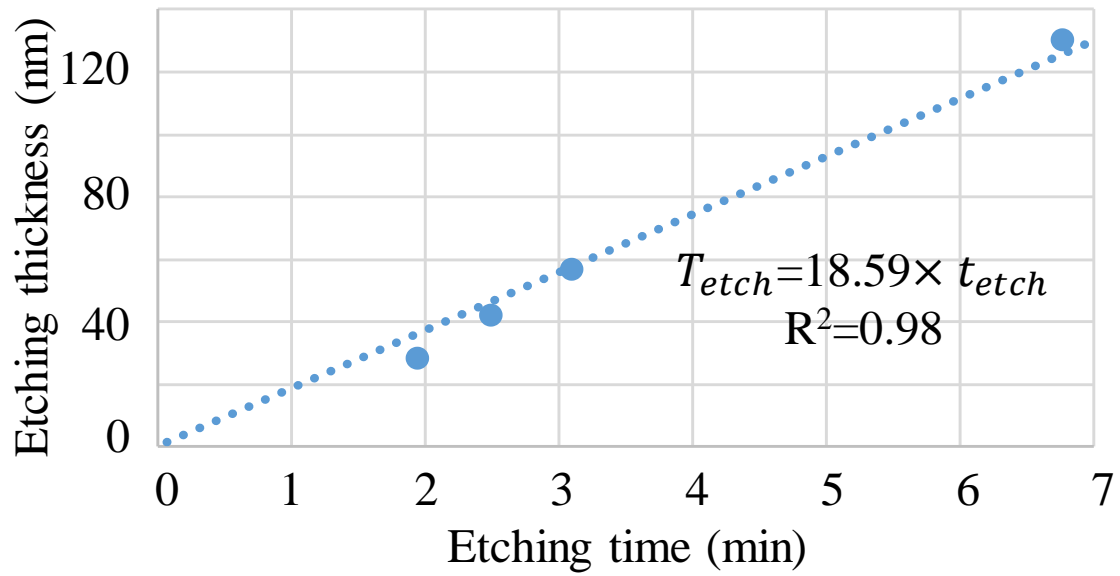


Fig. 4.10 The fitting curve of the relationship between the etching time and thickness of the intermediate layer (TiO₂).

Table 4.6 The etching times for different areas in the bottom 9-layer film stack.

Etching area	Etching thickness (nm)	Etching time
Fundus illumination area	42.8	2min30sec
Linear stripe pattern	55.7	3min8sec

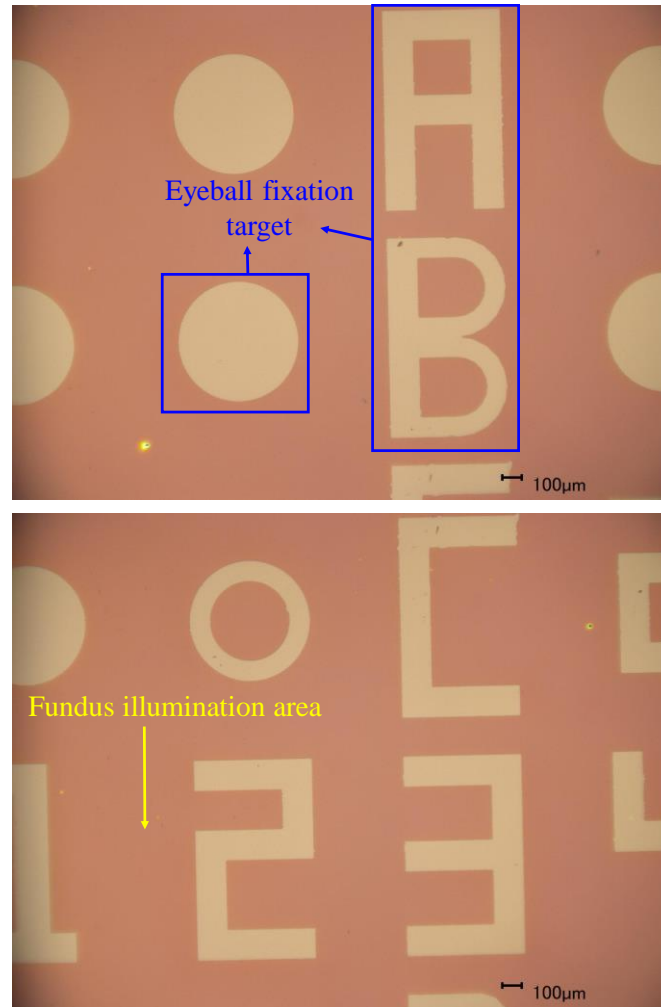


Fig. 4.11 Microphotographs of the eyeball fixation target in the bottom 9-layer film stack after the first cycle of the photolithography and etching.

After the cleaning by an ultrasonic cleaner (ASU-2D, AS ONE, JAPAN), the second cycle of the photolithography and etching was started. Compared with the first time photoresist coating, an adhesion improving material OAP (Tokyo Ohka Kogyo Co., Ltd., Japan) and a positive-type photoresist OFPR-8600 (Tokyo Ohka Kogyo Co., Ltd., Japan) were applied. The mask fabricated following the layout of the linear stripe pattern (shown in Fig. 4.3) was applied to the exposure of the filter by a contact aligner to remove the positive-type photoresist on the linear stripe pattern. The RIE was applied to etch the intermediate layer to form the linear stripe pattern. The etching time follows Equation 12. The microphotographs of the partial area in the fabricated bottom 9-layer film stack are shown in Fig. 4.12. This figure shows the same eyeball

fixation target and linear stripe pattern as the designed layouts, which proves the accuracy of the operations in the photolithography and etching process. The spectrum evaluation of the fabricated 9-layer film stack is shown in the appendix.

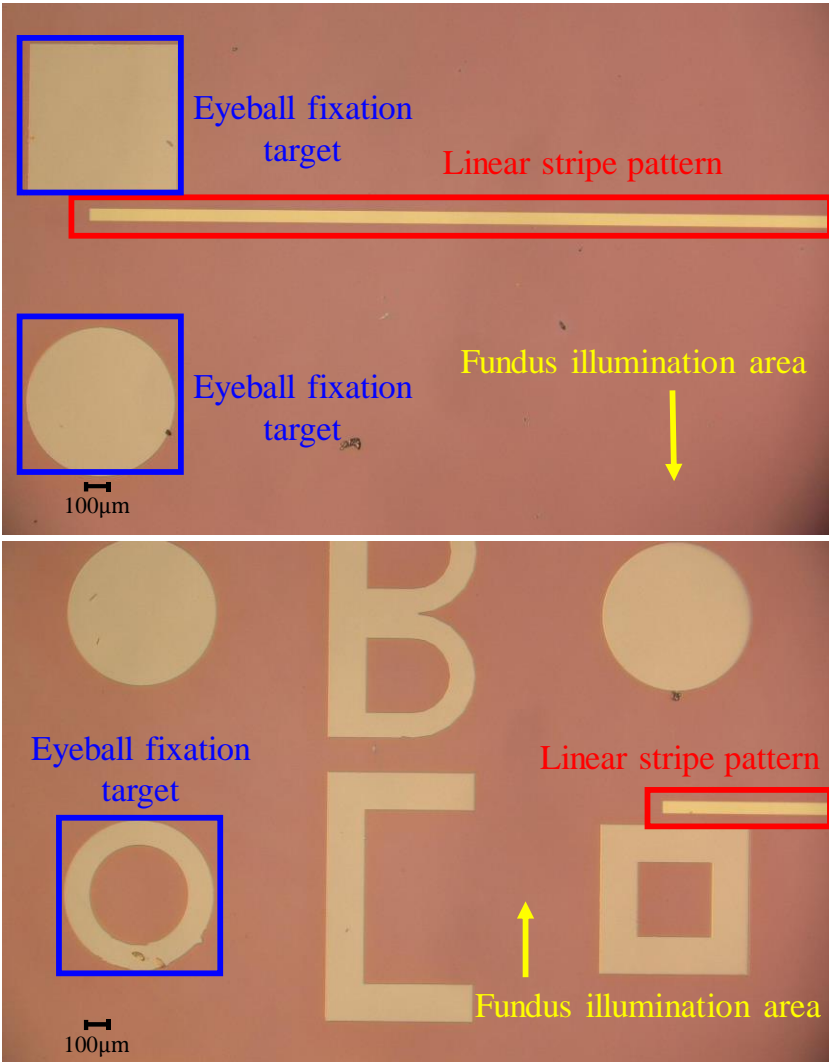


Fig. 4.12 Microphotographs of the partial areas in the fabricated 9-layer film stack.

Thus, the fabrication of the bottom 9-layer film stack was finished. Due to the uncontrollable factors in deposition and etching processes, the thickness of every layer in the fabricated interference filter is different from the thickness in simulation. To detect the thickness error caused during film deposition and etching, the reflectance of the three areas in the 9-layer film stack and 18-layer interference filter was measured. The measured reflection spectrums of

every area show high goodness of fit with the simulated spectrums, which proves every layer thickness of the deposited 9-layer film stack after the deposition and etching is proper. The measured transmission spectrum of the fabricated 9-layer film stack is shown in the appendix for layer thickness error calibration, please move to the appendix for more details. The analysis of the measured transmission spectrum of the 18-layer interference filter is shown in the next section.

To get the multi-functional interference filter with 18 layers, the second time sputtering deposition is needed. The deposition process procedure is the same as the first time. The transmission spectrum of the fabricated multi-functional interference filter with 18 layers will be presented in section 4.4.

4.4 Evaluation of the Multi-Functional Interference Filter

The evaluation method of the fabricated 18-layer multi-functional interference filter is to compare the transmission spectrums obtained by the measurement and simulation. Figure 4.13 shows the transmission spectrum of the fabricated multi-functional interference filter measured by the microscope spectral reflectivity film thickness measurement system. There are three transmittance curves in Fig. 4.13, in which linear stripe pattern and eyeball fixation target have transmittance peak at 800 nm and 660 nm, respectively. All of these three curves have high transmittance in NIR bands to provide sufficient NIR fundus illumination. Compared with simulated transmission spectrum in Fig. 4.7, though the transmittance peak of the eyeball fixation target has an about 20 nm blue shift, the low transmittance around 800 nm and 660 nm, except for the linear stripe pattern and eyeball fixation target, ensured the efficiency of the

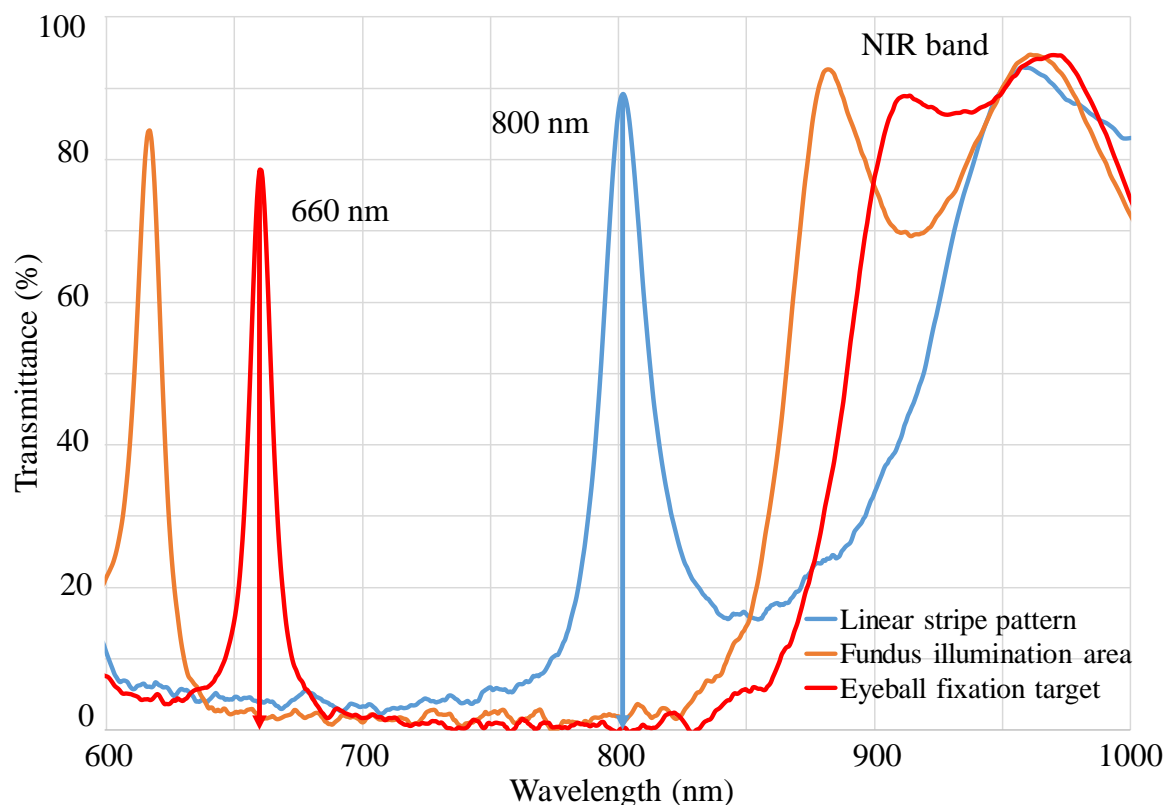


Fig. 4.13 The transmission spectrum of the fabricated multi-functional interference filter measured by the MSRFTM system.

pattern projection on the fundus and eyeball fixation, respectively. Figure 4.14 is the photograph of the fabricated patterned interference filter. The same linear stripe pattern and eyeball fixation target in the fabricated filter as shown in the simulation also proves the success in the fabrication.

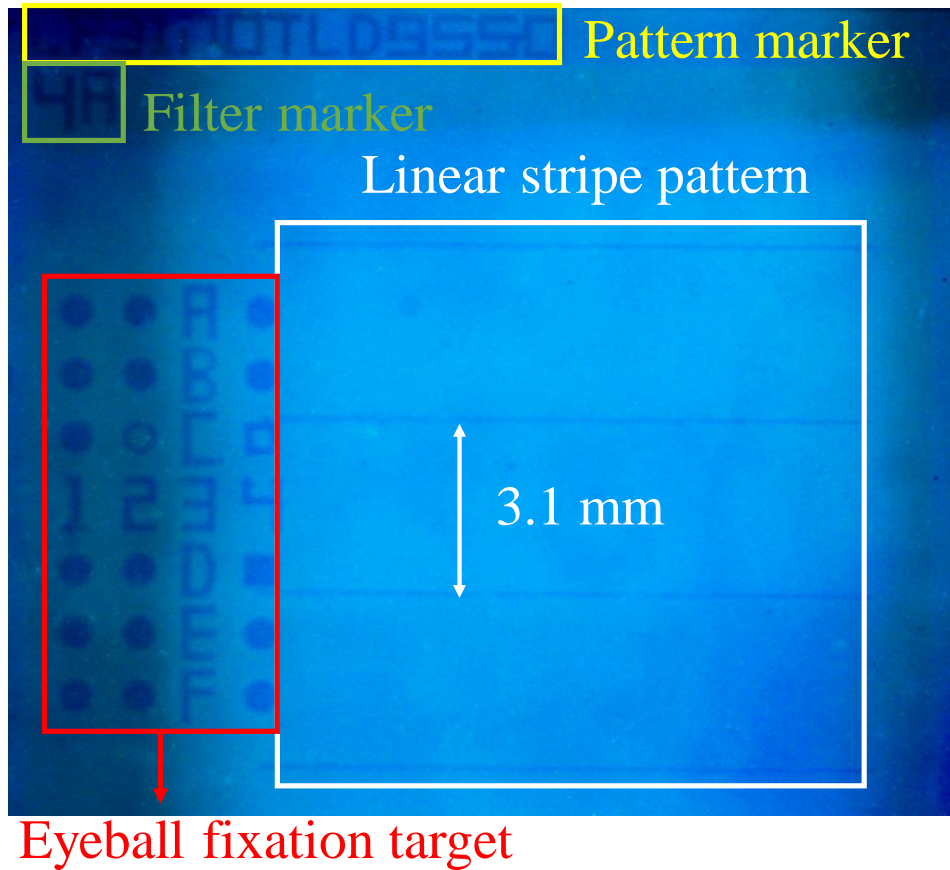


Fig. 4.14 Photograph of the fabricated multi-functional interference filter.

4.5 Summary and Discussion

In this chapter, the design of a multi-functional interference filter, which includes the layout optimization of the projection mask and the transmission spectrum simulation of the multi-functional interference filter with bottom 9-layer and 18-layer, and the fabrication of the multi-functional interference filter was presented. The layout optimization was mainly in the linear stripe pattern and eyeball fixation target. A multi-line and a single-line linear stripe pattern were presented. The optimization of the eyeball fixation target has applied a matrix, which comprises circles, alphabets, and numbers, to replace the concentric circles in the first layout design for accurately eyeball gazing position movement. The transmission spectrum simulation of the multi-functional interference filter follows the Fabry-Perot principle. In this research, the thickness of the intermediate layer in the 18-layer interference filter determined the transmittance. The simulated transmission spectrums for eyeball fixation target, linear stripe pattern, and fundus illumination area show high transmittance at around 680 nm, 800 nm, and NIR bands, respectively, which satisfy the requirements for pattern projection on the fundus.

Three areas mainly presented the fabrication of the multi-functional interference filter in this chapter, the sputtering deposition, the photolithography process, and the etching process. The sputtering deposition of different films followed the fitting curves of silica and titanium dioxide about the deposition time and thickness. Two cycles of the photolithography and the etching processes are needed after the deposition of a bottom 9-layer film stack to form the three areas in the multi-functional interference filter. A negative-type and a positive-type photoresist were applied in the two times photolithography process. The two times etching processes followed the fitting of the etching time and thickness. After the second time sputtering deposition, the transmission spectrum of the fabricated 18-layer multi-functional interference filter was measured. The comparison between the transmission spectrum in simulation and

measurement shows that the wavelengths of transmittance peaks have high similarity, which proves the fabrication of the multi-functional interference filter satisfies the requirement for pattern projection on the fundus.

5. Scattering Detection by Pattern Projection

5.1 Overview

The purpose of the multi-functional interference filter (patterned interference filter) is to project a pattern on the fundus and measure light scattering with a NIR fundus camera. The patterned interference filter was evaluated by measuring the transmission spectrum in the last chapter. This chapter describes the pattern projection on the fundus and scattering experiment with this filter. The same eye model and human eyeball were applied in fundus imaging. The patients can see the linear stripe pattern and eyeball fixation target generated by the patterned interference filter through the ophthalmic lens. The position of the optic disc can be adjusted by moving the gazing position of the patient eyeball in the eyeball fixation target. The linear stripe patterned fundus images with different wavelengths of illumination light were demonstrated to prove the feasibility of pattern projection on the fundus. Besides, the patterned interference filter was also applied in the scattering experiment to check the feasibility of the application of the patterned interference filter in scattering detection.

5.2 Pattern Projection on the Retina with a Multi-Functional Interference Filter

The NIR fundus camera with a fabricated multi-functional interference filter was performed on both a glass eye model and a human eyeball, as they both have a similar optical length and pattern on the fundus. In the case of using LED as the light source for pattern projection, three wavelengths for illumination means that three LEDs are needed. As shown in Fig. 2.5, the LEDs are symmetrically distributed around the center point, which will cause

comatic aberration and astigmatism due to the deviation of the light source center. Thus, an advanced four-channel LED driver (DC4104, THORLABS INC., USA) was applied. The light with three wavelengths, 660 nm, 800 nm, and NIR band, generated by this driver will be transferred by the optical fiber for the pattern projection on the fundus. The schematic diagram of the fundus camera with a patterned interference filter for pattern projection on the fundus is shown in Fig. 5.1. The optical fiber was placed at the position aligned with the center of the light path to decrease the possibility of comatic aberration and astigmatism generation. Figure 5.2 shows the photograph of the fundus camera with a patterned interference filter.

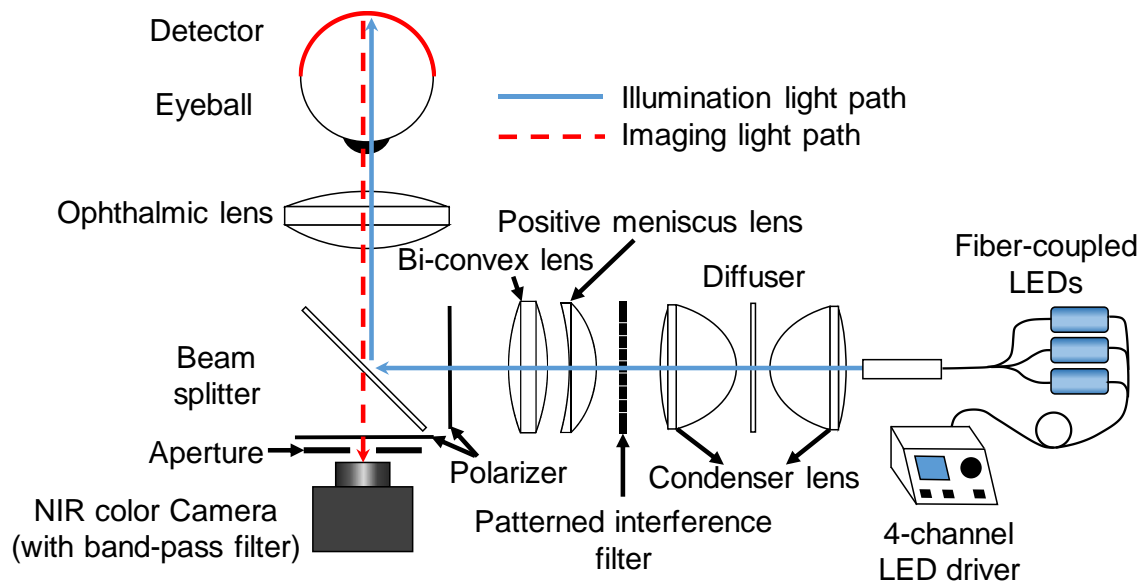


Fig. 5.1 Schematic diagram of the NIR fundus camera with a patterned interference filter for pattern projection on the fundus.

The eye model mentioned in Chapter 2 was applied to the assembled fundus camera for the potential distance error calibration and the fundus observation. The fundus image of the eye model with 800 nm alone as the illumination light is shown in Fig. 5.3. The clear and unique linear stripe in the fundus image proves the low transmittance in the fundus illumination area of 800 nm wavelength light. Due to the large line pitch, other linear stripes cannot be obvious in the fundus image. With the scattering caused by the fundus, we can also obvious the optic

disc and vasculature from the fundus image.

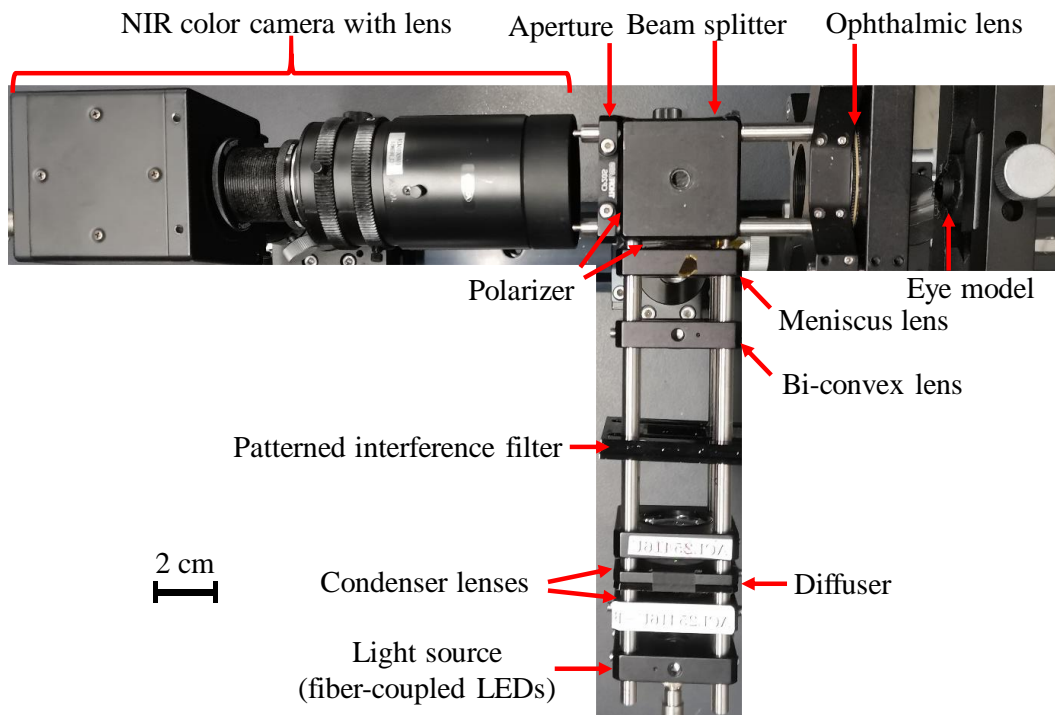


Fig. 5.2 Photograph of the NIR fundus camera with a patterned interference filter for projection on the fundus.

After the fundus observation with the eye model, the NIR fundus camera with a patterned interference filter was applied to human eyeball fundus observation. During the fundus observation by the NIR fundus camera with a patterned interference filter, the patient can see the image shown in Fig. 5.4 with 660 nm wavelength light illumination. Due to the fundus illumination area has a transmittance peak close to 660 nm, the red light pass from the fundus illumination area can be observed, while the linear stripe pattern is dark. Figure 5.5 shows the image of the patient can observe when the illumination light is 800 nm wavelength. The eyeball fixation target and fundus illumination area are dark due to the low transmittance at 800 nm.

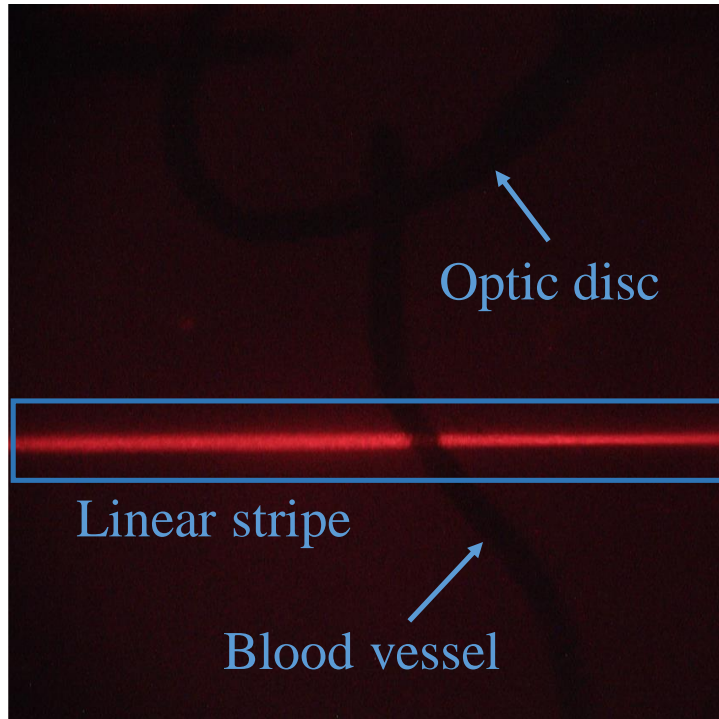


Fig. 5.3 Fundus image of the eye model with a linear stripe illuminate by 800 nm light.

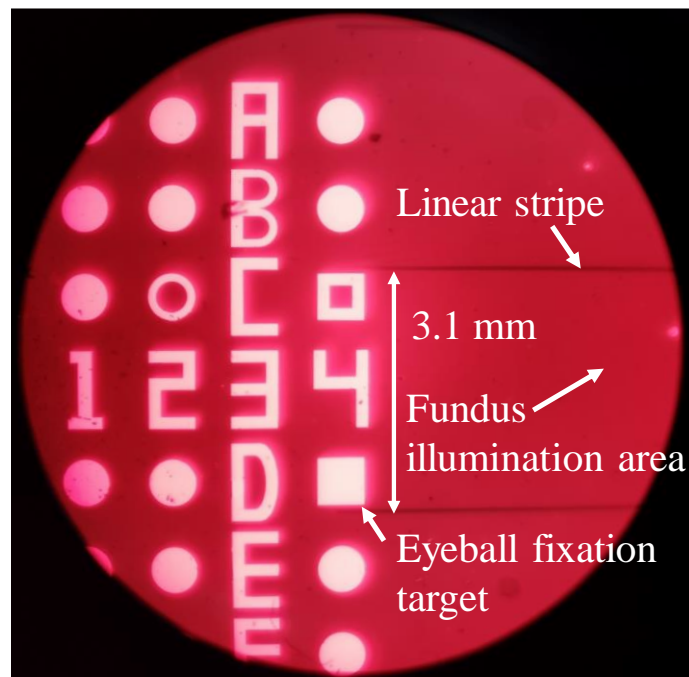


Fig. 5.4 The observed image through the ophthalmic lens in the NIR fundus camera with a patterned interference filter with 660 nm wavelength light illumination.

Though 800 nm is invisible to the human eye, the image shown in Fig. 5.5 can still be taken by the smartphone. These observed images from the ophthalmic lens prove the fabricated patterned interference filter satisfy the requirements for pattern projection on the fundus. In Fig. 5.4, the patient can gaze on the different positions in the eyeball fixation target to slightly adjust the relative position between the optic disc and linear stripe by following the instructions from the observer. Thus, it can be easier to achieve the fundus linear stripe patterned illumination.

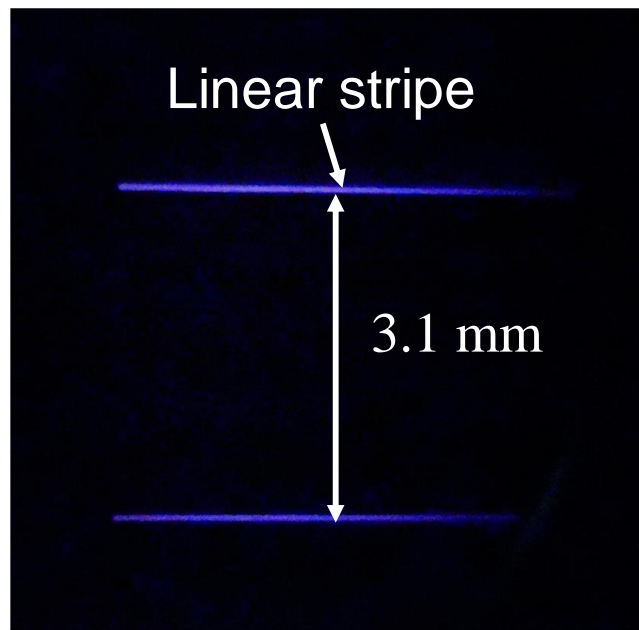


Fig. 5.5 The observed image through the ophthalmic lens in the NIR fundus camera with a patterned interference filter with 800 nm wavelength light illumination.

Figure 5.6 shows two fundus images with the linear stripe patterned illumination. In Fig. 5.6(a), the wavelength of the illumination light is 660 nm, high transmittance in eyeball fixation target for eyeball fixation, and 800 nm, high transmittance in linear stripe pattern for linear stripe patterned illumination. In Fig. 5.6(b), besides the 660 nm and 800 nm, a NIR band light for fundus illumination was applied for fundus observation. Due to the eye model background is composed of the absorption material, so less scattering was generated. While the fundus is composed of the vasculature and tissues, all these things have a higher reduced scattering coefficient, and a higher scattering will be generated. Thus, compared with Fig. 5.3, a wider

fundus can be observed from Fig. 5.6, which also be illuminated by a linear stripe light beam.

Figure 5.6(b) is a fundus image obtained by simultaneous illumination of three wavelengths of light. Compared with Fig. 5.6(a), the fundus can be easier observed in Fig. 5.6(b) under the NIR light illumination. Thus, for better fundus linear stripe pattern illumination, the fundus observation with NIR light is needed. The linear stripe patterned fundus images prove the feasibility of pattern projection on the fundus by the NIR fundus camera with a patterned interference filter.

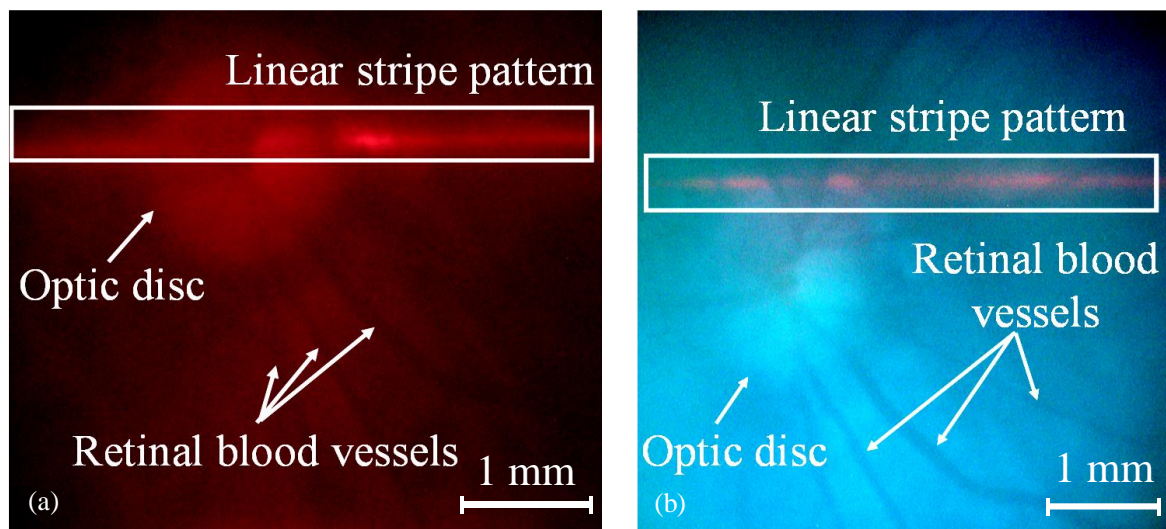


Fig. 5.6 Fundus images of the human eyeball taken by the NIR fundus image with the patterned interference filter by the linear stripe patterned illumination light with (a) 660 nm and 800 nm, (b) 660 nm, 800 nm, and NIR band.

5.3 Scattering Experiments with a Multi-Functional Interference Filter

The fabricated patterned interference filter was applied to scattering experiments to check the feasibility of lipid concentration detection. The schematic diagram of the scattering detection system is shown in Fig. 5.7. The artificial blood applied in this experiment has the same reduced scattering coefficient as Table 3.1. Figure 5.8 shows the linear stripe patterned light generated by the fabricated patterned interference filter on a glass tube filled with artificial blood. Due to the transmittance of the linear stripe pattern is not as high as the 100% transmittance in the patterned metal mask, so the illumination light intensity in this scattering experiment is lower than mentioned in Chapter 3.

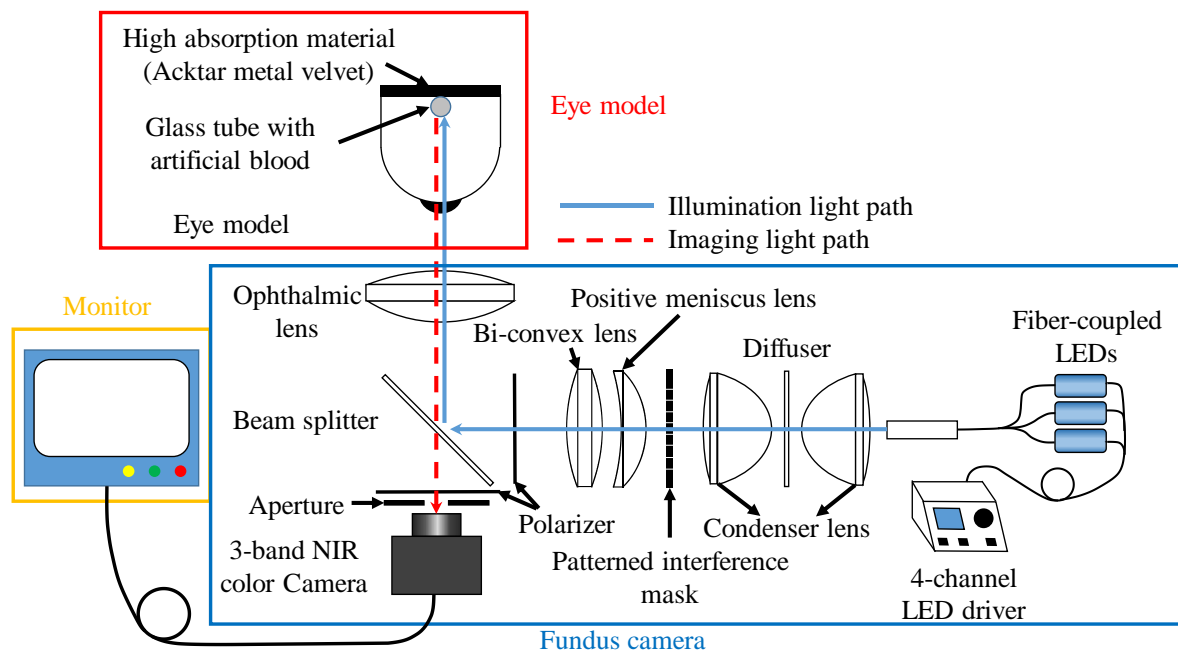


Fig. 5.7 Schematic diagram of the scattering detection system.

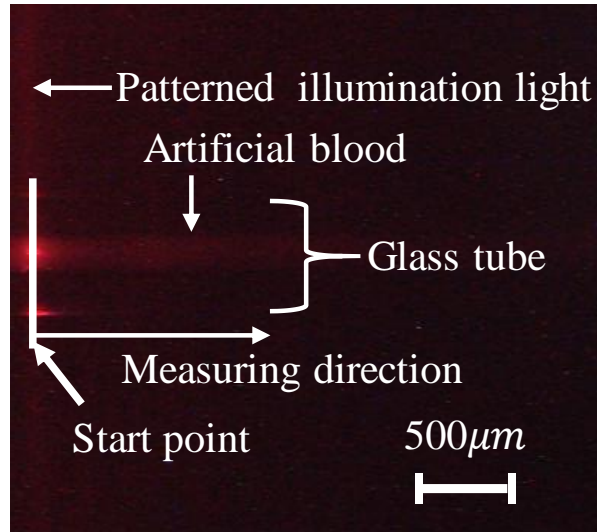


Fig. 5.8 Photograph of the linear stripe patterned light on a glass tube filled by artificial blood.

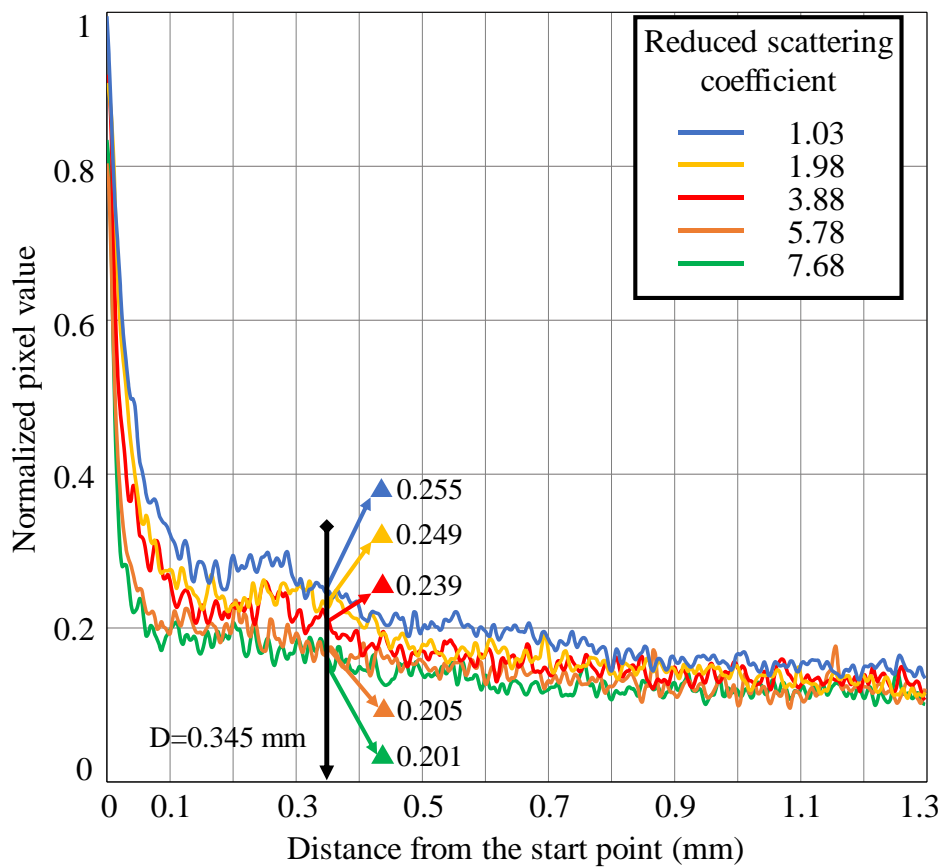


Fig. 5.9 Normalized pixel values for different scattering lengths of the artificial blood with different reduced scattering coefficients.

The measured scattering relationship for the artificial blood with different reduced scattering coefficients is shown in Fig. 5.9. This figure shows that the scattering intensity (normalized pixel value) is different under the same scattering distance for the artificial blood with different lipid concentration (reduced scattering coefficient). Same as the scattering experiment in Chapter 3, the scattering intensity when the scattering distance is 0.345 mm was selected to avoid the effect from the illumination light. Fig. 5.10 shows relationship curve between the scattering intensity and the lipid concentration when the scattering distance equal to 0.345 mm. In this figure, the scattering intensity is increasing with the lipid concentration increasing, which demonstrates the scattering intensity has a positive correlation with the lipid concentration. Though the differences between the scattering relationship of different artificial blood can only be easily distinguished at a short scattering distance, the feasibility of lipid concentration detection with the measured scattering information by the NIR fundus camera with a patterned interference filter was proved.

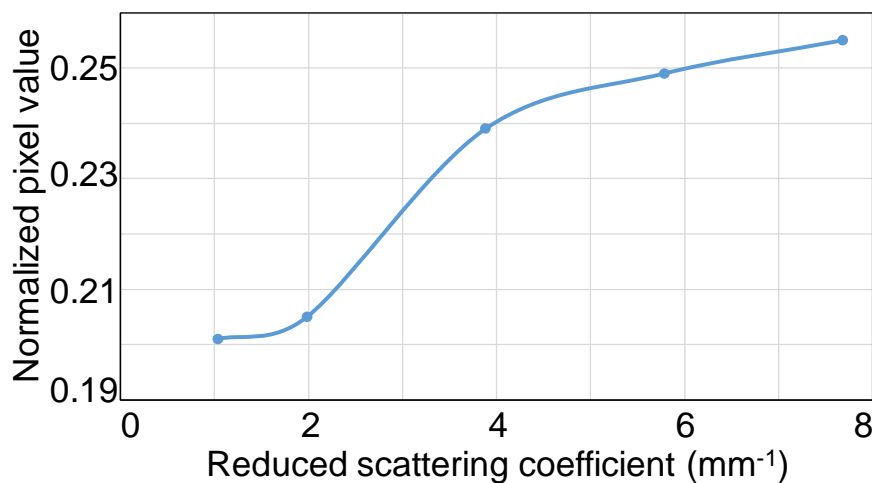


Fig. 5.10 Normalized pixel values for different reduced scattering coefficient when scattering distance equal to 0.345 mm.

5.4 Summary and Discussion

The fabricated patterned interference filter was applied to the fundus imaging and the scattering experiment in this chapter. The results demonstrate the feasibility of using the NIR fundus camera with a patterned interference filter for pattern projection on the fundus and the lipid concentration detection. In the fundus imaging, the LEDs with 660 nm, 800 nm, and NIR bands were coupled into a fiber as the light source for illumination. With the multi-wavelength illumination light, the comparison of the fundus images, including the NIR band's light or not, demonstrates the use of each area of the fabricated patterned interference filter in fundus imaging. In the scattering experiment, with the measurement system mentioned in chapter 3, though the scattering intensity decreased rapidly with distance increased, the measured scattering relationship shows a high correlation with the reduced scattering coefficient in the artificial blood. This correlation shows the feasibility of measuring the lipid concentration by the NIR fundus camera with a patterned interference filter.

6. Conclusion

6.1 Summary

This research presents the design and fabrication of a multi-spectral NIR fundus camera with a patterned interference filter for light scattering detection. The fundus camera provides a noninvasive way to observe the fundus for disease diagnosis and health care. With the development of fundus cameras, high resolution and large field of view fundus images are available for disease diagnosis. Still, the surface fundus images alone cannot satisfy the requirements for health checks and disease prevention noninvasively, and the information about the fundus tissues is indispensable. To solve this problem, we proposed a multi-spectral NIR fundus camera with a patterned interference filter for light scattering detection, which can be applied to health checks and disease prevention. The design and fabrication of this fundus camera were presented in this research.

A fundus camera for fundus observation was simulated and assembled as a platform for developing the fundus camera for light scattering detection. A linear stripe projection mask and a lens group were added to the traditional fundus camera for pattern projection. The lens type and optical path were adjusted to project the linear stripe pattern with less distortion on the fundus in the simulation. The uniformity evaluation of the pattern projected on the fundus shows apparent boundaries between the adjacent linear stripes and high uniformity, which proves the feasibility of the pattern projection. Then layouts of the projection mask were designed considering the human fundus structure. Besides the linear stripe pattern in the simulation, an eyeball fixation target was added for a more manageable pattern projection. The patterned metal mask fabricated following the designed layout was added into the assembled fundus camera for pattern projection on the human fundus. In addition to the clear linear stripe

pattern, the fundus images with linear stripe pattern illumination also portray the apparent optic disc, fundus vasculature and, tissues. Thus, the feasibility of the pattern projection on the human fundus by a NIR fundus camera with a patterned metal mask was proved.

The NIR fundus camera with a patterned metal mask was applied to detect the light scattering from artificial blood. Capillary glass tubes filled with artificial blood, a mixture with different reduced scattering coefficients to emulate the lipid scattering properties in human blood, were applied in the scattering experiments to mimic fundus blood vessels. The high correlation between the measured scattering relationship and the scattering properties of the artificial blood from the experimental results proves the feasibility of the lipid concentration measurement by the NIR fundus camera with a patterned metal mask.

Following the advice of the patients during the pattern projection on the fundus and the scattering distance from the scattering detection by the fundus camera with a patterned metal mask, the layout of the projection mask was optimized for patterned interference filter fabrication. The pitch of the linear stripe increased to avoid the interaction between the adjacent linear light, and a matrix composed of numbers, alphabet, and circles replaces the donuts as the eyeball fixation target for a more manageable eyeball fixation. The fabrication of the patterned interference filter mainly includes sputtering deposition, photolithography, and the etching process. The bottom 9-layer film stack of the multi-functional interference filter was deposited on the glass substrate for the intermediate layer thickness adjustment by photolithography and etching process. The deposition and etching thicknesses were well controlled by time and the pre-confirmed rate. The transmittance of each area in the patterned interference filter was evaluated after the deposition of the top nine layers. The measured transmission spectrum of the fabricated patterned interference filter shows similar wavelengths of the transmittance peak as the simulation, which proves the fabricated patterned interference filter satisfies the requirements of the pattern projection.

Besides the evaluation by the transmission spectrum measurement, the fabricated patterned interference filter was applied to pattern projection on the fundus and scattering detection. The apparent linear stripe and fundus tissues proves the feasibility of the pattern projection on the human fundus, and the high correlation between the scattering relationship and the scattering properties of artificial blood demonstrates the feasibility of the application of the fabricated patterned interference filter in the lipid concentration measurement.

The proposed multi-spectral NIR fundus camera with a patterned interference filter was proved by the results mentioned above from the scattering experiment and linear stripe patterned fundus observation that it can be used for lipid concentration measurement and pattern projection on the fundus.

6.2 Future Plan

This thesis demonstrates a multi-spectral NIR fundus camera with a patterned interference filter to achieve the light scattering detection target. Research never stops, there are still kind of open opportunities to improve this light scattering detection system.

Though the feasibility of the lipid concentration measurement by the multi-spectral NIR fundus camera with a patterned interference filter was proved, the quantitative analysis of lipid concentration is still hard to achieve at the present stage. The quantitative analysis of lipid concentration needs to satisfy the following requirements. The first one is a higher resolution and sensitivity imaging system, which can decrease the noises from the experimental environment. With lower noises in the captured images, the averaged scattering intensity curve can be more smooth to obtain a clear fitting curve about the scattering information and lipid concentration. Furthermore, with the higher performance imaging system, the repeatable scattering experiments between the experimental group and control group with different lipid

concentrations are needed. The experimental group in the repeatable experiments is used for verifying the reliability of the fitting curve about the scattering information and lipid concentration obtained from the control group. Thus, a more accurate fitting curve is available.

With the accurate fitting curve of the relationship between the scattering information and the lipid concentration, the multi-spectral NIR fundus camera with a patterned interference filter can be applied to the health check and disease prevention. The portable size of this fundus camera makes it is possible to do disease diagnosis and health checks at home by a doctor with an internet connection. Combined with artificial intelligence algorithms, patients can even conduct disease diagnosis and health checks independently.

References

- [1] E. DeHoog and J. Schwiegerling, “Optimal parameters for retinal illumination and imaging in fundus cameras,” *Appl. Opt.*, vol. 47, no. 36, p. 6769, Dec. 2008.
- [2] W. T. W. J. Jackman, “On photographing the retina of the living human eye.,” *Philadelphia Photogr.*, vol. xxiii, no. 275, pp. 340–341, 1886.
- [3] H. Davson, Ed., *Visual Optics and the Optical Space Sense*. Elsevier, 1962.
- [4] L. Ayton, “The Retinal Atlas – Second Edition K Bailey Freund, David Sarraf, William F Mieler, Lawrence A Yannuzzi Elsevier 2016, 1,173 pages, RRP \$404,” *Clin. Exp. Optom.*, vol. 100, no. 4, pp. 407–407, Jul. 2017.
- [5] T. Behrendt and L. A. Wilson, “Spectral Reflectance Photography of the Retina.,” *Am. J. Ophthalmol.*, vol. 59, pp. 1079–88, Jun. 1965, [Online].
- [6] B. Dobbin, “Kodak engineer had revolutionary idea: the first digital camera.” <https://www.seattlepi.com/business/article/Kodak-engineer-had-revolutionary-idea-the-first-1182624.php>.
- [7] F. LaRocca, D. Nankivil, S. Farsiu, and J. A. Izatt, “Handheld simultaneous scanning laser ophthalmoscopy and optical coherence tomography system,” *Biomed. Opt. Express*, vol. 4, no. 11, p. 2307, 2013.
- [8] N. Panwar, P. Huang, J. Lee, P. A. Keane, T. S. Chuan, A. Richhariya, S. Teoh, T. H. Lim, and R. Agrawal, “Fundus photography in the 21st century -a review of recent technological advances and their implications for worldwide healthcare,” *Telemedicine and e-Health*, vol. 22, no. 3, pp. 198–208, Mar. 2016.
- [9] Y. Cui, T. Takamatsu, K. Shimizu, and T. Miyake, “Near-infrared fundus imaging system with light illumination from an electronic contact lens,” *Applied Physics Express*, vol. 15, no. 2, p. 027001, 2022.
- [10] T. Teng, M. Lefley, and D. Claremont, “Progress towards automated diabetic ocular screening: A review of image analysis and intelligent systems for diabetic retinopathy,” *Med. Biol. Eng. Comput.*, vol. 40, no. 1, pp. 2–13, Jan. 2002.
- [11] K. S. Lin, C. L. Tsai, M. Sofka, C. H. Tsai, S. J. Chen, and W. Y. Lin, “A telemedical approach to the screening of diabetic retinopathy: digital fundus photography.,” *Diabetes Care*, vol. 23, no. 3, pp. 345–348, Mar. 2000.
- [12] K. S. Lin, C. L. Tsai, M. Sofka, C. H. Tsai, S. J. Chen, and W. Y. Lin, “Vascular Tree Construction with Anatomical Realism for Retinal Images,” in *2009 Ninth IEEE*

- International Conference on Bioinformatics and BioEngineering*, Jun. 2009, pp. 313–318.
- [13] B. Al-Diri, A. Hunter, D. Steel, and M. Habib, “Automated analysis of retinal vascular network connectivity,” *Comput. Med. Imaging Graph.*, vol. 34, no. 6, pp. 462–470, Sep. 2010.
- [14] S. M. Heringa, W. H. Bouvy, E. Van Den Berg, A. C. Moll, L. Jaap Kappelle, and G. Jan Biessels, “Associations between retinal microvascular changes and dementia, cognitive functioning, and brain imaging abnormalities: A systematic review,” *J. Cereb. Blood Flow Metab.*, vol. 33, no. 7, pp. 983–995, 2013.
- [15] C. Cheung, C. Chen, and T. Wong, “Ocular Fundus Photography as a Tool to Study Stroke and Dementia,” *Semin. Neurol.*, vol. 35, no. 05, pp. 481–490, Oct. 2015.
- [16] S. McGrory, J. R. Cameron, E. Pellegrini, C. Warren, F. N. Doubal, I. J. Deary, B. Dhillon, J. M. Wardlaw, E. Trucco, and T. J. MacGillivray, “The application of retinal fundus camera imaging in dementia: A systematic review,” *Alzheimer’s Dement. Diagnosis, Assess. Dis. Monit.*, vol. 6, pp. 91–107, 2017.
- [17] H. Takehara, H. Sumi, W. Ze, T. Kondo, M. Haruta, K. Sasagawa, and J. Ohta, “Multispectral Near-infrared Imaging Technologies for Nonmydriatic Fundus Camera,” *BioCAS 2019 - Biomed. Circuits Syst. Conf. Proc.*, pp. 1–4, 2019.
- [18] H. Sumi, H. Takehara, S. Miyazaki, D. Shirahige, K. Sasagawa, T. Tokuda, Y. Watanabe, N. Kishi, J. Ohta, and M. Ishikawa, “Next-generation fundus camera with full color image acquisition in 0-lx visible light by 1.12-micron square pixel, 4K, 30-fps BSI CMOS image sensor with advanced NIR multi-spectral imaging system,” *Dig. Tech. Pap. - Symp. VLSI Technol.*, vol. 2018-June, pp. 163–164, 2018.
- [19] R. Michels, F. Foschum, and A. Kienle, “Optical properties of fat emulsions,” *Opt. Express*, vol. 16, no. 8, p. 5907, 2008.
- [20] D. Hope, “Photograph of the retina of the human eye, with overlay diagrams showing the positions and sizes of the macula, fovea, and optic disc.pdf.” <https://commons.wikimedia.org/wiki/File:Macula.svg>.
- [21] S. A. B. S. B Cassin, *Dictionary of Eye Terminology*, 2nd ed. Gainesville, Florida: Triad Pub Co, 1990.
- [22] M. Hammer, A. Roggan, D. Schweitzer, and G. Muller, “Optical properties of ocular fundus tissues-an in vitro study using the double-integrating-sphere technique and inverse Monte Carlo simulation,” *Phys. Med. Biol.*, vol. 40, no. 6, pp. 963–978, Jun. 1995.
- [23] D. K. Sardar, G. Y. Swanland, R. M. Yow, R. J. Thomas, and A. T. C. Tsin, “Optical

- properties of ocular tissues in the near infrared region,” *Lasers Med. Sci.*, vol. 22, no. 1, pp. 46–52, 2007.
- [24] T. J. T. P. van den Berg and H. Spekreijse, “Near infrared light absorption in the human eye media,” *Vision Res.*, vol. 37, no. 2, pp. 249–253, Jan. 1997.
- [25] J. J. Vos, A. A. Munnik, and J. Boogaard, “Absolute Spectral Reflectance of the Fundus Oculi,” *J. Opt. Soc. Am.*, vol. 55, no. 5, p. 573, 1965.
- [26] B. G. Yust, L. C. Mimun, and D. K. Sardar, “Optical absorption and scattering of bovine cornea, lens, and retina in the near-infrared region,” *Lasers Med. Sci.*, vol. 27, no. 2, pp. 413–422, 2012.
- [27] P. Thueler, I. Charvet, F. Bevilacqua, M. St. Ghislain, G. Ory, P. Marquet, P. Meda, B. Vermeulen, and C. Depeursinge, “In vivo endoscopic tissue diagnostics based on spectroscopic absorption, scattering, and phase function properties,” *J. Biomed. Opt.*, vol. 8, no. 3, p. 495, 2003.
- [28] “光で静脈血を測定する非侵襲濁度計.” [Online]. [Japanese Reference]
- [29] K. Shimizu, K. Tochio, and Y. Kato, “Improvement of transcutaneous fluorescent images with a depth-dependent point-spread function,” *Appl. Opt.*, vol. 44, no. 11, pp. 2154–2161, 2005.
- [30] S. A. P. Steven L. Jacques, “Reduced scattering coefficient,” 1998. <https://omlc.org/classroom/ece532/class3/musp.html>.
- [31] M. Wiesmann, A. J. Kiliaan, and J. A. Claassen, “Vascular Aspects of Cognitive Impairment and Dementia,” *J. Cereb. Blood Flow Metab.*, vol. 33, no. 11, pp. 1696–1706, Nov. 2013.
- [32] D. S. Knopman, “Dementia and Cerebrovascular Disease,” *Mayo Clin. Proc.*, vol. 81, no. 2, pp. 223–230, Feb. 2006.
- [33] A. London, I. Benhar, and M. Schwartz, “The retina as a window to the brain - From eye research to CNS disorders,” *Nat. Rev. Neurol.*, vol. 9, no. 1, pp. 44–53, 2013.
- [34] N. Patton, T. Aslam, T. MacGillivray, A. Pattie, I. J. Deary, and B. Dhillon, “Retinal vascular image analysis as a potential screening tool for cerebrovascular disease: a rationale based on homology between cerebral and retinal microvasculatures,” *J. Anat.*, vol. 206, no. 4, pp. 319–348, Apr. 2005.
- [35] C. Y. L. Cheung, Y. T. Ong, M. K. Ikram, S. Y. Ong, X. Li, S. Hilal, J. A. S. Catindig, N. Venkatasubramanian, P. Yap, D. Seow, C. P. Chen, and T. Y. Wong, “Microvascular network alterations in the retina of patients with Alzheimer’s disease,” *Alzheimer’s and*

- Dementia*, vol. 10, no. 2. pp. 135–142, 2014.
- [36] M. K. Ikram, F. J. De Jong, E. J. Van Dijk, N. D. Prins, A. Hofman, M. M. B. Breteler, and P. T. V. M. De Jong, “Retinal vessel diameters and cerebral small vessel disease: the Rotterdam Scan Study,” *Brain*, vol. 129, no. 1, pp. 182–188, Jan. 2006.
- [37] K. Okubo, Y. Kitagawa, N. Hosokawa, M. Umezawa, M. Kamimura, T. Kamiya, N. Ohtani, and K. Soga, “Visualization of quantitative lipid distribution in mouse liver through near-infrared hyperspectral imaging,” *Biomed. Opt. Express*, vol. 12, no. 2, p. 823, 2021.
- [38] T. D. Weber and J. Mertz, “Non-mydratic chorioretinal imaging in a transmission geometry and application to retinal oximetry,” *Non-mydratic chorioretinal imaging a Transm. Geom. Appl. to Retin. oximetry*, p. 314765, 2018.
- [39] W. S. Hee, K. Sasagawa, A. Kameyama, A. Kimura, M. Haruta, T. Tokuda, and J. Ohta, “Lens-free dual-color fluorescent CMOS image sensor for Förster resonance energy transfer imaging,” *Sensors Mater.*, vol. 31, no. 3, pp. 2579–2594, 2019.
- [40] K. Sasagawa, A. Kimura, M. Haruta, T. Noda, T. Tokuda, and J. Ohta, “Highly sensitive lens-free fluorescence imaging device enabled by a complementary combination of interference and absorption filters,” *Biomed. Opt. Express*, vol. 9, no. 9, p. 4329, 2018.
- [41] S. G. Lipson, H. Lipson, and D. S. Tannhauser, “Optical Physics,” *Optical Physics*. 1995.
- [42] G. Hernandez, *Fabry-perot interferometer*. Cambridge University Press, 1986.
- [43] Z. Wang, M. Uemura, H. Takehara, M. Haruta, H. Tashiro, K. Sasagawa, and J. Ohta, “Near-infrared fundus camera with a patterned interference filter for the retinal scattering detection,” *Jpn. J. Appl. Phys.*, vol. 60, no. SB, p. SBBL07, May 2021.
- [44] NIDEK, “眼底撮影に特化したコンパクトな手持ちカメラ デジタルメディカルスコープ DS-20Fを発売,” 2016. [Online] [Japanese Reference]
- [45] Nanolux, “Core Technology Transform ‘invisible’ to ‘visible.’” https://www.nanolux.co.jp/english/technology_en/.
- [46] T. Lian, K. J. MacKenzie, D. H. Brainard, N. P. Cottaris, and B. A. Wandell, “Ray tracing 3D spectral scenes through human optics models,” *J. Vis.*, vol. 19, no. 12, pp. 1–17, 2019.
- [47] J. Schwiegerling, *Field Guide to Visual and Ophthalmic Optics*. SPIE, 2009.
- [48] J. Lin, D. Cheng, C. Yao, and Y. Wang, “Retinal projection head-mounted display,” *Front. Optoelectron.*, vol. 10, no. 1, 2017.
- [49] Q. F. Li Chun, Sun Qiang, Liu Ying, Lu Xinqi, Wang Jian, Sun Jinxia, Liu Jianzhuo, “眼底相机的均匀照明及消杂光干扰设计,” *Chinese J. Opt. Appl. Opt.*, vol. 3, no. 4, pp.

- 363–368, 20210, [Chinese Reference].
- [50] Y. Ding, X. Liu, Z. Zheng, and P. Gu, “Freeform LED lens for uniform illumination,” *Opt. Express*, vol. 16, no. 17, p. 12958, Aug. 2008.
- [51] R. A. Jonas, Y. X. Wang, H. Yang, J. J. Li, L. Xu, S. Panda-Jonas, and J. B. Jonas, “Optic disc -Fovea distance, axial length and parapapillary Zones. The Beijing eye study 2011,” *PLoS ONE*, vol. 10, no. 9. 2015.
- [52] S. Martinez-Conde, S. L. Macknik, and D. H. Hubel, “The role of fixational eye movements in visual perception,” *Nat. Rev. Neurosci.*, vol. 5, no. 3, pp. 229–240, 2004.
- [53] S. Takatani and M. D. Graham, “Theoretical Analysis of Diffuse Reflectance from a Two-Layer Tissue Model,” *IEEE Transactions on Biomedical Engineering*, vol. BME-26, no. 12. pp. 656–664, 1979.
- [54] S. Prahl, “Optical Absorption of Hemoglobin.” <https://omlc.org/spectra/hemoglobin/>.
- [55] D. J. Faber, M. C. G. Aalders, E. G. Mik, B. A. Hooper, M. J. C. Van Gemert, and T. G. Van Leeuwen, “Oxygen saturation-dependent absorption and scattering of blood,” *Physical Review Letters*, vol. 93, no. 2. 2004.
- [56] A. N. Yaroslavsky, I. V. Yaroslavsky, T. Goldbach, and H. J. Schwarzmaier, “Optical properties of blood in the near-infrared spectral range,” in *Proceedings of SPIE - The International Society for Optical Engineering*, May 1996, vol. 2678, pp. 314–324.
- [57] A. Ishimaru, *Wave propagation and scattering in random media*. Academic Press, INC., 1999.
- [58] W. C. Malm, “Monitoring Visibility,” *Visibility*. pp. 201–245, 2016.
- [59] V. V Tuchin, *Handbook of Optical Biomedical Diagnostics: SPIE Society of Photo-Optical Instrumentation Engineering*, vol. 1. 2016.
- [60] H. Nakazawa, M. Doi, E. Ogawa, and T. Arai, “Modified optical coefficient measurement system for bulk tissue using an optical fiber insertion with varying field of view and depth at the fiber tip,” *Lasers Med. Sci.*, vol. 34, no. 8, pp. 1613–1618, 2019.
- [61] T. Hirasawa, M. Ishihara, K. Tsujita, K. Hirota, K. Irisawa, M. Kitagaki, M. Fujita, and M. Kikuchi, “Continuous wavelet-transform analysis of photoacoustic signal waveform to determine optical absorption coefficient,” in *Photons Plus Ultrasound: Imaging and Sensing 2012*, 2012, vol. 8223, p. 822333.
- [62] T. Sakai, W. Manabe, T. Kamitani, E. Takeyama, and S. Nakano, “Ropivacaine-induced late-onset systemic toxicity after transversus abdominis plane block under general anesthesia: Successful reversal with 20% lipid emulsion,” *Japanese J. Anesthesiol.*, vol.

- 59, no. 12, pp. 1502–1505, Dec. 2010.
- [63] Z. Guo, S. Hu, and L. V. Wang, “Calibration-free absolute quantification of optical absorption coefficients using acoustic spectra in 3D photoacoustic microscopy of biological tissue,” *Opt. Lett.*, vol. 35, no. 12, p. 2067, 2010.
- [64] T. Hirasawa, M. Fujita, S. Okawa, T. Kushibiki, and M. Ishihara, “Improvement in quantifying optical absorption coefficients based on continuous wavelet-transform by correcting distortions in temporal photoacoustic waveforms,” in *Photons Plus Ultrasound: Imaging and Sensing 2013*, 2013, vol. 8581, p. 85814J.
- [65] H. Komatsu, A. Kitajima, and S. Okada, “Pharmaceutical Characterization of Commercially Available Intravenous Fat Emulsions: Estimation of Average Particle Size, Size Distribution and Surface Potential Using Photon Correlation Spectroscopy.,” *Chem. Pharm. Bull.*, vol. 43, no. 8, pp. 1412–1415, 1995.
- [66] Q. Liu, C. Zhu, and N. Ramanujam, “Experimental validation of Monte Carlo modeling of fluorescence in tissues in the UV-visible spectrum,” *J. Biomed. Opt.*, vol. 8, no. 2, p. 223, 2003.
- [67] H. Xu and M. S. Patterson, “Determination of the optical properties of tissue-simulating phantoms from interstitial frequency domain measurements of relative fluence and phase difference,” *Opt. Express*, vol. 14, no. 14, p. 6485, 2006.
- [68] F. Martelli and G. Zaccanti, “Calibration of scattering and absorption properties of a liquid diffusive medium at NIR wavelengths CW method,” *Opt. Express*, vol. 15, no. 2, p. 486, Jan. 2007.
- [69] N. Rajaram, T. H. Nguyen, and J. W. Tunnell, “Lookup table–based inverse model for determining optical properties of turbid media,” *J. Biomed. Opt.*, vol. 13, no. 5, p. 050501, 2008.
- [70] P. Di Ninni, F. Martelli, and G. Zaccanti, “The use of India ink in tissue-simulating phantoms,” *Optics Express*, vol. 18, no. 26, p. 26854, 2010.
- [71] D. D. Royston, “Optical properties of scattering and absorbing materials used in the development of optical phantoms at 1064 nm,” *J. Biomed. Opt.*, vol. 1, no. 1, p. 110, 1996.
- [72] V. V. Tuchin, *Tissue Optics: Light Scattering Methods and Instruments for Medical Diagnosis*. Society of Photo-Optical Instrumentation Engineers (SPIE), 2015.
- [73] S. Liang and K. Shimizu, “Development of a technique to measure local scattering in turbid media using backscattered light at the surface for noninvasive turbidity evaluation of blood in subcutaneous blood vessels,” *Jpn. J. Appl. Phys.*, vol. 60, no. 2, p. 022002, Feb.

2021.

- [74] D. Goldenberg, J. Shahar, A. Loewenstein, and M. Goldstein, “Diameters of retinal blood vessels in a healthy cohort as measured by spectral domain optical coherence tomography,” *Retina*, vol. 33, no. 9, pp. 1888–1894, Oct. 2013.
- [75] G. D. Chanana and B. B. Sheth, “Particle size reduction of emulsions by formulation design. I: Effect of polyhydroxy alcohols.,” *J. Parenter. Sci. Technol.*, vol. 47, no. 3, pp. 130–4, [Online].
- [76] B. W. Shen, A. M. Scanu, and F. J. Kezdy, “Structure of human serum lipoproteins inferred from compositional analysis,” in *Proceedings of the National Academy of Sciences of the United States of America*, 1977, vol. 74, no. 3, pp. 837–841.
- [77] 钟文婷, “新型LED光源雷达大气气溶胶探测技术研究实验观测,” 西安理工大学, 2019. [Chinese Reference]
- [78] C. F. Bohren and D. R. Huffman, *Absorption and Scattering of Light by Small Particles*. Wiley, 1998.
- [79] G. Mie, “Beiträge zur Optik trüber Medien, speziell kolloidaler Metallösungen,” *Ann. Phys.*, vol. 330, no. 3, pp. 377–445, 1908.
- [80] T. Wriedt, “The Mie Theory: A review,” *The Mie Theory: Basics and Applications*. pp. 53–71, 2012, [Online].

Appendix

The reflection spectrum of the 9-layer film stack was measured after every deposition and etching. This measurement is to check every layer thickness of the fabricated 9-layer film stack by measuring the reflection spectrum. If there is a large error between the measured reflection spectrum and the spectrum obtained by simulation, it means that there is a layer thickness fluctuation happened during the deposition and etching process. The 9-layer film stack with reflectance error will be disposed. The 9-layer film stack without large reflectance error will be applied for the 18-layer interference filter fabrication.

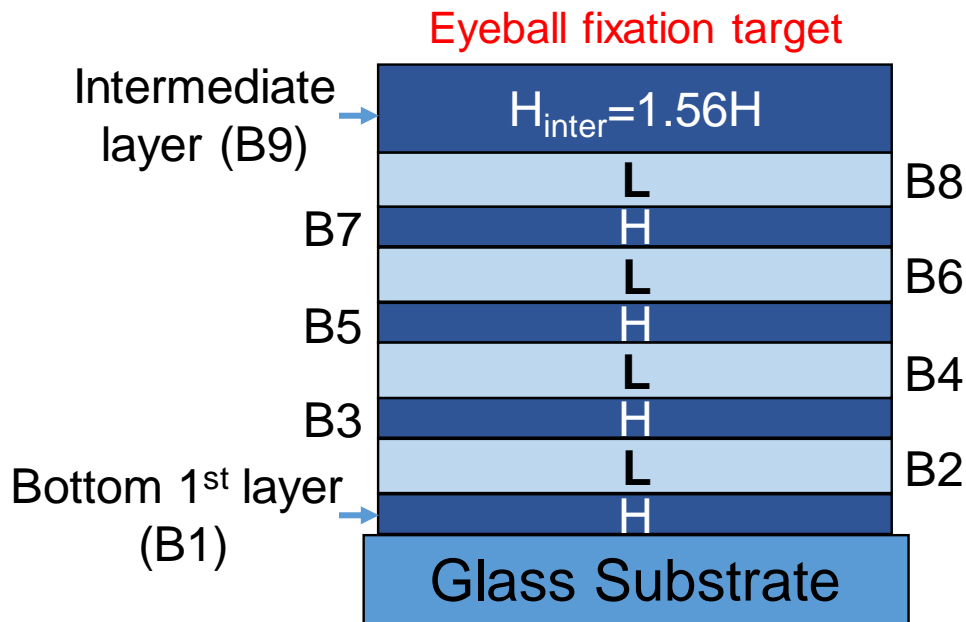


Figure 1 Schematic structure of the bottom 9-layer film stack of the multi-functional interference filter.

The first reflection measurement is after the deposition of the 9-layer film stack. Figure 1 shows the schematic structure of the deposited 9-layer film stack. Where H and L mean the thickness of high and low refractive index layer, respectively. From bottom to top, each layer is represented by B1 to B9 respectively. The photolithography progress and etching process are only performed on the intermediate layer (layer B9). Figure 2 shows the measured reflection spectrum of the bottom 9-layer film stack. In this figure, the measured reflection spectrum has

a high overlap degree with the theoretical one, which means every layer thickness in the 9-layer film stack is close to the thickness of each layer in the simulation. The measured reflection spectrum proves every layer thickness of the deposited 9-layer film stack is proper.

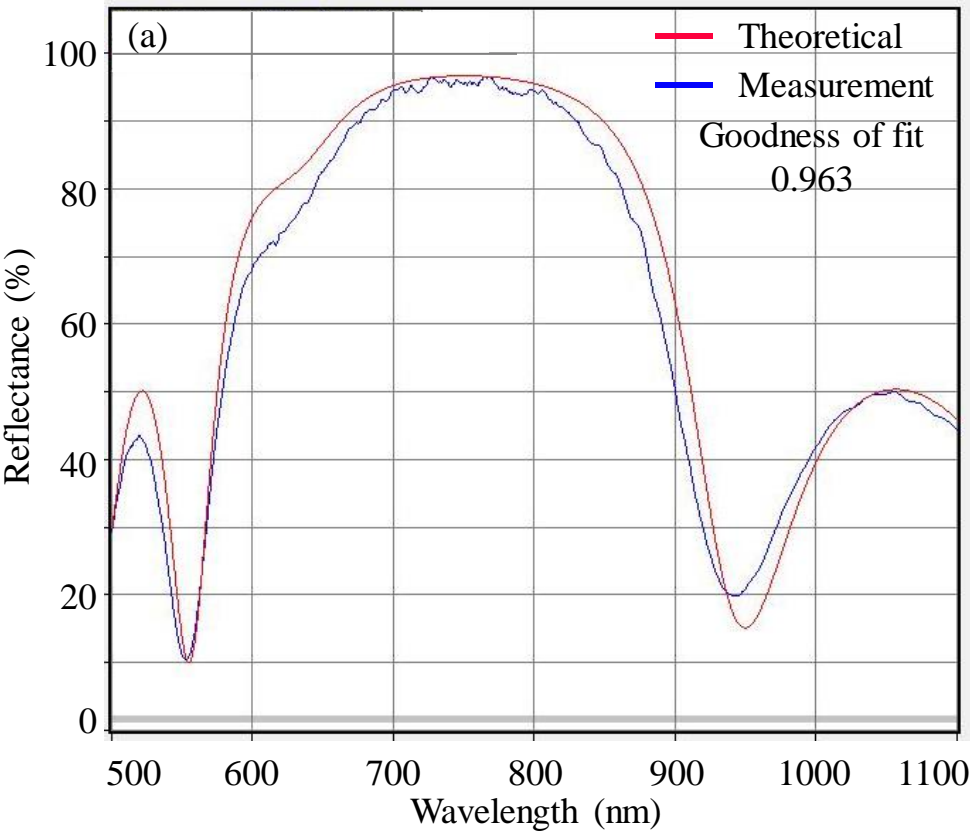


Figure 2 The comparison of the reflection spectrum between the theoretical and measurement of the deposited 9-layer film stack.

After the deposition, the 9-layer film stack was moved to the photolithography and etching process. Two rounds of the photolithography and the etching processes are needed to form the fundus illumination area and linear stripe pattern successively. After the first round, the fundus illumination area was formed. Figure 3 shows the schematic structure of the 9-layer film stack after the first photolithography process and etching process. The thickness of layer B9 was decreased to $0.64H$ to form the fundus illumination area. The measured reflection spectrum of the fundus illumination area in the 9-layer film stack is shown in Figure 4. In this figure, the measured reflection spectrum has high goodness of fit with the theoretical one, which means

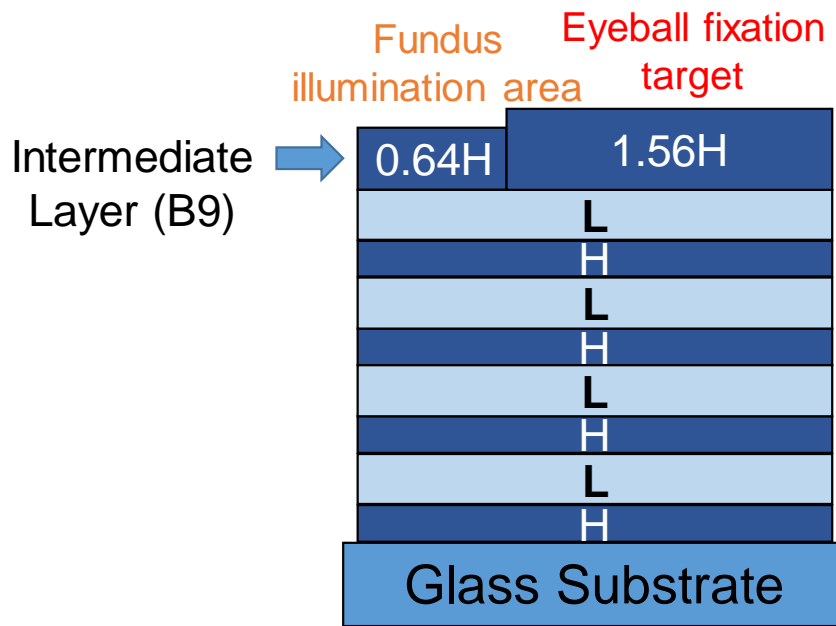


Figure 3 Schematic structure of the 9-layer film stack after the first round of photolithography and etching process.

the intermediate layer thickness of the fundus illumination area in the 9-layer film stack is close to the simulation results. The measured reflection spectrum proves the photolithography and etching process for the formation of the fundus illumination area is proper.

To form the linear stripe pattern in the 9-layer film stack, the second round of the photolithography and the etching processes is performed. Figure 5 shows the schematic structure of the 9-layer film stack after the second photolithography process and etching process. The thickness of layer B9 was decreased to $0.17H$ to form the linear stripe pattern. The measured reflection spectrum of the linear stripe pattern in the 9-layer film stack is shown in Figure 6. In this figure, the measured reflection spectrum has high goodness of fit with the theoretical one, which means the intermediate layer thickness of the linear stripe pattern in the 9-layer film stack is close to the simulation results. The measured reflection spectrum proves the photolithography and etching process for the formation of the linear stripe pattern is proper.

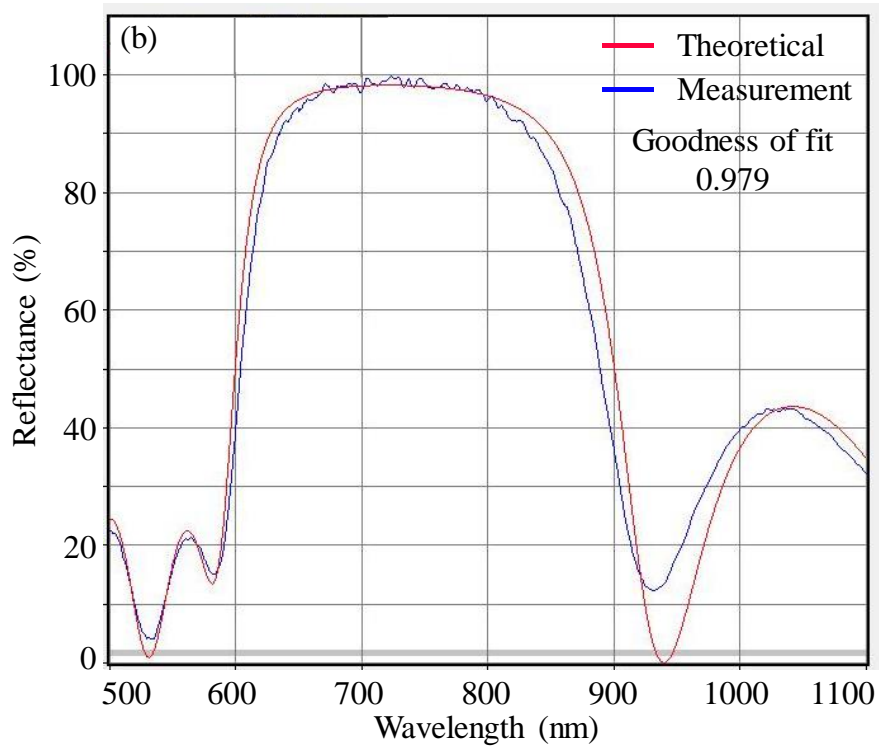


Figure 5 The comparison of the reflection spectrum between the theoretical and measurement of the fundus illumination area in the 9-layer film stack after.

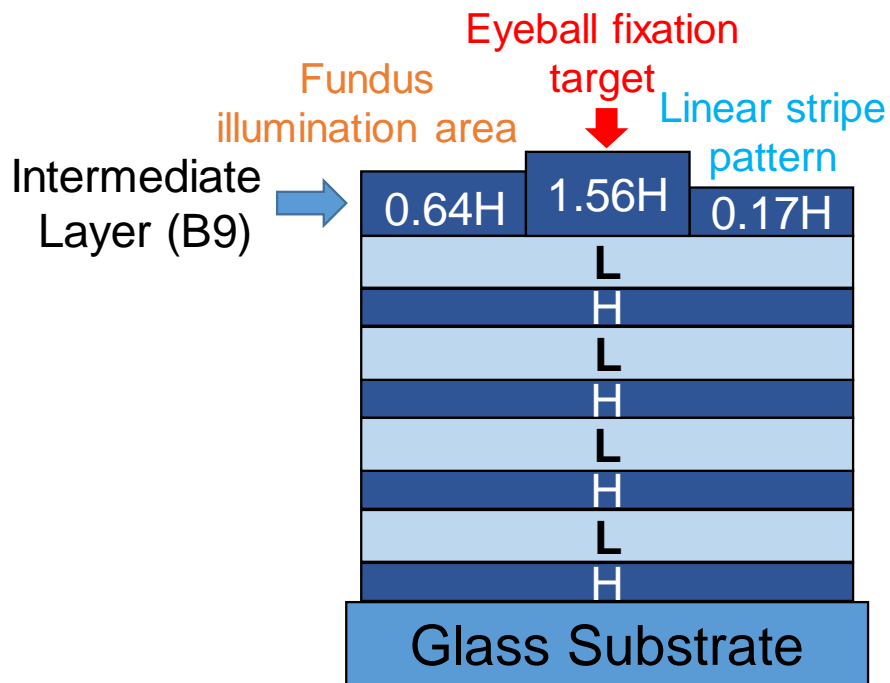


Figure 4 Schematic structure of the 9-layer film stack after the second round of photolithography and etching process.

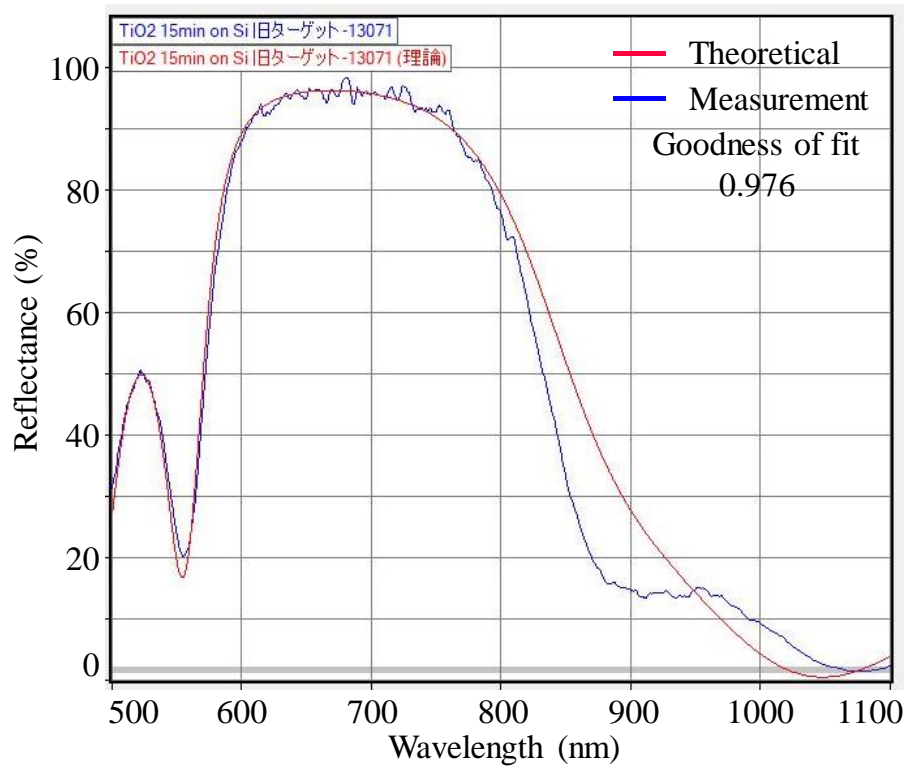


Figure 6 The comparison of the reflection spectrum between the theoretical and measurement of the linear stripe pattern in the 9-layer film stack after.

List of publications

● Journals

[1] **Ze Wang**, Masayuki Uemura, Hironari Takehara, Makito Haruta, Hiroyuki Tashiro, Kiyotaka Sasagawa, Jun Ohta, "Near-infrared fundus camera with a patterned interference filter for the retinal scattering detection" Japanese Journal of Applied Physics, vol.60, no.SB, pp.SBBL07, 2021.5.doi:10.35848/1347-4065/abea4c

[2] Honghao Tang, Hironari Takehara, **Ze Wang**, Noriaki Kishida, Makito Haruta, Hiroyuki Tashiro, Kiyotaka Sasagawa, and Jun Ohta, "Multi-channel bandpass filters for reconstructed high-resolution spectral imaging in near-infrared fundus camera," Sensor and Materials. [Accepted in Feb. 2022]

[3] Hironari Takehara, **Ze Wang**, Honghao Tang, Noriaki Kishida, Yusuke Horiki, Motoshi Sobue, Makito Haruta, Hiroyuki Tashiro, Kiyotaka Sasagawa, Jun Ohta, "Near-infrared colorized imaging technologies and their fundus camera applications," ITE Transactions on Media Technology and Applications. [Accepted in Feb. 2022]

● International conferences

[1] **Ze Wang**, Hironari Takehara, Honghao Tang, Noriaki Kishida, Makito Haruta, Hiroyuki Tashiro, Kiyotaka Sasagawa, Jun Ohta, "Design and fabrication of patterned interference filter in near-infrared fundus camera for retinal scattering detection" 43rd Annual International Conference of the IEEE Engineering in Medicine and Biology Society (EMBC), 2021.11.1.

[2] Honghao Tang, Hironari Takehara, **Ze Wang**, Noriaki Kishida, Makito Haruta, Hiroyuki Tashiro, Kiyotaka Sasagawa, Jun Ohta, "Optical design of multichannel bandpass filter for human eyefundus spectroscopy using selfie near-infrared fundus camera" 2021 International Conference on Solid State Devices and Materials (SSDM2021), 2021.9.8.

[3] **Ze Wang**, Masayuki Uemura, Hironari Takehara, Makito Haruta, Hiroyuku Tashiro, Kiyotaka Sasagawa, Jun Ohta, "Near-infrared fundus camera with patterned illumination mask for lipid concentration determination based on light scattering from retinal blood vessels" 2020 International Conference on Solid State Devices and Materials(SSDM2020), 2020.9.30.

[4] Hironari Takehara, Hirofumi Sumi, **Ze Wang**, Takahiro Kondo, Makito Haruta, Kiyotaka Sasagawa, Jun Ohta, "Multispectral Near-Infrared Imaging Technologies for Nonmydriatic Fundus Camera," Biomedical Circuits and Systems Conference 2019 (BioCAS2019), 2019.10.19. Nara Kasugano International Forum, Nara, Japan.

● Domestic conferences

[1] 岸田 憲明, 王 澤, 湯 鴻浩, 堀木 雄介, 竹原 浩成, 田代 洋行, 春田 牧人, 笹川 清隆, 太田 淳, "単板イメージセンサを用いた近赤外カラー眼底カメラにおける画像処理改善および視線固定法の検討" 映像情報メディア学会 2021年冬季大会, 2021.12.16.

[2] 竹原 浩成, 山根 宏大, 王 澤, 湯 鴻浩, 杉江 謙治, 岸田 憲明, 田代 洋行, 春田 牧人, 笹川 清隆, 國定 照房, 太田 淳, "超広角近赤外カラー化眼

底カメラの開発”, 第 82 回応用物理学会秋季学術講演会 , 2021.9.13.

[3] 岸田 憲明, 王 澤, 湯 鴻浩, 竹原 浩成, 角 博文, 春田 牧人, 田代 洋行, 笹川 清隆, 太田 淳, “近赤外カラー眼底カメラ用モザイク干渉フィルタ搭載イメージセンサの作製と評価”, 情報センシング研究会 (IST), 2021.6.30.

[4] 上村 将之, 王 澤, 竹原 浩成, 角 博文, 春田 牧人, 笹川 清隆, 太田 淳, “モザイク多層膜干渉フィルタ搭載イメージセンサによる近赤外カラー眼底撮像” 映像情報メディア学会 創立 70 周年記念大会, 2020.12.22.

[5] 上村 将之, 王 澤, 竹原 浩成, 角 博文, 田代 洋行, 春田 牧人, 笹川 清隆, 太田 淳, “近赤外カラー高速眼底カメラ向けイメージセンサへのモザイク多層膜干渉フィルタ搭載と評価” 情報センシング研究会 (IST) , 2020.7.1.

[6] 近藤孝彦, 王 澤, 竹原浩成, 角 博文, 笹川清隆, 春田牧人, 太田 淳, “近赤外カラー高速眼底撮像用オンチップファブリペロー干渉フィルタの作製と評価,” 映像情報メディア学会 冬季大会 2019, 2019.12.13. 電気通信大学.

[7] Wang Ze, Takahiro Kondo, Hironari Takehara, Kiyotaka Sasagawa, Makito Haruta, Jun Ohta, “The optimization of light path in advanced near-infrared color fundus camera,” 2019 年映像情報メディア学会年次大会, 2019.8.30. 東京工業大学 大岡山キャンパス.

[8] 近藤 孝彦, 王 澤, 竹原 浩成, 角 博文, 笹川 清隆, 春田 牧人, 太田 淳, “近赤外マルチスペクトル高速眼底カメラ用オンチップファブリペロー干渉フィルタの開発,” 2019 年映像情報メディア学会年次大会, 2019.8.28. 東京工業大学 大岡山キャンパス.